Politecnico di Torino

ScuDo
Scuola di Dottorato ~ Doctoral School
WHAT YOU ARE, TAKES YOU FAR

Doctoral Dissertation
Doctoral Program in Electrical, Electronics and Communications Engineering
(35th Cycle)

An Arduino-controlled bioreactor for stimulation and in situ pH monitoring of cell cultures with Organic Thin Film Transistors

By

Nicolò Cacocciola

Supervisor(s):
Candido Fabrizio Pirri
Matteo Cocuzza
Simone Luigi Marasso

Doctoral Examination Committee:
Prof. A.B. , Referee, University of….
Prof. C.D. , Referee, University of…
Prof. E.F. , Referee, University of….
Prof. G.H. , Referee, University of…
Prof. I.J. , Referee, University of….

Politecnico di Torino
2023

Declaration

I hereby declare that, the contents and organization of this dissertation constitute my own original work and does not compromise in any way the rights of third parties, including those relating to the security of personal data.

Nicolò Cacocciola

2023

* This dissertation is presented in partial fulfillment of the requirements for **Ph.D. degree** in the Graduate School of Politecnico di Torino (ScuDo).

Alla mia famiglia e ai miei amici più cari

Acknowledgment

First and foremost, I would like to acknowledge my supervisors, Prof. Candido Fabrizio Pirri and Prof. Matteo Cocuzza for introducing me in our research group, making possible this journey where I explored fields incredibly interesting and sometimes far from my scientific background. I would like to acknowledge Francesca Frascella and Simone Marasso for guiding me during my work and special thanks also goes to Giancarlo Canavese to giving me the right inputs and corrections during these years. I would also like to acknowledge Lucia Napione and Désirée Baruffaldi for the support they gave me for the biological part of this work. I would also acknowledge Valentina Monica and Luca Primo, with whom I explored the first conceptualization of my research work during the first year of this journey.

Very special thanks goes to Simona Villata, who supported my work and interacted with me during these years and to Pietro Zaccagnini and Davide Arcoraci who made possible the exploration of new pathways during this research work, giving me a huge help during the exploration of the biochemical part of my research. I must also mention Matteo Segantini, Matteo Parmeggiani and Alessio Verna, who taught me everything about the development of organic transistors, giving me continuous support.

Abstract

During the development process of cancer drugs, costly and time-consuming animal tests should be substituted with more effective experimental methods that go beyond traditional cell culture in multi-well plates. Over the past two decades, new research areas have emerged that are heading toward experimental models that reproduce the organ-specific microenvironment in order to maintain cell differentiation and tissue-specific function. Research and industry in the field of drug development and therapeutics is not sufficiently covered by flexible platforms suitable for the use with conventional cell culture methods, despite the presence of several complex systems attempting to mimic the conditions occurring inside human organs. Additionally, it is hard to employ in situ live traditional detection methods during cell growth, which are often used in biology laboratories, including the measurement of absorbance in multi-well plates and the monitoring of physical, chemical and biological factors during cell development, or accurate in vitro tracking of early/late apoptosis and necrosis of cells, as well as physical variables like pH and O_2 content, NO_x and glucose. Additionally, the acidity of the culture medium influences the cell metabolism, gene regulation and life cycle, making in situ pH monitoring an effective tool for the development of cell cultures. As a result of studies on pH monitoring in cell cultures, systems for real-time pH monitoring, including OECTs (organic electrochemical transistors) have been developed. They are a type of biosensors widely studied in recent years, offering advantages such as excellent sensitivity, exceptional stability, and low cost. In this work, a versatile and programmable multi-well plate culture system compatible with the growth of both normal and tumorous lung cells is proposed. By periodically

increasing the hydrostatic pressure inside the culture chamber, such system exposes cells to mechanical stimulation that mimics a normal breathing cycle. The controlled hydrostatic pressure increase inside the culture chamber, on the other hand, increases the partial pressure of gases in the culture chamber, particularly CO_2, which can result in the production of carbonic acid and a lowering of the pH of the culture medium once it has dissolved in the fluid used for cell growth. The development of pH-sensitive OECTs which are designed to operate directly inside the system to monitor pH variations within the culture medium during cell growth is proposed. The system discussed in this dissertation showed the feasibility of growing a cell culture inside it, and the stability of the pressure cycles set via software via a microcontroller unit. Moreover, no significant temperature perturbation induced by the pressure cycles have been observed within the system, since this parameter could influence cell development. An array of pH-sensitive OECTs have been developed, which turned out to be suitable for working inside cell culture media, opening the path for future cell culture in situ monitoring. Despite the pH sensitivity of such devices has been demonstrated, further investigation is needed to improve OECTs performance and to make them suitable not only to detect pH, but also to open the path to the detection of key biomarkers during cell growth. Further research work should be made in the future, to integrate the programmable cell culture platform with an array of OECT-based biosensors.

Contents

List of Figures

List of Tables

Chapter 1

From static to dynamic cell cultures

1.1 Introduction

One of the most discussed challenges in healthcare is the lack of models which recreates the preclinical conditions of the development of organs and tissues [1]. Animal cell lines and animal studies are widely employed for human drug development, inevitably leading to poor correlations between animal tests and the ones performed on humans, or also between in vitro and in vivo cell culture data. Drug companies often fail during the process of drug development, because correct prediction of human responses is not possible with these methods [2]. This can lead to high drug costs, less new products in the pipeline, chemical compounds characterized by a limited efficacy, and good products lost in failed implementation. A new method to study the physiology of organs and new drugs testing systems for the research field of personalized medicine is needed. It is well known that biochemical signals like the growing factors of cells, cytokines, and the role played by transcription factors possess a critical role in the mechanism of regulation of a wide variety of cellular activities, and also in maintaining the typical structure and function of cell tissues and organs. The biochemical signals are not the only players in this scenario, the biophysical signals play a very important role as well. There is increasing evidence that the biophysical signals, particularly the mechanical ones, play very important roles at various stages of the development of human tissues and organs, starting from the morphogenesis

mechanism occurring during the development to the maturation and maintenance of tissue and organ function throughout life. In order to understand the mechanism through which mechanical signals are related to cell and tissue development, a lot of effort have been made to develop different materials and devices with the function of deliver different typologies of mechanical stimuli to tissues growing inside them. In this chapter we discuss the current state of the art in this specific research field, focusing also on the design and development principles, highlighting the major challenges and prospects for the future.

1.2 Mechanotransduction

Mechanotransduction refers to the process by which the mechanical forces are directly converted into cellular signals that can trigger biochemical responses in cells. It is a fundamental process that is critical for many biological functions such as touch sensation, hearing, muscle contraction, and bone formation. The process of mechanotransduction begins with the detection of mechanical forces by specialized proteins called mechanoreceptors, which are located on the surface of cells. These mechanoreceptors can be activated by a wide variety of mechanical stimuli, such as hydrostatic compression, tension, or stretching. Once activated, the mechanoreceptors transmit signals to the interior of the cell through a complex network of signaling pathways, which ultimately lead to changes in gene expression, protein synthesis, and cellular behavior. For example, mechanical forces on bone cells can trigger the expression of genes that promote bone formation and remodeling, while mechanical forces on skin cells can trigger the release of neurotransmitters that generate touch sensation. Mechanotransduction is also important in the field of tissue engineering, where researchers aim to use mechanical cues to guide the development and behavior of cells in engineered tissues. By understanding the mechanisms of mechanotransduction, scientists can design materials and devices that mimic the mechanical properties of natural tissues and promote cell growth and function. Biochemical signals are a very important key factor in the regulation of cell activity, formation of tissues, and the function of organs during the development of human life. During the very early stages, a wide variety of biochemical signals regulates the embryonic development such as growing factors and cytokines, and also the transcription ones which regulates cell proliferation, cell migration and differentiation, and the formation of tissues [3]. Organs are subjected to a maturation process occurring after embryonic and fetal development, which usually last for the next twenty years. During this process, biochemical compounds such as hormones act as a

regulator of organs function, influencing a wide variety of mechanisms such as metabolism, reproduction and growth [4]. A lot of works has been inspired by the roles played by biochemical signals during these mechanisms, for example in the field of regenerative medicine, in order to better understand how the cell microenvironment controls its behavior, to achieve the regeneration of organs and tissues [5]. In addition to the cell microenvironment, some biophysical features such as mechanical forces to which cells/tissues are subjected, have also an important role in the regulation mechanism of cell behavior, including cell proliferation, cell differentiation and morphogenesis, and also the maintenance of tissue and organ function during the entire life of a living organism [6]. The interactions between cells and their surrounding microenvironment, has been shown to be directly dependent on factors influencing their development, such as the junction barrier between cells, the surrounding extracellular matrix (ECM), and the mechanical forces acting on cells and tissues during their normal development, making these features very important for tissue regeneration and also aging mechanism. [7]. A lot of development parameters are directly affected by the mechanical forces acting on tissues, such as cell growth, differentiation, and rearrangement of cells, the formation of macrostructures, and the morphogenesis of an embryonic cell [8]. A lot of studies performed in vitro highlighted the dependance of cell fate on mechanical stimulation directly acting on tissues, which as a result alter the cell shape [9]. A bright example of mechanical forces acting on tissues is given by the human musculoskeletal system, which is constantly subjected to mechanical stimuli during its entire life, which act on bone structure, muscles, and cartilages. For this reason, it is very important to consider such biophysical factors while performing studies on cell behavior and tissue development, and also to different typologies of stimuli not only strictly related to mechanical ones, such as electric, magnetic and acoustic stimuli, which have been shown to have an effect on cell development [10], [11]. Despite this, mechanical forces are the most studied among the various set of different biophysical stimuli, since mechanotransduction have been shown to be relevant during different life stages [12]. The mechanical stimulation of cells and tissues can be categorized in three main pathways:

- mechanical forces acting on the extracellular matrix surrounding the cells;
- mechanical forces belonging to the topography of extracellular matrix surface;
- mechanical forces applied directly to cells and tissues from an external source (Figure 1).

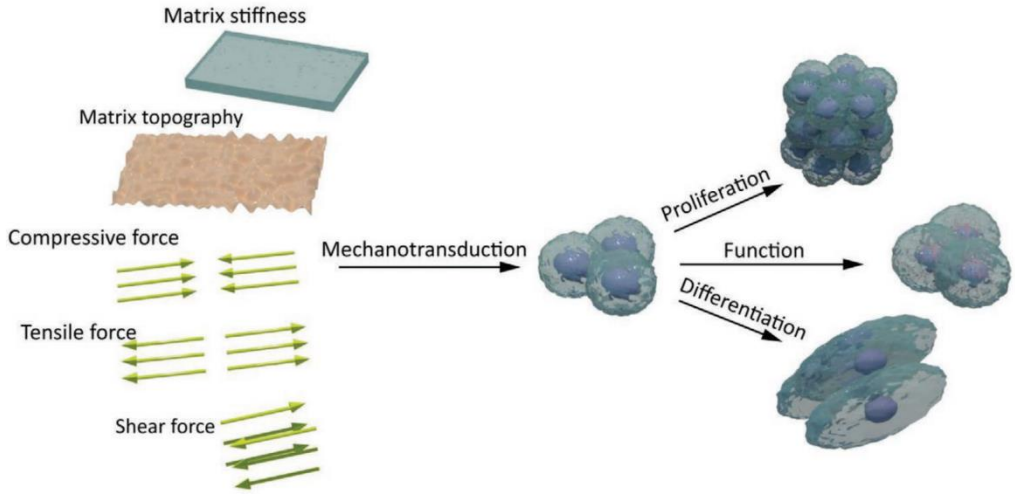

Figure 1 Representation of the effects of mechanical stimulations on cells. Reproduced with permission from John Wiley and Sons.

A lot of devices have been developed during the last two decades in order to assess the correlation between the presence of an external mechanical stimulus and the growth and development of cells and tissues. Such devices have been widely employed to study some of the key parameter just mentioned, such as the direct effect of mechanical stimulation on tissues topography [13], and also to study biophysical factors influencing organ regeneration and trying to analyze the mechanotransduction mechanisms influencing fetal cell development [14]–[16]. In this chapter, a summary on the insights into the choice of materials and devices developed to study the topics just mentioned is discussed, focusing on the different methodologies and effects on cells and tissues, providing the state of the art in the field of mechanotransduction and development of systems to stimulate living tissues, focusing on the basic design rules, existing challenges, and pathways for future development. Finally, a summary of the various possibilities in the mechanisms of transferring a mechanical stimulus to cells in the scenario of cell regeneration therapies for in vivo experiments is discussed. Cells and tissues can sense a mechanical stimulus coming from the surrounding environment both actively and passively through different mechanisms, starting from mechanically activated ion channels, receptor-ligand binding, and also considering the mechanism of coupling between the cell nucleus and its surface, as highlighted in Figure 2a [17].

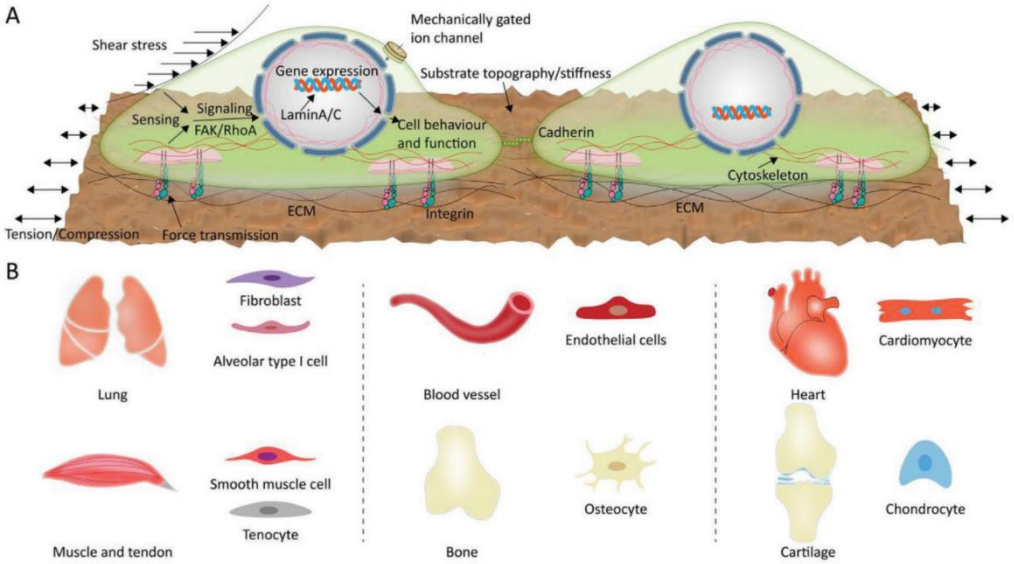

Figure 2 a) Schematization of the effects of mechanical loading on mammalian cells **b)** list of organs whose cells are mainly affected by mechanical stimuli. Reproduced with permission from John Wiley and Sons.

Considering active sensing, the mechanical properties of the extracellular matrix surrounding cells and tissues, and also factors such as topography and cell stiffness plays a key role. In passive sensing, the major players are the effects of external mechanical stimuli acting on cells, such as tension, shear stress, and hydrostatic pressure, which are mediated by neighboring cells and the surrounding environment such as matrix and cell culture medium. The mechanical stimulation of cells has been shown to act at an early stage on the activation of ion channels in the plasma membrane, which are directly controlled in a mechanical way, such as *TREK-TRAAK K2P* [18], *Piezo1* and *Piezo 2* [19], *TMEM63-OSCA* [20], and *TMC1* and *TMC2* [21]. Such ion channels are activated on a timescale of the order of microsecond, resulting in a very fast switching process which do not involve the presence of a second messenger, resulting in a change of the gate potential producing a very fast biochemical response [22]. Considering *Piezo1* and *2*, for example, it has been found that this ion channel plays a very important role during different biochemical processes, such as the formation of vascular tissues, pulmonary tissues and lung respiration, and mechanical transduction. Transmembrane receptors such as integrin, it is shown to behave as a transductor of mechanical signals coming from the surrounding environment of cells to structures of the cytoskeleton through the adhesion between cells and extracellular matrix, directly mediated by integrin [23]. After the formation of a focal complex during the cell development, the mechanical forces generated by the interaction

between actin and myosin are capable to activate different proteins such as vinculin, talin and paxillin, which leads to the subsequent activation of different signaling pathways such as *FAK-RhoA* and *RhoA-ROCK* [24]. These pathways have been shown to be capable to affect the mechanics of cell nucleus and also gene expression or actin polymerization and the contractility of actin and myosin, thus leading to a wide variety of mechanosensitive behaviors, such as proliferation, survival rate, stiffness, rearrangement, and differentiation [25]. The process of mechanical coupling occurring between the nucleus and cell surface through the action of mechanical forces on transmembrane proteins, is found to be capable to transmit mechanical forces along the entire tissue, thus avoiding the chemical signaling processes based on diffusion of chemical compounds, thus acting on the expression of genes [26]. Mechanotransduction plays important roles also on a wide variety of physiological and pathological processes involving a lot of human organs, such as respiratory system, cardiac system, and musculoskeletal system, physiological, and pathological processes in various tissues and organs, including lungs, blood vessels, heart, muscles, tendons, bones, and cartilage, as highlighted in Figure 2b [27], opening the path to further studies aiming to the regeneration and reparation of damaged living tissues, in the scenario of regenerative medicine.

1.3 Mechanical stimulation of cells

Tissues and organs of mammalians are mostly composed by different types of cells and extracellular matrices, possessing mechanical properties widely different. As an example, the Young modulus of such tissues can range from 100 Pa to 10 kPa. Considering osteoblasts, their Young modulus has been found to be in the range 3.5-4.2 kPa, [28], very similar to the one of fibroblasts, which has been found to be in the range 2-5 kPa [29]. Other tissues such as myoblasts and endothelial cells have been found to be characterized by Young moduli of around 11 kPa [30] and up to 3 kPa respectively [31]. A lot of variation on the overall mechanical properties of the various organs composed by the cells described above is thus expected, for example comparing soft tissues such as the ones composing heart, lungs and skin and hard tissues composing bones. As a result, the first tissues possess Young moduli with values ranging around 10 kPa, while musculoskeletal tissues tend to be extremely dense and packed compared to the first ones, with elastic moduli as high as tens of GPa.

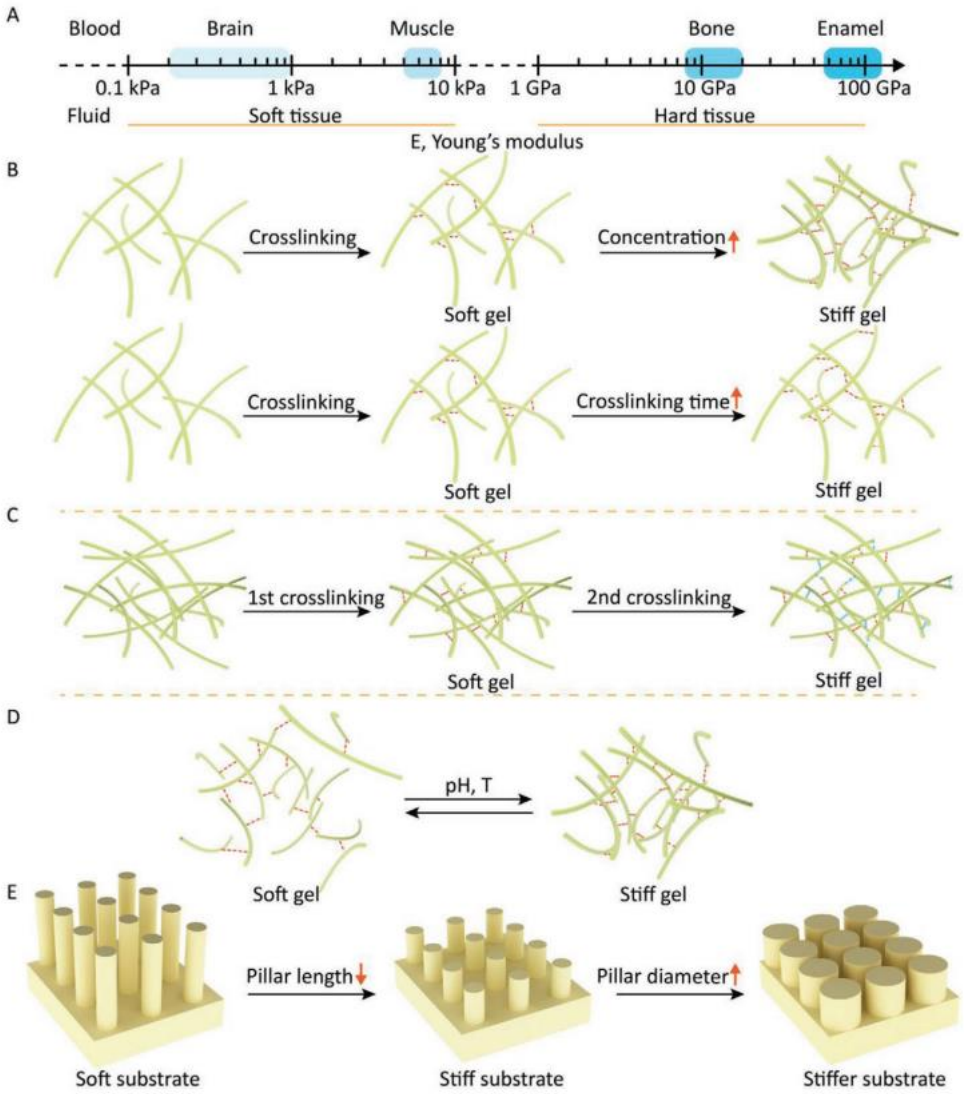

Figure 3 a) Elastic moduli of the principal types of tissues **b)-e)** principal mechanisms to modify the stiffness on gels and on pillar substrates**.** Reproduced with permission from John Wiley and Sons.

The composition and topology of the tissues described above thus affects directly the overall mechanical properties of such tissues. A lot of studies have been performed trying to investigate the role of the extracellular matrix stiffness and topology on the development of tissues and their mechanical properties. [32]. Such studies are mainly characterized by the employment of hydrogels to mimic the surrounding cell environment and study the effects of different structures by cross-linking such polymers following different topologies, in order to assess how different shapes are capable to influence cell behavior. Hydrogels are very convenient to perform studies of this kind, since their Young modulus is

selectable in the range between 10 and 100 MPa. Such materials can be made by different compounds, such as collagen, fibrin, hyaluronic acid, which are natural sources of gels, or from artificial polymeric compounds like gelatin methacryloyl (GelMA), polyethylene glycol (PEG) and poly(dimethylsiloxane) (PDMS) [30]. The mechanical properties of such materials can be easily controlled by acting on the concentration of their precursor compounds [33], [34], namely a low precursor concentration translates into a low stiffness and thus softer gels, while vice versa, a high precursor concentration translates into high stiffness and thus harder materials. Gel stiffness can also be modulated by acting on the exposure time to UV light, considering materials who are cross-linkable by light radiation, as highlighted in Figure 3b [35]. Another method to modulate the stiffness of such gels is the introduction of a second chemical crosslinker into the pre-crosslinked network, as shown in Figure 3c [36]. Finally, external physical and chemical stimuli such as pH and temperature have also been shown to be useful to modulate gel stiffness, as highlighted in the scheme of Figure 3d [37]. It is worth noting that, such methods are certainly very useful tools to modulate gel stiffness easily, but the drawback of such processes could be the structural changes produced by the employment of widely different crosslinkers concentration, which can result in structural changes in the final gel [38]. Gel stiffness can also be modulated mechanically, introducing external sources such as nanofibers and particles, resulting in a two-phase compound, and by creating anisotropic structures following freeze casting methodologies [39]–[41]. The drawback of the latter methods is the resulting change in gel nanostructure and chemical composition, thus making these methods not suitable for certain experiments. The introduction of such physical changes in gels could result in an effective modulation of their stiffness (and thus density), maintaining intact other properties. In Figure 3e is highlighted the modulation of such parameters in pillar-like structures by acting on the geometry of pillars. A lot of materials can be employed to build such structures, such as poly(dimethylsiloxane) (PDMS), metallic glasses and polyurethane acrylate (PUA) [42], [43]. Another aspect widely considered is viscoelasticity, which is found to be a parameter strongly influencing the mechanical properties of cell environment, thus translating in direct effects on cell development. Several material science approaches have been used to investigate the role of substrate relaxation on cell behavior. This includes the modulation of both polymer concentration and covalent crosslink density in hydrogels [44], the use of different quantities of covalent crosslinkers characterized by different affinities and lifetimes [45], the use of covalent versus physical crosslinking [46], and also acting on the molecular weight of the polymer and adding spacer

material [47]. Viscoelastic hydrogels developed by the methods discussed above differs from purely elastic materials and are more similar to physiological ECM, which are complex viscoelastic structures. Nevertheless, it is important to consider that changes in the chemical nature of the crosslinker (covalent or physical crosslinking) and the addition of spacer material can influence cell behavior that is independent of the resulting changes in the mechanical properties of the substrate. It has been shown that substrate stiffness can trigger a variety of cell responses, including spreading, attachment, migration, proliferation, osteogenic differentiation, adipogenic differentiation, chondrogenesis, neurogenic differentiation, myogenic differentiation, endothelial differentiation, and phenotype maintenance [34], [37], [48]–[51]. A lot of studies have been carried out employing focusing on the very first events occurring during cell development, such as proliferation, attachment and migration using simple 2D cell cultures. Recent studies are pushing research towards different more complex cell cultures such as the 3D organoids/spheroids and the formation of cultures in which the tissue structure is recreated, trying to simulate the in vivo conditions in the development of biomaterials for precision medicine.

1.4 Fabrication techniques

As was already noted, the content and structure of the extracellular matrix vary, which is why various tissues and organs have distinct mechanical characteristics. The collagen fibers that make up the extracellular matrix are randomly arranged in certain organs, like the lungs and liver, but they are aligned in other tissues like tendons, providing the latter tremendous tensile strength and good hardness. In Figure 4a is highlighted a scheme providing some basic information on the extracellular matrix structure. Collagen nanofibrils, which have a finely aligned pattern and are integrated with hydroxyapatite nanocrystals, compose the extracellular matrix of the bone's framework. Tissue from bones has outstanding mechanical qualities, including high tensile and compressive strength, as well as high stiffness and great toughness, due to its highly aligned, anisotropic, and dual structural arrangement [52]. The toughest tissue in the human body is enamel on the teeth structure. Due to its high mineral phase composition and distinctive design, enamel found in teeth possesses remarkable structural and mechanical qualities [53]. The living organisms can sense and react to a variety of topographic signals through mechanical transduction that may be identical to those of the extracellular matrix. The cells not only secrete a matrix with distinct topographical features, as described in the case of the ECM of the

muscleskeletar system. Subsequent intracellular signals that result in a wide range of cellular responses in terms of proliferation, attachment, migration and differentiation, are caused by the perception of topographic aspects of the extracellular environment by the surrounding cells [54]. In addition, the way that cells create and arrange their natural surrounding matrix can be significantly influenced by topographic features. For instance, it has been demonstrated that cells such as fibroblasts, tenocytes, osteoblasts and gut cells may create precisely aligned collagen fibers when exposed to substrates characterized by a nanopatterned topography [55]. Biomaterial development for regenerative medicine applications has made use of the capacity to control cell activity and their surrounding matrix structure using topographical stimulations. Various sophisticated manufacturing technologies and material synthesis techniques have been used to create a range of topographical designs up to this point, such as grooves, crests, grids, curved arrays, vertical arrangements, matched fibers, nanoscale textured surfaces, porous arrangements, filament arrangements, and wrinkles, as highlighted in Figure 4b [55]–[66]. Porous layers are another type of topographic feature [67] and emulating natural surface features like foliage, insect wings, and natural materials.

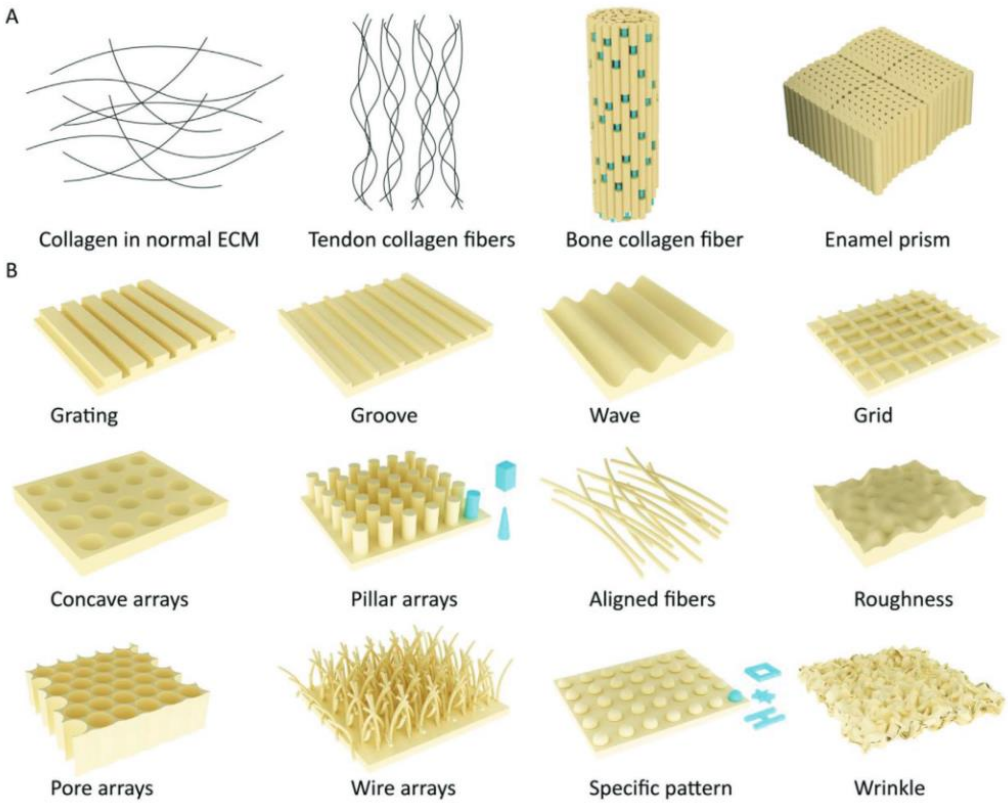

Figure 4 a) ECM structures exhibited by living tissues **b)** different types of geometries artificially fabricated to recreate the topography of living tissues. Reproduced with permission from John Wiley and Sons.

The application of modern fabrication and synthesis techniques is intrinsically related to the production of such a wide variety of topographic patterns. These methods are divided into several branches based on the production principle, including lithographic printing, pattern disposal, physical treatments, and chemical processes. Lithography is considered as top-down approach for creating micro and nanoscale surface patterns is lithography. There are several lithography methods, with photolithography being the most used. A predetermined geometric design is transferred using UV light during photolithography from a photomask to a photosensitive photoresist on a specific substrate. The exposed photoresist beneath the mask can be removed after exposure with a solvent, in order to display the patterned substrate. The resulting surface design is either etched into the substrate in subsequent processes or a coating of a new material is applied to it using a wide variety of procedures [68]. Chemical, deep reactive ion etching, and plasma etching are the most common etching techniques which can be used to fabricate micro and nano devices. Deposition methods include spin coating, electron beam deposition, electrodeposition and magnetron sputtering. By integrating the technology of photolithography with additional processes like hydrothermal treatment, soft lithography and hot embossing, the patterned geometry produced by photolithography may be further altered as well as transferred to other substrates [69]. Along with the mentioned techniques, other extensively used methods include electron beam lithography, X-ray lithography, colloidal lithography, and two-photon lithography [66], [70], [71]. Despite being very accurate and effective when producing topographic features, lithography-based methods are only effective in patterning two-dimensional surfaces on a restricted number of substrates. In order to transfer their patterns onto the required substrate materials, a variety of natural and artificial masters with precise topographic properties have been utilized as templates, including foliage, flower petals, organic structures, droplets of water and nylon fibers [72], [73]. Their predetermined characteristics however, make them more rigid than other systems, which is one drawback. Surface topographies have been developed through a variety of physical procedures, either top down or bottom up. While certain surface treatments, such as physical vapor deposition, deposit a thin film of material on the substrate, others, such as laser treatment, sanding and ion etching erode the surface of the substrate to form patterns. The majority of these procedures, including drilling, polishing, sanding, physical vapor deposition, and

electrospraying, are only compatible with few different topography patterns. However, it is possible that the underlying material would experience unfavorable phase shifts as a result of the high-energy beams used in laser ablation [74]. Even in highly aligned forms, electrospinning is a preferred bottom-up technique for creating fiber arrays [75]. A variety of topographic features can also be produced through chemical techniques such as anodization, which can create nanopore arrays, and also wet etching, which can produce surfaces with nanometric roughness. Other techniques such as chemical vapor deposition, can create vertical arrays and induce crystallization on the surface of the substrate, while electrochemical polymerization can create polymeric features with micrometric size [76]–[80]. Chemical modifications, which are not just applicable to two-dimensional surfaces, are promising to add topographic details to three-dimensional materials and hollow structures. Despite this, controlling topography at the required nanoscales is still difficult. Using the techniques described above, a variety of topographic features may be developed, allowing the investigation of interactions in the surrounding extracellular matrix. The regulation of stem cell differentiation and maintenance, as well as the modification of the matrix structure, are just a few biological applications where research in such areas has demonstrated considerable potential [81]. Despite the fact that many different kinds of topographic variables have been discovered and researched up to this point, basic concerns concerning the function of these distinct topographies remain unanswered. It is also vital to keep in mind that most existing approaches are restricted to two-dimensional surfaces and cannot be easily applied to three-dimensional porous or bulky scaffolds, which are crucial in the field of regenerative medicine. However, the degree of control of the spatial organization at the micro and nanoscale has limitations in these methods. Some manufacturing techniques, such as electrospinning, sintering, blending, etching, and chemical treatment, are relevant to three-dimensional materials. To better utilize patterning as a method of regulating how cells react to biomaterials and to create smart, tissue-inducing biomaterials, it will be crucial to understand the relationships between various topographical features and to develop and fabricate methods that allow spatially regulated patterning in 3D.

1.5 Typologies of mechanical stimuli

The heartbeat, breathing through the lungs, muscular contractions, and bone support are just a few examples of the many tissues and organs that operate to sustain life on a daily basis. As a result, numerous cells, including muscle,

tenocyte, epithelial, endothelial and chondrocyte cells, exist in a dynamic environment that is continually changing. Alveolar cells, cardiac muscle cells, tenocytes, and muscleskeletal cells frequently switch between relaxed and stressed states. While walking, leaping, and running compress chondrocytes in cartilage, blood flow continuously exposes vascular endothelial cells to shear stress. As a result, mechanical forces are believed to be significant throughout the life of an individual, from morphogenesis in the very first stages of cell growth to the development and maintenance of cells and organ functionality after birth. Evidence is that while muscular mass and size tend to decline when an human is restricted to resting for extended periods owing to sickness, appropriate physical exercise can enhance muscle cell proliferation, leading to larger and stronger muscles. Heterogeneous muscle fibers with different physiological and metabolic characteristics composes skeletal muscle. Due to their diversity, several muscle groups can offer a range of functional characteristics. Skeletal muscle adapts to its environment by reprogramming gene expression through the activation of signaling pathways, which maintains muscular function. Recent research has used a variety of stimulation techniques, including lifting weights, electric stimulation, microgravity, and sick circumstances, to demonstrate how the genetic structure of muscle fibers changes in accordance with functional demands. Skeletal muscle remodeling has been demonstrated to involve many transcription factors, gene activators, and repressors as well as calcium-dependent signaling pathway components. The development of novel therapeutics that focus on treating sick states will undoubtedly benefit from an understanding of the processes behind the modification of skeletal muscle characteristics [107]. Several research using external mechanical stimulation of cells and tissues have been carried out so far in order to explore how mechanical forces impact cell activity, tissue development, and regeneration. Tension forces, shear forces, and hydrostatic pressure are the four categories into which the diverse mechanical stimulation modalities are divided.

1.5.1 Tension forces

In order to apply mechanical deformation in cellular in vitro models, flexible membranes are typically used. These membranes can either be deformed through the application of fluid or gas force (either positive or negative) to a permeable flexible membrane from one end, as schematically shown in Figure 5, or they can be stretched in one direction by stretching a particular membrane region. In the 1990s, first-generation of cell stretching systems were created with the intention

of causing uniaxial stretch in bi-dimensional cell models of simpler cells, notably muscles.

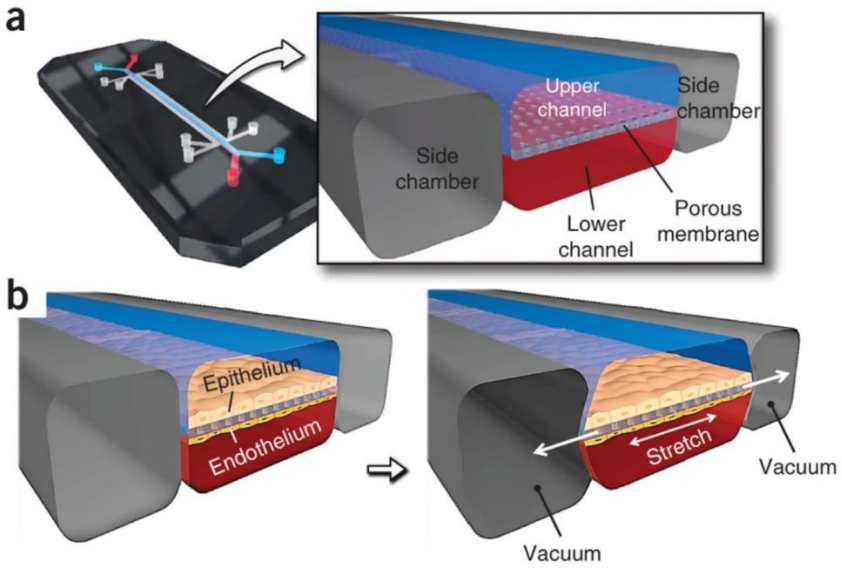

Figure 5 a) Structure of a lung on a chip in which the barrier between endothelium and epithelium is recreated **b)** mechanism to mimic the stretching forces on the tissues. Reproduced with permission of Springer Nature.

Cyclic stretch is necessary for muscle development because the mechanical transduction processes that underlie myogenesis are controlled by stretch-sensitive ion channels that, once triggered, alter calcium homeostasis, which controls the fate of cells (proliferation or differentiation) [82]. Other tissues may not be as dependent on this mechanical input, yet tensile stress can still have an impact on their physiological and pathophysiological condition. Stepper motors have also been used to stretch silicon chambers in some systems [83]. The diameters of the chambers have been decreased and merged into sealed chambers and channels to apply this concept to organ-on-a-chip devices, in which typically, membranes are put between neighboring channels or cultured areas usually made of PDMS. [84]. Such membranes can be punctured during construction to allow for efficient molecular exchange and cell-to-cell transmembrane communication. These organ-on-a-chip models mostly replicate the lung, but they also include other tissue models into similar chip systems for investigating different organs such the intestine [85]. Applied strain forces are reported as either linear, superficial, circumferential, or radial strain. Linear strain-the predominant variant-has been reported to induce up to 50%, while most devices induce around 10% [86]. The resulting surface strains are usually somewhat higher - up to 60% - and the

circumferential and radial stresses are usually less than 20% [87]. Despite these variations in tension forces, strain frequencies for all organ models average about 0.2 Hz and rarely exceed 1 Hz. However, current research fusing PDMS-made membranes together with microelmechanical platforms has paved the way for extremely miniature membranes that allow the generation of strain frequencies as high as 870 Hz, allowing even the most extreme physiological conditions, like blunt force trauma, to be studied [88]. A lot of measures must be taken to prevent the change in the amounts of given pharmaceuticals and stimulants since silicone-based membranes can absorb hydrophobic compounds not only via surface contacts but also by diffusion of molecules through the pores of the polymer. Alternative materials are, however, infrequently employed as stretchable membranes. Reliable bonding for PDMS devices is achieved by low-pressure plasma ignition and following assembling of the membrane to the neighboring layers [89]. In other processes, the membranes are fixed between the surrounding layers, often as the prepolymer is curing. To achieve full depletion of chemical precursors which are extremely hazardous to cells, such curing operations should be carried on beyond the period indicated in normal procedures, which turns out to be at least 36 hours [90]. Biocompatibility of adhesive compounds must be extensively verified. Membrane clipping is an alternative, however it frequently results in fluid loss or the development of air bubbles. Cell cultures are cultivated on flexible surfaces including rubber made from silicone, polyurethane, and PDMS structures coated with fibronectin, in order to emphasize the impact of tensile stress on cell activity in two-dimensions [91]–[93]. The cells cultured directly over the substrate were exposed to cyclic strain by pressing a penetrator on the substrate, as shown in Figure 6a. As illustrated in Figure 6b, another method for generating cyclic stress in cells involves applying programmed negative or positive pressure to an elastic substrate. Since polymer tubing enables the delivery of air/fluid pressure from the pumps towards the target device, a large portion of the pump system may be installed outside of the incubator, which makes it more practical to employ. Instead of using cells planted on an artificial substrate in a three-dimensional substrate, cell-loaded polymers, decellularized tissues and cell sheets have been also applied. The three-dimensional substrates were either planted directly using two straining clamps or set on additional flexible substrate supported again by straining clamps to study the impact of cyclical stress stimuli on the cells, as illustrated in Figure 6c. In certain instances, the test specimens were subjected to cyclic bending which was powered by mechanical forces or pressure, as illustrated in Figure 6d [94]. The tensile force produced by bending was often less uniform compared to the force

produced by extending the clamps. A few in vivo investigations have been carried out where mechanical force was directly delivered to in vivo organisms in addition to the aforementioned in vitro research. It's noteworthy that some studies demonstrated exceptional hair regrowth in mice when the right tensile force was given for the right amount of time [95].

1.5.2 Shear forces

Applying shear forces, which are induced by fluid flow and can, for instance, represent blood flow throughout capillaries or interstitial circulation through bone matrix, is the simplest approach to impart mechanical stresses to cells. The physical phenomenon starts off easily with a laminar flow occurring inside a straight fluidics in which cells are directly grown and attached to the inner surface, but it may become quite complex when for example, blood cells are introduced to the fluid. The above problems directly affect experimental setups should be taken into account during the development of such systems. [96]. Moreover, since continuous food delivery and waste disposal in cell culture models often are affected by medium perfusion, flow-induced shear forces are frequently challenging to minimize. Shear forces are usually expressed in dynes per square centimeter, namely

$$1\ dyn \cdot cm^{-2} = 10^{-5}N = 10^{-1}Pa \tag{1}$$

Considering endothelial cell cultures, physiologically relevant shear stresses forces vary from about 10 to more than 50 dyn/cm^2 while for bone osteoblasts, forces between 8 and 30 dyn/cm^2 have been reported in a very simplified cell model [97]. In order to prevent consequences that differ from in vivo conditions, other tissues might require to be shielded from shear stresses. Highly mechanosensitive cells are susceptible to shear stresses at considerably lower levels, hence fluid flow conditions and the layout of chips must be carefully taken into account. As an example, muscle cells have been shown to respond to forces of less than 0.1 dyn/cm^2 [98]. The shear forces induced by fluid flow can be approximated using the wall-shear rate model [99]:

$$\tau = 6 \cdot \frac{Q \cdot \mu}{w \cdot h^2} \tag{2}$$

$$\tau = 6 \cdot \frac{Q \cdot \mu}{\pi \cdot R^3} \quad (3)$$

in the case of a rectangular channel (2) and of a circular tube (3). In the equations, Q represents the volumetric fluid flow rate, μ is the dynamic viscosity of the fluid, h and w are the height and width, respectively, while R is the inner radius of the pipe. The fluid mechanics are most influenced by the inner radius or channel height characteristics, which also affect whether or not the device tends to produce large or small shear forces. They are thus the most crucial geometrical limitations for device design. Application of pulsing shear forces vs steady shear forces, in instance, can have distinct outcomes [100], which take place, for instance, in medium perfusion driven by peristaltic pumps. To increase their medicinal value, such patient-derived data may be converted to in vivo imitating on-chip models. Directly printing cells on a gel matrix is a new method for creating three-dimensional cell models. However, these printing techniques include large shear stimuli that may cause necrosis or cell damage [101]. Research on the long-term consequences of these shear stresses can help to enhance this adaptable technology by giving useful information. It is possible that other factors can affect experimental results, as an example, it is suggested that models used to test medications are capable to modify shear stimuli since mechanobiological factors have been demonstrated to alter drug delivery outcomes [102]. The many ways through which shear stresses induced by the flow affected the cell models under investigation, show how complexly biological systems interact with artificial environment, emphasizing the importance of design and evaluation. Here three key examples of how to provide shear stress to cells in two-dimensional cultures are discussed, which are often caused by fluid movement as is indicated in Figure 6e.

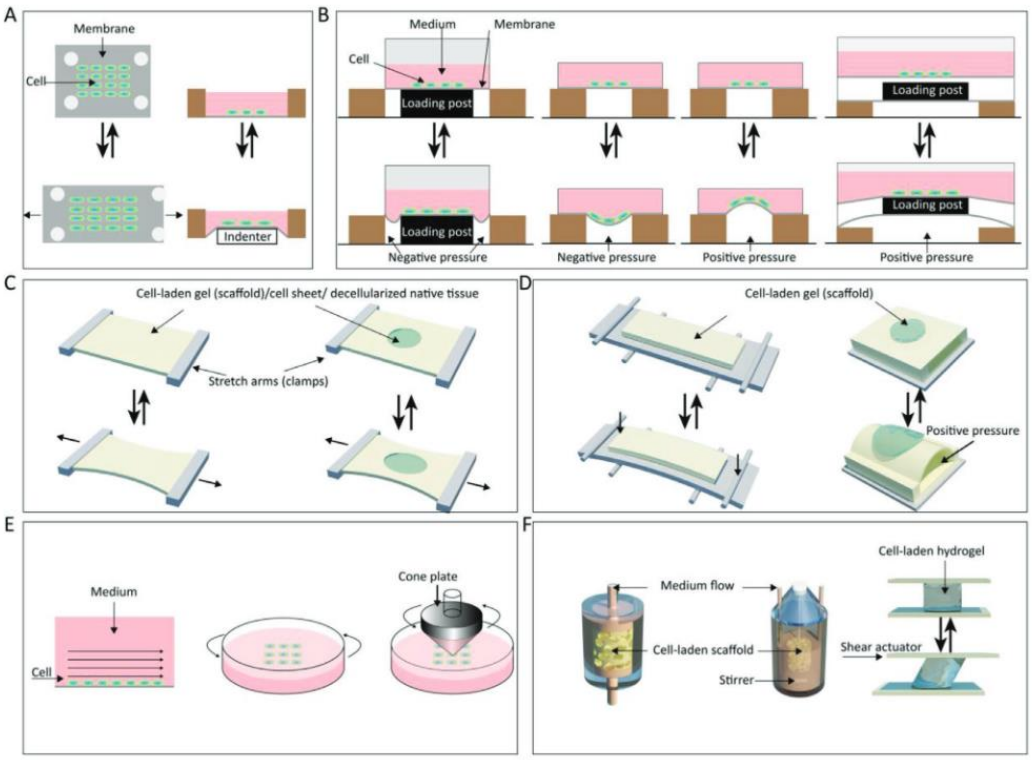

Figure 6 Artificial methods employed to simulate shear and tensile forces on living tissues. Reproduced with permission from John Wiley and Sons.

In the first instance, cell culture media was pushed through a static cultured chamber in which cells were grown, providing a constant flow that provided a shear stress to the cells [103]. In the second instance, the cells were planted in a surface following an orbital rotation. Once the culture plate vibrated, the culture medium became turbulent, applying shear stresses to the cells [104]. In the latter example, dynamic flow has been generated in the medium used to grow cells by spinning a cone instead of pumping or vibrating the media throughout the chamber [105]. Comparatively, the first technique produced the most consistent shear stress, whereas the second technique had the simplest setup. As indicated in Figure 6f, permeable scaffolds and gels were utilized to hold the appropriate cells while we investigated the consequences of shear stress in three-dimensional systems. These scaffolds have occasionally been loaded using a shear motor and put in stirred tanks or incorporated into perfusion systems.

1.5.3 Hydrostatic Pressure

Despite the fact all the cells composing the human organism are frequently compressed by gravity and body motion, only a small number of tissues require continuous dynamic and cyclical mechanical strain for growth and maintenance. The main stimulus for bone remodeling processes is this force framework [106], [107]. Some devices can simulate this early stage of cartilage formation, however many of them do not include this mechanical stress as an input. Nevertheless, models have been presented that incorporate mechanical input for chondrocytes and bone cells in artificial scaffolds, but compared to bones, these models are not sufficient to accurately capturing the cellular diversity and, consequently, the complex functions of the interactions occurring within in vivo bone tissue [108], [109]. The models that most nearly mimic in vivo environments currently utilize bone cells formed in in vivo conditions and subsequently implanted in chip systems where they can be successfully analyzed, since building such a complex tissue still requires technological advancements in integrated scaffold creation [110]. Current microvascular in vitro chip systems, however, do not take into account the intricate structure of the calcified skeletal matrix and instead concentrate on simpler bone models, such as those involving differentiation of skeletal stem cells or osteocyte integration. The models are comparable to chip devices designed to create mechanical loading because they employ multilayer soft polymeric devices with integrated flexible membranes that may be pushed into the cells. The models also feature dynamic mechanical loading. The applied mechanical load is specified either in terms of pressure, or in the description of the experimental setup utilized, involving parameters such as the compression distance or the loading force. The simplest approach reported in the literature for applying stress to cell layers cultivated in two-dimension was to apply a constant weight to the cells, as illustrated in Figure 7a, or to raise the hydrostatic pressure on the air around the cell culture by using a piston. These techniques allow for continuous, static, or cyclic compression stimulation. By incorporating the cells onto microfabricated devices and placing them beneath a deformable membrane, dynamic compression was made possible. The elastic membrane can be deformed under positive pressure, compressing the cells as a consequence. The membrane restores its natural form once the pressure was released, and the cells compressive force is thus decreased [111]. As shown in Figure 7a, the device can be constructed in such a way that it is possible to apply several pressure stresses to the cells of interest at once. The test environment may be converted from two-dimensional to three-dimensional by simply adding cell-loaded gels in

place of the original microfabricated devices' cells. As indicated in the scheme of Figure 7b, it is possible to stimulating various cell culture structures in a system at once with various pressure levels. The majority of these research applied cyclic stress stimuli to cell-loaded three-dimensional scaffolds both in a longitudinal or transverse way, using a mechanically powered constant/alternating load, as illustrated in Figure 7c. This technique can compress the material uniformly, but since the entire equipment is often somewhat big, it cannot be used for tissue culture. In vivo studies involving animals such as mice and rabbits have all been used [112], [113], demonstrating how compressive stress affects the formation intramembranous bone connectors as well as bone growth. It is quite simple to apply hydrostatic pressure to the appropriate cells and tissues as compared to both tension and shear stresses. The target cells are frequently positioned in a sealed space in with the hydrostatic pressure is increased in a controlled manner. The hydrostatic force is applied to the surrounding surface, and subsequently also on the samples, by supplying a constant or cyclical hydrostatic pressure to the liquid in the chamber. Diverse cell activities, such as differentiation, migration, apoptosis, and proliferation, can be controlled by hydrostatic pressure. Pathologies include glaucoma and reshaping in hypertensive diseases are linked to abnormal hydrostatic pressure values. Cartilage and bone formation have been found to be stimulated by hydrostatic tension [114], and has an immediate impact on lung tissue. The behavior of cells in the tissues of the brain, eye, blood vessels, and cartilage is controlled by hydrostatic pressure, and recent, major in vitro experimental work has demonstrated how the responses of cells in various tissues to this stimulation can vary dramatically. Elevated hydrostatic pressure has been shown to causes cell elongation in endothelial cells without cell realignment or cytoskeletal change [115]. By upregulating micro-ribonucleic acid (Mi-RNA), an increase in hydrostatic pressure encourages the proliferation of muscular cells in humans [116], [117]. High hydrostatic pressure causes the potential of the receptor vanilloid 1 of the retinal ganglion cells to be upregulated and raises intracellular Ca2+, which causes cell death [118]. Hydrostatic pressure causes ATDC5 cells to differentiate into chondrocytes over time [119]. Additionally, it has been demonstrated that increased hydrostatic pressure causes leukemia cells K562 and HL60 to shrink, while lung cancer cells A549 and CL1-5 increases their volume [120]. There is an urgent need to understand what drives these different hydrostatic pressure-regulated cell behaviors. The understanding of how biological reactions to mechanical stimulation are triggered has greatly benefited from the design and development of the broad spectrum of devices that are capable of applying mechanical stresses to cells and tissues that have been

documented so far. However, several of the above-mentioned devices are highly sophisticated, making them unavailable as common laboratory techniques. Furthermore, due to their complexity, it is challenging to extend their in vitro application to in vivo experiments. Even if some studies have been conducted using animal experiments, it appears improbable that identical procedures can be implemented to humans in the near future. However, the noninvasive use of mechanical stresses is a potential way to get beyond this problem.

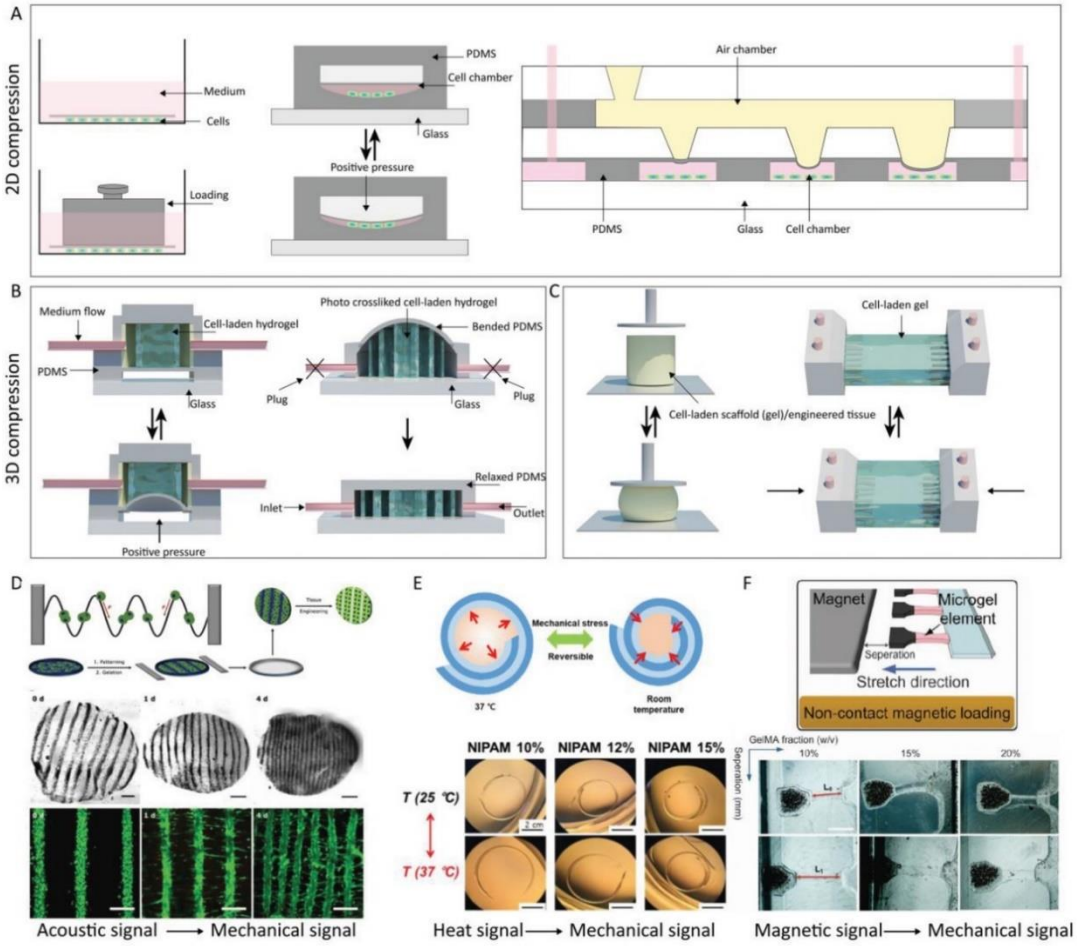

Figure 7 Scheme of different techniques used to apply compression forces on living tissues. Reproduced with permission from **[121]–[123].**

As an example, acoustic force stimuli have been successfully applied to cells using sound waves to induce cell patterning, as highlighted in Figure 7d. Figure 7e illustrates the application of a tensile stress to cells by controlling their temperature using a gel matrix sensitive to heat. Similarly, a magnetic field has been employed to deform magnetic scaffolds loaded with cells, thus applying

a mechanical force directly to the cells, as shown in Figure 7f [121]–[123]. Researchers may utilize all of these techniques as inspiration to create cutting-edge materials and tools for the mechanical stimulation of in vitro biological experiments.

Chapter 2

Organic Electrochemical Transistors

2.1 Introduction

Organic Field-Effect Transistors (OFETs) and Organic Electrochemical Transistors (OECTs) represent two classes of Organic Thin-Film Transistors (OTFTs), respectively. The difference is that OECTs employ an electrolyte instead of a traditional dielectric with dipoles between the channel and gate. OECTs can be identified by this distinction, which also gives rise to their unique electrical properties. OECTs gate-channel capacitances can reach tens of mF cm^{-2}, which is three orders of magnitude more than current high-k dielectrics. This is mostly due to the huge capacitance of electrolytic dual layers and the capability of ions to permeate organic semiconductors [124]. OECTs have outstanding signal amplification qualities and are able to work at very low voltages (below 1 V) thanks to their huge gate-channel capacitances. For example, the transconductance of OECTs can be greater than 500–800 Sm^{-1}, above the usual capacitance of most OTFTs, which is greater than conventional thin-film transistor technologies [125]. OECTs are particularly intriguing for applications in the area of wearable devices and biosensors since they also utilize materials that display mechanical flexibility (with a modulus of elasticity of several hundreds of MPa) and can be biofunctionalized [126], [127]. OECTs have been used by researchers for many different kinds of applications, including digital logic and neuromorphic engineering in addition to those that are explicitly connected to biological

sensing, as a result of these characteristics [128]–[131]. Several studies describing the operation of OECTs have been published as a result of the potential efficiency of such devices in various fields, which has stimulated study into the physics of OECTs. In this chapter, we go over current frameworks for various sides of OECT performance and demonstrate how the knowledge gained from them may be used to optimize and characterize OECTs. We also point out areas of study that need to be analyzed more deeply in order to comprehend the physics of such devices. First, section 2.1 provides a foundation on the OECT's guiding principles. The effects of device geometry on OECT behavior are then discussed in Section 2.2, along with how channel size might be selected to get the best performance. We cover several transient response models for OECTs in Section 2.3 and illustrate how an appropriate transient model results in a more precise interpretation of OECT observations. We discuss the consequences of parasitic resistance in series to the polymeric channel in Section 2.4 and offer several solutions for mitigating these effects. Finally, we discuss how the energy and structural disorder of polymeric semiconductors influences the behavior of OECT in Section 2.5.

2.1 Device physics of OECTs

Source, drain, and gate are the three metallic electrodes which make the conventional configuration of an OECT, as can be observed in Figure 8. A polymeric semiconductor channel built right between the source and drain electrodes serves as the active channel. The modification of the channel current operating on the gate potential is made possible by a liquid medium connecting the channel with the gate, as shown in Figure 8a. The semiconductor can be either a p-type material, which conducts holes, or an n-type one, which conducts electrons. For the sake of simplicity, we exclusively examine p-type devices in this chapter; nevertheless, the topic is also applicable to n-type semiconductor-based OECTs. The usual potentials and currents within an OECT are denoted in Figure 8b. In typical circumstances, the source electrode is grounded, and an electronic current, I_D, is driven across the channel between the source and drain electrodes by a steady bias voltage on the drain electrode, V_D. The device's output current, i.e., the drain current, may be modulated by changing the gate voltage V_G, as was already indicated. This modulation results from the ionic charge carriers forced diffusion into the active channel through the electrolytic solution due to the gate voltage. In this case, the ionic charge carriers provide charge balance to the holes, modulating their concentration and, in turn, the electrical

conductivity of the active channel. In an OECT device, the electrons (or holes) transport the channel current. The gate current, or I_G, which is transported by the ions in the electrolytic solution and supplies the ions neutralizing the electronic charge in the channel, is the ionic current that is generated by the electrolyte solution and directed towards the channel, as noted in Figure 8b. The gate current is solely capacitive and goes away in steady state because the source/drain electrodes prevent ions from moving and do not permit direct transfer of charges in a faraidic manner. The comparison between these two devices offers more information on how OECTs operate even if their behavior, as mentioned above, varies greatly from that of typical metal-oxide-semiconductor field-effect transistors (MOSFETs). The insulating material placed among the gate and the channel is the key distinction between these transistors. In contrast to OECTs, which have an electrolyte solution with mobile ions, MOSFETs have an oxide dielectric with nearly immobile dipoles that are strongly bound to their place by the SiO_2 lattice. As seen in Figure 9a, the gate voltage of a MOSFET polarizes the electrical dipoles of the oxide and produces a potential field that leads to the accumulation of holes within the channel along the interface between semiconductor and dielectric. In an OECT, as shown in Figure 9b, the gate-induced electric field forces ions into the device channel, causing holes to accumulate over the whole volume of the semiconductor film rather than at the interface between semiconductor and electrolytic solution. The high capacitance connected across the interface between gate electrode and polymeric semiconductor in these transistors is caused by this charge accumulation, which distinguishes an OECT from other electronic components. Although there are many differences between an OECT and a MOSFET, the physics of MOSFETs may still be used as long as the bulk capacitance of OECTs can be substituted with the capacitance associated with the MOSFET's interface [33]. For instance, D. Bernards and G. Malliaras' early model of OECT behavior (referred to as the "Bernards model") mainly depends on the comparison to MOSFET behavior [38]. The same collection of variables that explain the drain current in long-channel MOSFETs are employed in this model to describe the characteristics of electronic transport of charges in an OECT [46,47]. One has

$$I_D = \mu C \cdot \frac{W \cdot d}{L}\left[1 - \frac{V_G - \frac{1}{2}V_D}{V_T}\right] \cdot V_D \ \ when\, V_D > V_G - V_T \tag{4}$$

$$I_D = -\mu C \cdot \frac{W \cdot d}{L} \frac{[V_G - V_T]^2}{2V_T} \quad when\, V_D < V_G - V_T \tag{5}$$

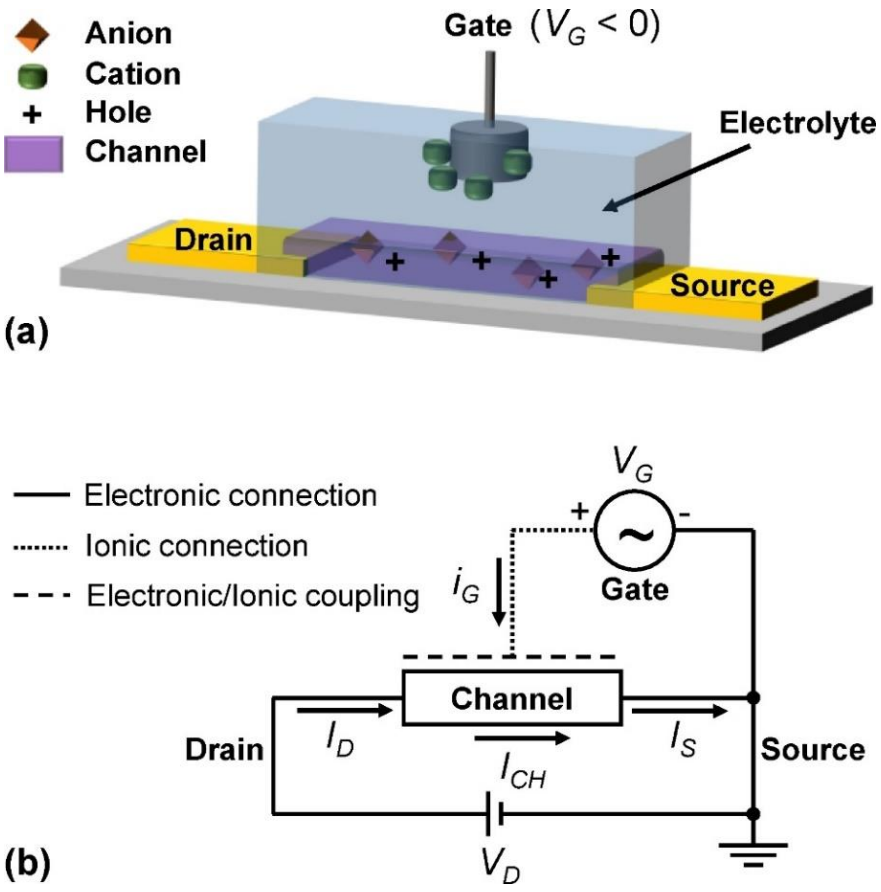

Figure 8 a) Scheme of an OECT with the gate electrode surrounded by an electrolyte medium, when a negative voltage is applied to the gate electrode. **b)** electronic diagram highlighting the various contributions to the channel current. Reproduced with permission from Elsevier.

Where I_D is the current of the channel, W, d and L are the geometric features of the channel i.e. width, thickness and length, mu the mobility of the charge carriers inside the channel, C the capacitance per unit volume. In the equations are also highlighted the electric parameters of the OECT in the same manner of a

MOSFET device, i.e. the voltage applied to the gate and drain electrodes (V_G and V_D respectively) and the threshold voltage V_T. From equation (4), one can calculate the transconductance gm of an OECT, defined as

$$gm = \frac{\partial I_D}{\partial V_G} \tag{6}$$

For applications like biological sensing, digital electronics, and brain-like devices which employ OECTs designed as signal amplifiers, this the quantity establishes the rate at which an OECT amplifies a signal at the gate electrode. In these situations, the impact of the gate voltage on the drain current that flows via the OECT channel is measured. This implies, for instance, that the transconductance is inversely correlated with the magnitude of the signal measured on an OECT-based biological sensor. The Bernards Model also covers the transient behavior of such devices, despite the fact that equations (4) and (5) are excellent mathematical representations for the steady-state explanation of an OECT. This may be accomplished by describing the flow of ions occurring between the gate electrode and the channel itself as an equivalent circuit constructed by a resistor in series with a capacitor and using a quasi-static estimation of the distribution of charges inside the OECT channel, as illustrated in Figure 8.

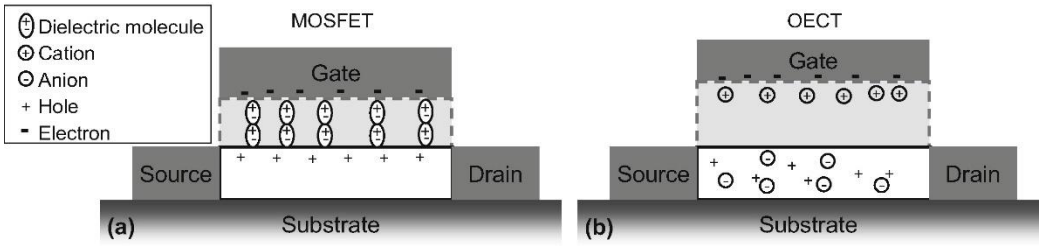

Figure 9 Comparison between a MOSFET **(a)** and an OECT **(b).** In a MOSFET the charge carriers in the insulators are locked on their position, while in an OECT they can move through the electrolyte solution and penetrate the channel. Reproduced with permission from Elsevier.

This model suggests that the equivalent ionic circuit modelled between the gate electrode and the semiconducting polymer defines an RC time constant that describes the reaction period of the drain current whenever the gate voltage changes. The Bernards Model is frequently used to define OECTs in a variety of applications due to its simplicity. In addition, we will make frequent references to

this model throughout this chapter since it provides the foundation for many more in-depth explanations of OECT device physics.

2.2 Tuning OECT performance

The most popular techniques for fine-tuning device shape to improve OECT performance are covered in this section. We will define scalability rules for OECT transconductance gm and topology in particular and explain how these factors impact the functionality of OECT-based sensors. As stated in the preceding section, equations (4) and (5) may be used to derive the transconductance, which can be defined as the derivative of I_D with respect to I_G. One has

$$g_m = \mu C \cdot \frac{W \cdot d}{L} \cdot V_D \ \ when\, V_D > V_G - V_T \tag{7}$$

$$g_m = -\mu C \cdot \frac{W \cdot d}{L} \cdot [V_G - V_T] \ \ when\, V_D < V_G - V_T \tag{8}$$

OECTs and MOSFETs vary significantly in that the first is characterized by a transconductance which scales also with thickness rather than only with their width, whilst the latter have a transconductance only related to the ratio *W/L*. This crucial distinction results from the fact that only the charge carriers concentration at the semiconductor-dielectric interface is affected by field-effect doping [132], while semiconductor bulk carrier density is modulated by electrochemical doping [133]. In order to create OECTs with high conductance without enlarging the devices' width, scientists and engineers use the mass doping effect, which results in the relation between the transconductance g_m and d. Since the proportionality constant includes the product of volume capacitance C and charge carrier mobility, both of which are variables associated to both the electronic as well as ionic features of the polymer utilized to fabricate the channel, the proportionality is important for both device design and material development.

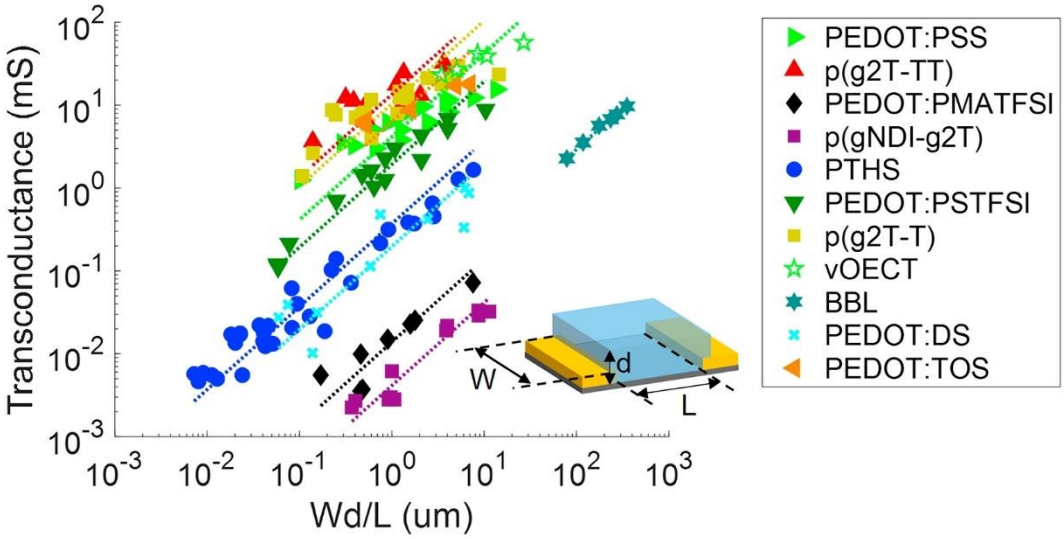

Figure 10 Peak transconductance as a function of the geometrical parameters of an OECT, for different channel materials. Reproduced with permission from [134].

The product between volume capacitance and mobility thus needs to be balanced and represents a performance metric for mixed ionic/electronic conducting materials. It follows that by creating OECTs with various geometries and taking into consideration the fact that transconductance is an indicator of the term *Wd/L*, one may evaluate the efficiency of materials. Another important characteristic that may be adjusted by changing the device topology is the speed at which the drain current of an OECT reacts to a change in the gate voltage. An exponential mathematical model using the RC time constant of the ionic circuit that can be represented between the gate electrode and the channel as its input may be used to adjust the rate of response for the current flowing throughout the semiconductor to a gate voltage step, and can be calculated as

$$\tau = R_S \cdot C_{CH} \tag{9}$$

where R_S is the resistance associated to the ionic solution and C_{CH} the channel capacitance. of the ionic current circuit modeled along the gate and the channel [135]. Impedance spectroscopy, for example, may be used to measure the solution impedance and the channel capacitance, demonstrating a direct correlation between the latter and the device's geometrical characteristics [136]. As shown in Figure 10, the slope of the curve highlighted gives the volumetric capacitance of the device. Considering one of the most used semiconductor polymer, i.e. PEDOT:PSS (poly(3,4-ethylenedioxythiophene):poly (styrenesulfonate)), is found

that its volumetric capacitance is set around 40 $F \cdot cm^{-3}$, but other materials are characterized by values in the range of up to 500 $F \cdot cm^{-3}$ [134]. The electrolyte resistance which is measured between the gate electrode and the channel, should scale with a proportionality constant equal to $[W \cdot L]^{-1/2}$ [137], [138]. When the scaling rules are combined, it becomes clear that the device's time constant is proportional to $d[WL]^{-1/2}$. One must assume that the response period for an OECT is identical to that of the equivalent ionic RC time constant for passive conductors if one wants to follow the criteria of the Bernards model mentioned in the following sections. With these hypotheses, the scaling rule for the time constants suggests that by reducing the channel's width and thickness, one may increase the device's reaction time while also lowering its transconductance. This implies that device shape must be meticulously planned depending on the purpose of the device. For instance, when using OECTs as brain activity sensors capable of detecting low frequency signals (40 Hz), it can be demonstrated that the frequency of such signals is not an issue, but the resulting amplitudes can become as low as tens of μV, needing significant amplification [139]. Due to this, OECT-based detectors for measures of neural activity should have high Wd/L ratios in order to obtain substantial enhancement of signals, even if doing this decreases bandwidth. On the opposite side, applications like single neuronal action potential monitoring or cyclic voltammetry with quick sampling necessitate the observation of higher frequency signals [140], OECTs should therefore be constructed with reduced $d[WL]^{-1/2}$ for such uses. The equivalent capacitance of two capacitors linked in series—one at the interface between gate and electrolytic solution, and one at the interface between solution and semiconductor, allows for the calculation of the channel capacitance of an OECT, namely

$$C_{eq} = [C_{G-E}^{-1} + C_{E-CH}^{-1}]^{-1} \tag{10}$$

From equations (7), (8) and 9 one can see that the transconductance is thus directly proportional to this quantity, while the response time of the device increases as the device capacitance decreases. In many applications, one has $C_{G\text{-}E} >> C_{E\text{-}CH}$, making the gate capacitance negligible. If the gate is made of a nonpolarizable material such as Ag/AgCl, the ionic charge can flow through the interface between gate and electrolytic solution, and the gate capacitance can be considered as an open circuit at low frequencies [141]. A little polarizable gate electrode may be utilized in some applications, and *Ceq* must be taken

into account. When enzyme processes take place at the gate electrode, for instance, a variation in the potential across the gate and electrolytic solution is generated, leading to a change on the gate potential and subsequently altering the channel current. In this scenario, OECT biosensors can identify analytes with this mechanism. This impact is underlined in Figure 11 for a rising amount of the molecule inside the electrolytic solution, demonstrating a significant difference in OECT behavior between the cases where the analyte is absent from the electrolyte and when it is present. The gate capacitance must be limited since the potential drop across the gate and the electrolytic solution is what drives this sensing mechanism. In some works, it is shown as the effective gate potential shift by a factor $1 + C_{E\text{-}CH}/C_{G\text{-}E}$ as the analyte concentration scales [142]. Some broad recommendations for improving the device performance by modifying its shape are provided by the relations stated for the transistor transconductance, sensitivity and bandwidth. Despite this, only at low frequencies (when ions have sufficient time to drift over the whole depth of the OECT channel) the volumetric capacitance scaling comes into play. This effect can be modeled by a characteristic frequency calculated as

$$f_{ION} = \mu_{ION} \cdot \frac{k_B \cdot T}{q} \cdot \frac{1}{d^2} \tag{11}$$

where μ_{ION} is the ion mobility inside the channel, k_B is the Boltzmann's constant, T the absolute temperature and q the elementary charge [143]. Since the ions are unable to penetrate the whole depth of the layer at frequencies beyond f_{ION}, only a portion of the channel is doped or undoped by the gate voltage, therefore the channel capacitance shows a sublinear dependency on thickness. The transistor behaves like a field-effect transistor at greater frequencies where the ions have no chance to enter the semiconductor [144]. The entrapment of ions in the polymeric semiconductor, or when ions fail to travel the complete length of the channel and thus the gate potential is altered, is an additional possible occurrence that might affect the device's characteristic frequencies. However, additional studies need to be done to determine whether this behavior exists and whether it can result in reversed OECT operation. Parasitic phenomena like overlapping capacitance and contact resistance can negatively affect bandwidth and *gm* in addition to these different frequency-dependent operating conditions. These effects are not covered by the scaling rules presented in this section [145]. Such effects are discussed in

further depth within Section 2.4, which also takes into consideration the effects of transconductance in steady state.

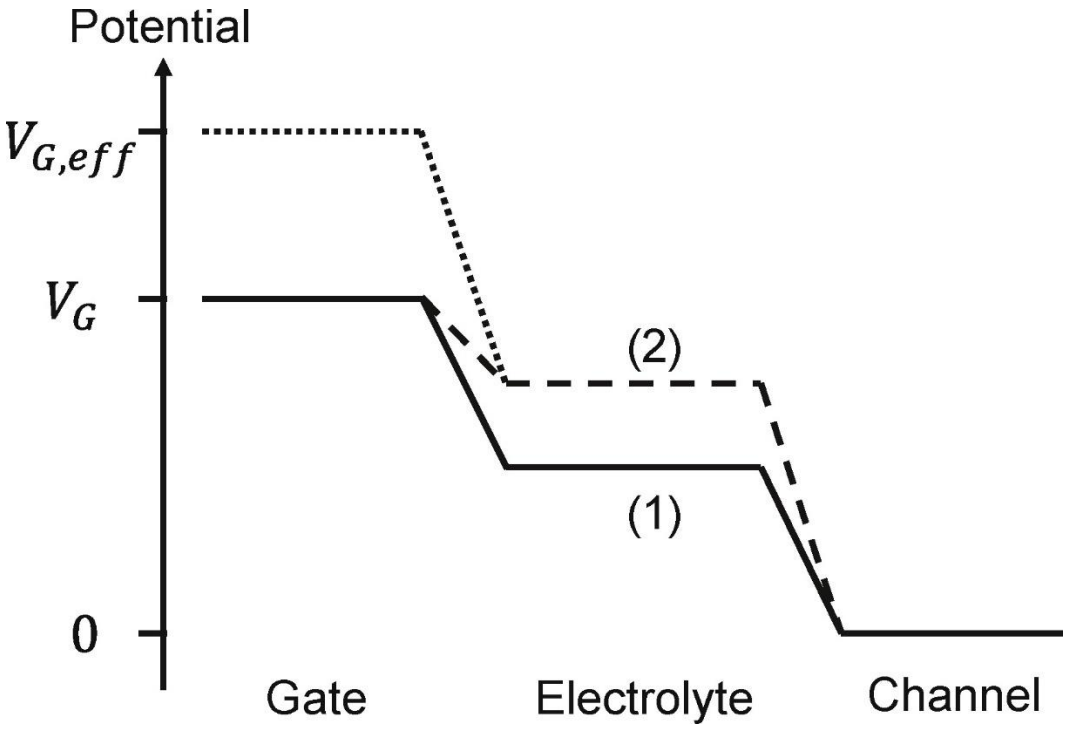

Figure 11 Diagram showing the trend of the potential in absence of the target analyte (solid line) and in presence of the target (dashed line). Dotted line shows the effective gate potential, required to achieve the same electrolyte potential when Faraidic effects are absent. Reproduced with permission from The Royal Society of Chemistry.

2.3 Transient effects

Starting with the Bernards model, the transient response of an OECT can be elaborated. The analogy with MOSFET devices is employed to explain the electronic transport effects that occur in the OECT channel. An equivalent RC circuit is also used to describe the ionic linking between the gate and the channel. In this part, we will take a closer look at more intricate mathematical models that explain how the transient gate current flow affects I_D and how to determine the transfer function's relationship to frequency. The transient response is modeled by Bernards and Malliaras by defining the estimation which the distribution of charges in the polymer at all times can be calculated through the steady-state solution for both source and drain potentials V_D, V_S, as well as by the time-varying electrolyte potential, $v_{G,sol(t)}$, written in smaller letters to emphasize its time dependence, as shown in the scheme in Figure 12.

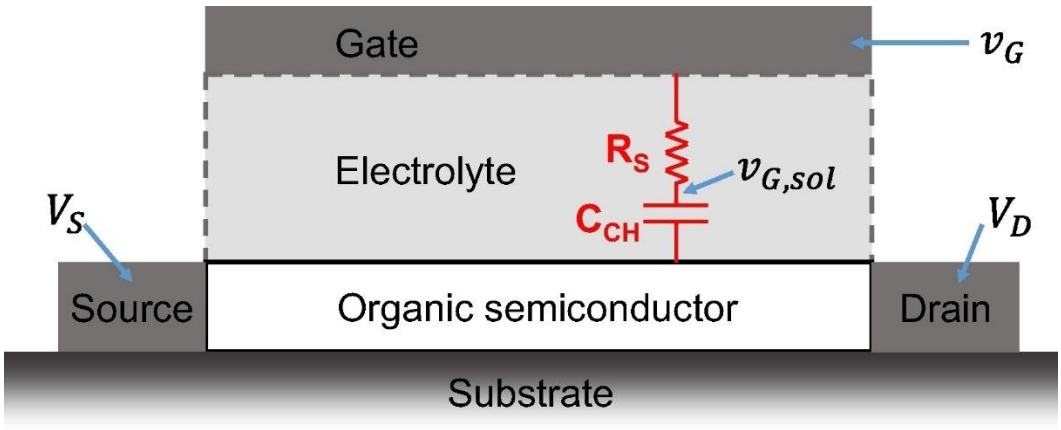

Figure 12 Schematization of the ionic circuit in an OECT when the gate capacitance can be neglected. Reproduced with permission from Elsevier.

The potential just mentioned, $v_{G,sol}$, is generated from the temporal response within this mathematical model, since the drain and source voltages are constant, causing the drain current I_D to depend only on the transient response associated with the corresponding ionic RC circuit. The displacement ionic current, $i_{G(t)}$, which is connected to the OECT channel's doping level, and the electronic transport current, $i_{CH(t)}$, which is related to the charge carriers' drift between the source and drain electrodes, may both be obtained after $v_{G,sol(t)}$ has been derived. The formula for $i_{G(t)}$ behaves as follows.

$$i_G(t) = C_{CH} \cdot \frac{dv_{G,sol}(t)}{dt} \tag{12}$$

while the electronic transport current can be calculated substituting $v_{G,sol}(t)$ in equations (4) and (5), namely

$$I_D = \mu C \cdot \frac{W \cdot d}{L}\left[1 - \frac{v_{G,sol}(t) - \frac{1}{2}V_D}{V_T}\right] \cdot V_D \;\; when\, V_D > V_G - V_T \tag{13}$$

$$I_D = -\mu C \cdot \frac{W \cdot d}{L}\frac{\left[v_{G,sol}(t) - V_T\right]^2}{2V_T} \;\; when\, V_D < V_G - V_T \tag{14}$$

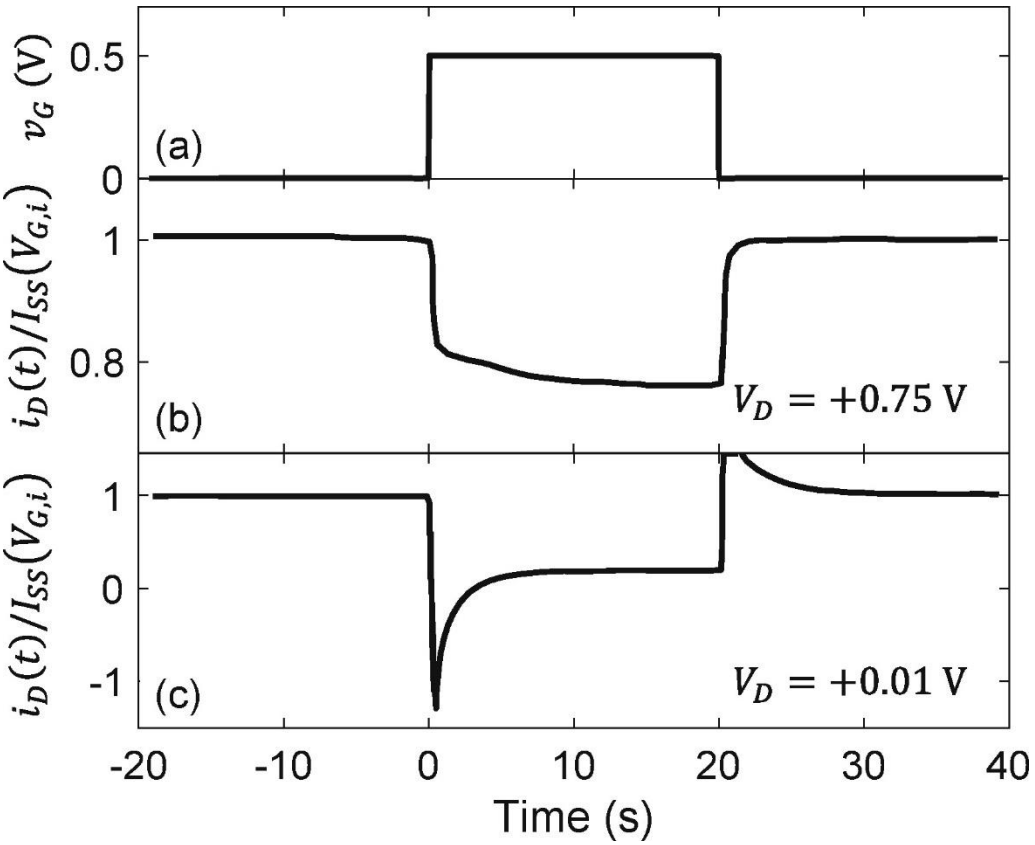

Figure 13 Transient response of an OECT when a square waveform is applied to the gate voltage when the ionic transport is faster than the ionic charging **(a)** and vice versa **(b)**. Reproduced with permission from John Wiley and Sons. Copyright 2016 WILEY-VCH Verlag GmbH & Co. KGaA, Weinheim.

According to the Bernards and Malliaras model, considering the situation of a quadratic gate potential, the time-dependent drain current $i_{D(t)}$ may be determined as a weighted sum of the displacement ion current and the drain current, namely

$$i_D(t) = I_{SS}(V_G) + \Delta I_{SS}\left[1 - f\frac{\tau_e}{\tau_i}\right] \cdot exp\left(-\frac{t}{\tau_i}\right) \tag{15}$$

where I_{SS} is the drain current in steady-state regime. In the first term of the latter equation, I_{SS} is calculated in the point V_G, ΔI_{SS} is calculated as $I_{SS}(t)$-$I_{SS}(0)$, f is a weighting factor defined as the fraction of the displacement ionic current directly contributing to the drain current, τ_e and τ_i are the transit time of a single charge carrier along the channel and the ionic RC time constant respectively. When the electronic transport in the channel is quicker than the ion charging, I_D relaxes from the starting value to the final one, as highlighted in Figure 13b, while as seen

in Figure 13c, I_D rises suddenly beyond the starting current value when the ionic charge is quicker than the electronic transport in the channel, and then it subsequently rises exponentially to the final current [146]–[148]. The weighting factor f highlighted in equation (15) has been investigated in several works, enriching the Bernards model. Assuming a constant value for f=1/2 (which is called the Friedlein Model), the OECT behavior is modeled through the scheme shown in Figure 14, with R_S and C_{CH} no longer dependent by the voltage [149]. In this scenario, one has

$$i_D(t) = i_{CH}(t) - \frac{1}{2} i_G(t) \tag{16}$$

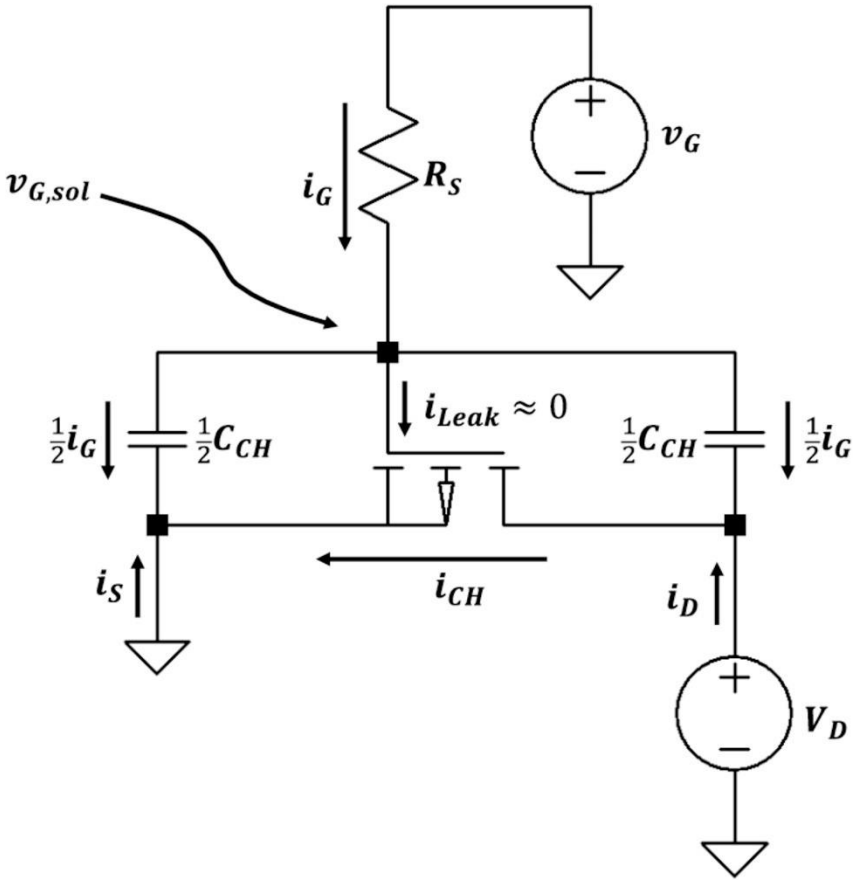

Figure 14 Equivalent circuit diagram of an OECT assuming a constant value for f=1/2. Reproduced with permission from John Wiley and Sons. Copyright 2016 WILEY-VCH Verlag GmbH & Co. KGaA, Weinheim.

Two significant conclusions may be determined by the above equation. The magnitudes for I_S and I_D are not identical in the transient response, and I_D follows a quadratic step from its starting value to its final value. No exponential relaxation occurs if the variation in channel current is precisely one half of the peak gate current. Considering the two regimes that were previously mentioned and underlined in Fig 13 helps to recognize this step reaction. By biasing V_D with the potential shown below, one may regulate the step response, which is located between these two regimes

$$V_D = \frac{L^2}{2\mu R_S C_{CH}} \tag{17}$$

The latter ensures the perfect balance between electronic transport time and ionic charge one. Since this mathematical assumption provides further insights about OECT behavior, it is only valid when $|V_D| << V_T - V_G$. To overcome this limitation, it is possible to assume that *f* depends both on the gate and drain voltages. This assumption takes the name of Faria's Model, an empirical expression for this dependence has been extracted from a mathematical fit of experimental data [150]. This method is useful to measure directly the *f* parameter, but with the drawback to require a distinct measuring channel to record the gate current. By monitoring the gate voltage's reaction to a quadratic step and comparing the heights of the spikes in I_G and I_D, it is possible to determine the value of f using this method. In either case, the assumption of a fixed value for $f=1/2$ previously outlined, but still without a clearly defined mathematical model, is refined by the empirical derivation of the frequency *f* by fitting or by measuring it directly. By integrating across the mobile charge carriers in the channel and assuming that a fraction *x/L* of the carriers at location x along the channel contribute to the drain current and the remaining fraction to the source current, a solution to this problem may be discovered. This statement is converted into a voltage-dependent value of the parameter *f*. According to experimental data, this situation yields an analytical formula for both the source and the drain current transitory behaviors [151]. It is also possible to get a description for the frequency f that describes the charge carrier fluxes in OECT using a transmission line framework or a finite element time-dependent model. To compute the contribution of the displacement ionic current to the drain current, these models are used to compute the time-varying currents at each location in the channel, which eliminates the need for an explicit f-factor. The voltage-dependent capacitance of the transistor may be used

to represent the transmission line-like idea, and it could be modified to characterize the transient response of OECTs [152]. To the contrary of this model, it is possible to undertake a finite element computation involving the time-dependent two-dimensional drift diffusion for both electrons and ions in the OECT channel, demonstrating that its effects are qualitatively comparable with the ones of the quasi-static models [153]. To confirm such models and demonstrate their accuracy in the high-frequency band, in which the quasi-static theory is predicted to fail, additional experimental data are required [154]. Overall, the models covered above offer estimations regarding the transient behavior of OECTs, which is helpful for the creation of materials and equipment employed as active channels in the transistors [155]. The challenge of restoring an unknown voltage input, which frequently occurs in biosensing investigations of electrogenic cells like heart cells or brain cells, is also addressed by the transient models, which enable researchers and engineers to derive unknown voltages from recorded current responses. Due to the characteristic polarization that occurs in their membranes, electrogenic cells can produce spontaneous voltage signals, and if these signals are recorded with an OECT, they can provide a response [156]. The voltage produced by the electrogenic cell is the primary signal of interest in these types of investigations, even if also the drain current generated by the OECT is monitored. By fitting the data from the calibration to a polynomial basis set to approximate the transfer function H(s) associated with the device, or by utilizing Fourier transformations to avoid polynomial decomposition, one may determine the input voltage [150]. The input voltage $V_G(\omega)$ can be determined as the inverse Fourier transform of $V_G(\omega)=I_D(\omega)/H(\omega)$, where $H(\omega)$ is given as a function of the radial frequency, $V_G(\omega)$ and $I_G(\omega)$ are the Fourier transforms of the voltage across the gate and drain current, respectively. In the latter assumption, $H(\omega)$ can be determined through calibrating the device via impedance spectroscopy. It has been demonstrated that, in both of these models, employing transfer functions using transitory models yields more accurate results than supposing that the change in gate voltage is related to the variation in drain current. The measured current in response to a spike in the gate voltage is highlighted in Figure 15a, and the Friedlein model's mathematical estimation based on the assumption that $f=1/2$ is correct is displayed in Figure 15b. This prediction also accounts for the time delay among the signal and the current response, as well as the imbalance in the current response caused on by the shift in sign for the gate current during the voltage peak, which is well described in Figure 15c and 15 d, where the outcome for the Faria hypothesis is emphasized. This also shows that, in such models, the imbalance and the time latency are more prominent for bigger OECT channels.

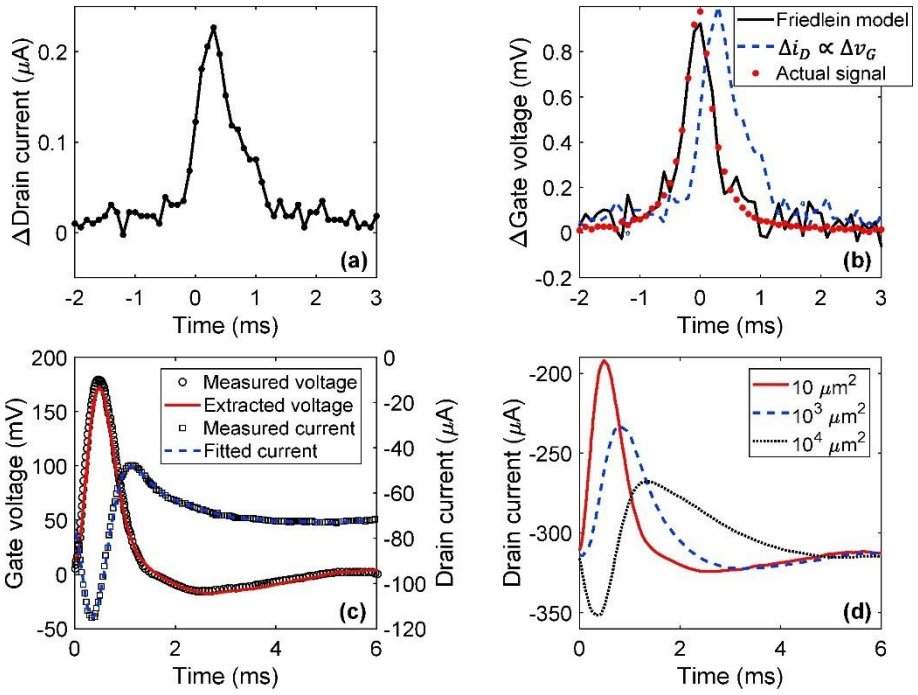

Figure 15 Current response to a voltage spike **(a)** on the gate electrode between different models. Comparison between Friedlein Model and the assumption of proportionality between drain current and gate voltage **(b)**. Fitting of the gate voltage in the Faria's Model **(c)**. Simulation on drain current for different channel areas **(d)**. Reproduced with permission from Elsevier.

In conclusion, the models just mentioned employ an RC circuit to represent the electrolyte and a progressive channel approximation to characterize the organic semiconductor in the transient behavior of an OECT. These mathematical models for discrete-element circuits adopt the assumption that the transient distribution of charges in the channel is approximated quasi-statically, showing the dominant effect of the ion charging circuit over the temporal response of an OECT. Despite the fact that these models are helpful to explain OECT behavior, the more precise approach would be to abandon the quasi-static method and instead use two-dimensional finite element simulation in the domain of time, as has recently been reported, taking into account the difficulty of establishing a balance between reliability and ease so that the theory can be tested experimentally.

2.4 Series resistance

The results presented in the preceding sections were determined under the assumption that the resistance in the device channel is larger than the resistance at the source-drain electrodes and the resistance across the conductors connecting

the source-drain contacts to the power supply. Although it is frequently acceptable to assume that the channel resistance predominates the device response, there are some situations when parasitic resistive devices are connected in series between the channel and the power source. Such parasitic resistors may decrease the device's performance and make the earlier findings invalid. The impacts of parasitic resistance in OECTs are discussed in this section, along with how they may affect OECT performance and possible mitigation measures. It can be proven that the resistance dependent by V_G which can be modeled in series with the OECT channel when employing the transmission line approach. An empirical model for this resistance's dependency on the gate voltage has been demonstrated, and it may be described as a contact resistance at the junction between the metallic source-drain electrodes and the polymer semiconductor channel [157]. In this scenario, it is also shown that this form of voltage-dependent contact resistance can result in a transconductance not dependent on the gate voltage. The channel resistance in series with the contact resistance can also result in an increase of the overall electric noise of the device by several orders of magnitude, a relatively high current flows in the device's channel [158]. Although the fact that these models give an explicit explanation of the impacts associated with contact resistance in such devices, physical evidence of its genesis is still lacking. It has been proposed that the parasitic resistance may occasionally result from ohmic resistance of the metal interconnects linked in series among the power supply and the source-drain terminals rather than contact interactions at the metal-semiconductor interfaces. The parasitic series resistance, which has a direct impact on device performance, may be demonstrated to be 10% larger than the resistance of the channel of an OECT with a high *Wd/L* ratio [157], demonstrating how the performance of the OECT channel can be impacted by parasitic resistance when it is in series with the channel. As previously indicated, parasitic resistance can influence the transconductance along with noise level when an OECT is operating, causing a deformation of the output and transfer characteristics and lowering the frequency at which the device's gain approaches the value G=1 [159], [160]. Inaccurate calculation of crucial device and channel material properties including, carriers mobility, threshold voltage and voltage swing in the domain below the threshold, which is another side consequence of parasitic resistance [161], [162]. Nevertheless, some manifestations of parasitic resistance in such transistors, are voltage independent. This makes understanding the dependency of parasitic resistance on the gate voltage a significant problem for study in the field of such devices. Parasitic resistance may be demonstrated to decrease the transconductance in standard MOSFETs and, therefore, on devices

with intrinsically non-ideal behavior, such as those impacted by disorder in their semiconductor, which we will investigate in the following session. It is evident that the geometric scaling described in Section 2.2 may be utilized at high Wd/L percentages, when the resistance constitutes a larger proportion of the overall resistance, as the drawback of parasitic resistance is more pronounced for devices with significant transconductance. This effect has been demonstrated experimentally for short-channel devices having line resistance on the order of tens of Ohms, as illustrated in Figure 16b, for simulations of transistor measurements [163], Although the line resistance begins to take precedence in devices with *Wd/L>2* µm, the resistance of the channel can reach hundreds of Ohms. The transconductance in this working area meets a plateau at 20 mS rather than increasing as the ratio *Wd/L* does. It has been demonstrated that monitoring the OECT conduction resistance and employing this parameter to compute the intrinsic transconductance leads in an intrinsic transconductance rise as the ratio Wd/L grows, also for devices in which the *Wd/L* ratio is greater than 10 µm, in order to explain this behavior. The intrinsic transconductance exhibits a non-monotonic dependency on gate voltage due to the parasitic resistance's impact on the highest point of the transconductance, which shifts to higher positive gate voltages. According to the previously described concept, a series resistance with a constant value might cause the observed transconductance's peak to shift towards 0 V. Once more, this impact is mostly seen in devices with high transconductance, and as it scales on geometry, it may appear that the highest level of transconductance is affected by geometry [164].

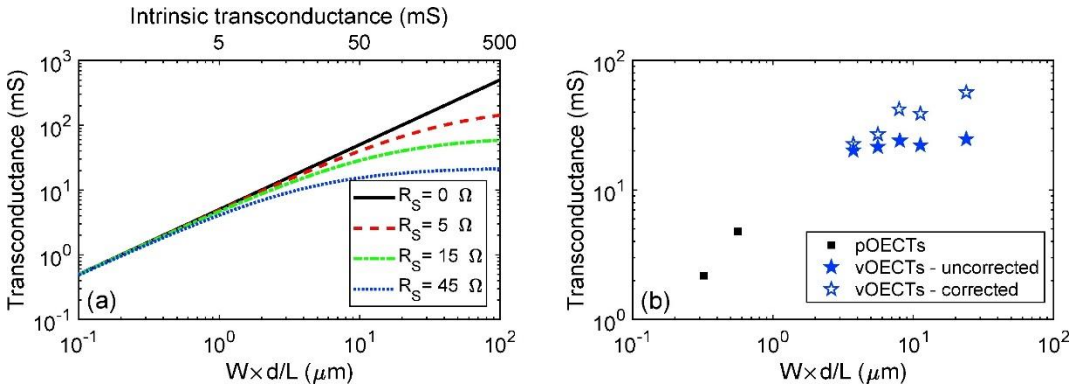

Figure 16 a) Transconductance as a function of the geometry of the OECT, when considering different series resistance values. **b)** Measured transconductance values as a function of the geometry of the device, for planar OECT channels (squares) and for vertical ones (stars). Reproduced with permission from **[163]**.

Whenever the aim is to precisely define the material properties or to maximize device performance will determine the appropriate approach to handle the aforementioned impacts. The approach is really simple in the latter scenario. Developing devices with big channel resistances so that overall parasitic resistance is a significant part of the overall resistance yields more precise parameter estimations. This eliminates the disruptive effects of contact resistance and line resistance. Using the Kelvin four-terminal sensing is another technique to reduce the impact of series resistance. This measuring method uses probes that sense the channel voltage without drawing current, thus they are not impacted by the line or contact resistance [165]. Despite employing four-terminal sensing and raising channel resistance are good ways of entirely removing the impacts of contact resistance whenever assessing the polymer qualities, these techniques are frequently ineffective when used in applications which ask for high performance devices. For instance, a drop in transconductance brought on by an increase in channel resistance would result in a reduction in the signal being measured for transistors employed as biosensors. Four-point sensing is also complicated to employ in higher-density OECT systems or even when power supply sources are hard to reach. In these circumstances, performance decline is a result of parasite resistance. For instance, a sensor array with extremely broad metallic links connecting the devices and the energy source may be created. While doing so would completely eliminate the impacts of line resistance, it will ultimately end in a smaller number of transistors on the chip, which would lower the sensor array's spatial resolution. These methods offer some suggestions on how to mitigate the effects of parasite resistance. However, if more research identifies the root reasons of parasite resistance in OECTs, more specific design guidelines may be produced. For instance, discovering that parasitic resistance in OECTs is mostly caused by contact resistance rather than conduction resistance would directly improve OECT devices from years of research on contact methods for OFETs [166]–[168]. This strategy still needs OECT-specific investigations because certain approaches used for OFETs may not work as well for OECTs. For instance, contact doping is commonly employed to reduce contact resistance in OFETs, but this approach might not be effective in OECTs in which the density for ions and electrons can be as high as 10^{20} cm^{-3}, a value in the exact same order of magnitude as many examples of doping levels used to reduce contact resistance. [169]–[171]. Contact resistance evaluations are crucial for the design of OFETs, but they are also difficult to conduct. There are significant problems in the majority of methods used to measure contact resistance and its relationship to gate voltage. For instance, the transmission line mode, a widely

used technique for measuring contact resistance, depends on studies on several devices with various channel lengths. The output of this model frequently produces false findings when there are considerable differences in contact resistance, mobility, or capacitance between devices [172]. Furthermore, the linear section of the transistor response must be used to obtain the overall resistance for the transmission line model. An incorrect extracted resistance may be the result of a too-narrow drain voltage range. The fact that the gate voltage affects the linear behavior's broadness in the drain voltage spectrum further draws attention to this issue. The transmission line approach can be substituted with the gated four-wires sensing method, which does not require measurements on several devices to determine the contact resistance. The voltages observed in the OECT polymer must, however, be extrapolated in order to use this approach. If the form of the voltage profile close to the source-drain connections is assumed to be wrong for this quantitative extrapolation of the voltage, the extrapolated voltage will be erroneous [173], [174]. Despite the fact that this flaw does not limit the capacity of gated four-wire sensing measures to completely exclude the impact of contact resistance, it may reduce the precision of the estimation of contact resistance when employing this technique. Since the voltage may be measured with much finer precision than is feasible with the gated four-wire sensing, the margin for error related to extrapolating the channel profile of voltage can be eliminated by employing the Scanning Kelvin probe microscope approach [175]. There have not been any measurements using this approach in OECTs, though, most likely because it is impossible to take into account the charge shielding done by ions that move in the solution over the transistor channel. Another effective technique for measuring contact resistance is impedance spectroscopy, which depends on a precise corresponding circuit representation of the transistor and allows for a reduction in the frequency dependence of both the channel impedance and the contact impedance [176]. A new way to determine contact resistance in such devices may need to be created, or many existing methods may need to be combined for cross-verification, given the shortcomings of these traditional measurement techniques. Overall, the debate in this section demonstrates the interest in future study of parasite resistance in such devices due to a number of factors. According to a number of studies, OECT effectiveness is negatively impacted by parasite resistance. Second, it is unclear what is causing this parasite resistance. Finally, decades of study have produced strategies to reduce different types of parasitic resistance in OFETs and traditional transistors, but these strategies will not be applicable to OECTs until researchers completely comprehend the physical process underlying parasitic resistance in such devices.

2.4 Crystal structure of organic semiconductors

The analyses highlighted in the sections above explains the transistors behavior when evaluated from the viewpoint used to define traditional inorganic transistors. For instance, multiple models including bulk capacitance and distribution of charge schemes that follow physical descriptions originally meant for describing inorganic semiconductors, along with parasitic consequences that can be recognized employing identical frameworks developed to describe MOSFETs, are used in the Bernards-Maillard model, which assumes the drain current is defined in the long-channel condition [177]–[179]. Although the aforementioned models offer qualitative guidance that helped in the creation of OECTs, these are only quantitatively correct over a limited range of voltages. Several models that take these issues into account are compiled in this section along with a discussion of how the unique physical characteristics of organic semiconductors impact the transportation of charges and capacitance in OECTs. For many years, researchers have been investigating the transport of charges in polymer semiconductors. Over the past two decades, a large number of studies on this issue have been produced [180]–[183]. Since polymeric semiconductors are not made up of single crystals, a lot of study in this field focuses the impact of structural disorder. In reality, the majority of the semiconductor channels utilized to create OECTs are semicrystalline with amorphous portions around nanometer-sized crystallites rather than polycrystalline materials [184]. The absence of an extended crystalline structure precludes the charge carriers' wave functions from propagating across the whole polymer film. Charge carriers must "hop" by means of a number of localized states through heat aided quantum mechanical tunneling in order to travel from one crystallite towards another, which is a much slower process than transport in single crystals regardless of whether charge carriers are delocalized throughout the entire crystallite or polymers chain [185], [186]. As a result, the hopping frequency within the semi-crystal structure determines the polymer's macroscopic conductivity [187]. The hopping process is a tunneling phenomenon, and as the dimensions of the potential barrier has a significant impact on this process' pace, so do the physical separation between the sites and their respective energies. The density of states within a semiconductor, that can be described as the amount of locations per volumetric unit and unit energy, describes these properties. Since the energy dependence of the density of states is established by the energetic contributions made by microscopic features of the polymer, including randomly directed dipoles, intermolecular twisting, and geometric deformations, the degree of chaos in polymer semiconductors invariably affects

this parameter [188]–[190]. Although several publications offered different explanations for the density of states' dependency on energy, there is almost universal agreement that this quantity rises super-linearly with energy, especially when taking into account low energy values [191], [192]. Since the sites are far from one another in both location and energy when low energies are taken into account, the charge carriers within the polymer only fill the sparsely populated sites, leading to a low density of states and a delayed hopping process. The number of charge carriers in a semiconductor increases when they start to occupy denser-packed sites with higher energies, which speeds up the process of hopping between sites and, as a result, increases carrier mobility [193], [194]. During the last years, OECT models have been proposed, in which the dependence of the mobility by the carrier concentration is highlighted. Given p the carrier concentration in the semiconductor, and μ_0 the mobility when $p=p_0$, a mathematical model for the relationship between μ and p is given by

$$\mu = \mu_0 \left[\frac{p}{p_0}\right]^a \tag{18}$$

where a is a constant term which depends on the shape of the density of states [195]. The dependency of the mobility on the power factor a distinguishes this model from the Bernard-Maillar one, highlighting the situation in which OECTs must be characterized using the physics for disorganized semiconductors. The output and transmission characteristics of OECTs are qualitatively described by Bernards model, as seen in Figure 17. Additionally, when the gate voltage is adjusted between the range of 0-0.25 V, it quantitatively matches the transfer profile for the given transistor, but when the voltage range is expanded to 0-0.4 V, it does not. Although it includes an extra fitting parameter, the power-law mobility much outperforms the Bernards model statistically in terms of how well it fits the data across this larger voltage range. Perhaps the power law mobility theory is inadequate when taking into account gate voltages that are more lower compared to those where maximum transconductance happens (for instance, 0 V for PEDOT:PSS channel). In particular, it is unable to explain the transconductance's non-monotonic dependency on the gate voltage. Numerous writers that have worked with different polymeric semiconductors, including polythiophenes, polyanilines, polypyrroles, polyacetylene, and ladder-type polymers, have documented this behavior, which is seen in Figure 17 [196]–[199].

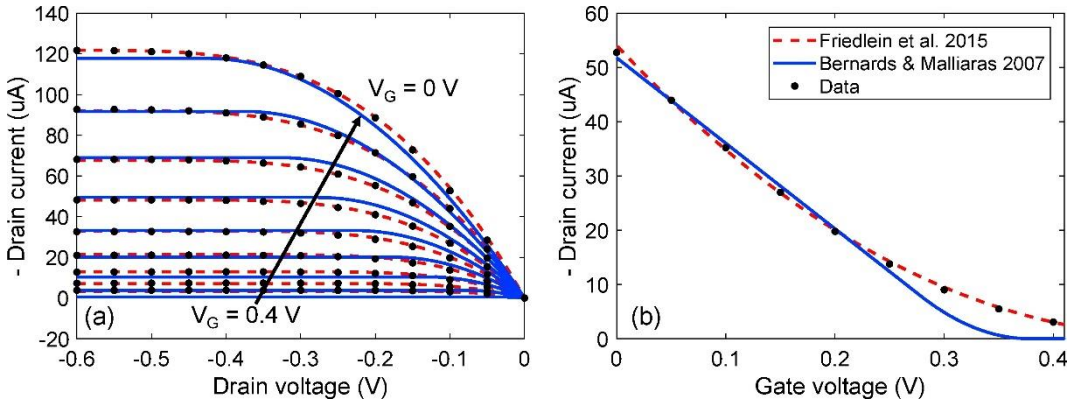

Figure 17 Output curves **(a)** and transconductance curves **(b)** for OECTs when considering the Friedlein Model (dashed, red) and the Bernards Model (solid, blue). Reproduced with permission from [195].

Additionally, OECT devices with various electrode geometries and those made with various fabrication processes are characterized by non-monotonic transconductance [200], [201]. Furthermore, systems with source-drain electrodes consisting of platinum, gold, PEDOT:PSS, or carbon exhibit similar behavior [202]. One explanation for this behavior is that the voltage-dependent contact resistance, which was discussed in the previous section, is what causes the non-monotonic transconductance. However, this explanation is unlikely to be accurate for such an extensive variety of implementations, and it is unable to account of the non-monotonic transconductance within gated four-wires sensing probe measures of such devices. Additionally, the previously described exponential relationship between contact resistance and gate voltage is insufficient to account for the negative transconductance seen at very high carrier densities [203]. Since the density of states themselves is non-monotonic, several other researchers have also hypothesized that the non-monotonic transconductance may take place. Since integration across all energies would produce an unlimited number of states, the superlinear densities of states previously stated can only be accurate at low energies. As a result, with greater energies, the density of states should saturate and eventually decline. Theoretical study and practical observations demonstrate that when the carrier concentrations exceeds its maximum achievable value, the saturation point of density of states becomes significant [204]. This results in a sublinear dependency between the carrier mobility and carrier concentration. A non-monotonic transconductance results from the change from a super-linear dependency at low carrier concentrations towards a sub-linear one when taking into account greater ones. As the carrier mobility declines as one increases carrier density, as has been recorded in some circumstances, the transconductance may

turn negative when the carrier density is determined to be above 50%. A non-monotonic density of states model has just been given, demonstrating how well it fits observations of the non-monotonic transconductance in such devices made using four-wire sensing. This section's discussion have currently focused on how charge transport is impacted by hopping transport and the architecture of the semiconductor's density of states. However, since channel capacitance in OECTs is governed by the buildup of charge carriers, the structure of the density of states additionally has an impact on this property. The capacitance can be expressed using the following relation

$$C^* = q\frac{dp}{dV_G} \tag{19}$$

since the charge carriers are fermions, one can calculate the carrier concentration as the convolution between the density of states *g(E)* and the Fermi-Dirac distribution *f(E)*, namely

$$C^* = q\frac{d}{dV_G}\int_{-\infty}^{\infty} g(E) \times [1 - f(E)]dE \tag{20}$$

Different approaches to handling this voltage-dependent capacitance while characterizing OECT activity have been described by researchers. For instance, a lot of models rely on the constant assumption that the gate-channel capacitance. The link among gate voltage and chemical potential is rather problematic as a result of this assumption, but it offers an analytical equation for carrier density and makes it easier to simulate circuits using OECTs [205]. Additionally, experimental data indicates that the gate-channel capacitance relies strongly on the gate voltage when low and high charge carrier densities are taken into account, contradicting the assumption of constant capacitance, which shows that the capacitance only weakly depends on the gate voltage upon moderate carrier densities. By assuming that the electron chemical potential is connected to both the gate voltage and an offset V_0 that relies on the material of the gate electrode and the chemical composition of the electrolyte solution, researchers have approximated the capacitance in these areas [206], namely

$$E_F = q(V_G - V_0) \tag{21}$$

With this assumption, equation (20) can be easily solved, and the approximate result for low temperatures can be found to be

$$C^*(V_G) = -q^2 g[q(V_G - V_0)] \tag{22}$$

Equations (20) and (22) are useful not only for describing OECT behavior but also for measuring the density of states [207]. Nevertheless, equation (20) is difficult to solve and equation (22) is incorrect whenever a voltage drop exists at the gate-electrolyte contact or in the electrolyte. The aforementioned voltage drop, impediment to ion buildup within the channel, or nonuniform distributions of charge transporters in the OECT channel are all taken into consideration in more complex formulations of the capacitance related with the gate-channel interface [208]. The formation of charge in an OECT channel may be demonstrated to be voltage-dependent and to diverge considerably from simply capacitive accumulation of charge at low carrier concentrations, in particular when all these effects are taken into consideration. In conclusion, the behavior of OECTs is complicated by the physics of disorganized semiconductors. When applied to narrow gate voltage ranges or intermediate carrier concentrations, some mathematical models that ignore these complexities frequently succeed, but they fall short when applied to high and low carrier levels. Particle mobility and gate-channel capacitance in such devices are highly dependent on carrier concentration in these regions. By taking into account the density of states and the charge transfer that is dominated by leaps, these complexities may be understood. The metal-insulator transition, charge-carrier-dopant culombic relationships, ion-induced film swelling, and polaron binding energies are just a few examples of additional phenomena that are not included by these modifications to traditional models, making them incorrect in some instances [209]–[212]. The creation of experiments that focus on isolating each of these issues is a significant problem for OECT research, and it must be supported by the equally significant effort of determining whether to incorporate these issues in device models and when to exclude them for the purpose of simplicity.

Chapter 3

Open-source Culture Platform for Multi-Cell Type Study with Integrated Pneumatic Stimulation

3.1 Introduction

Recent research has demonstrated that the microenvironment around cells may impact cancer development in addition to genetic abnormalities [213]. Solid stress, high fluid pressure, enhanced interstitial flow, and matrix mechanics are just a few examples of how biomechanical factors may change the tumor microenvironment, leading cancer cells to migrate to neighboring tissues and finally metastasize [214], [215]. Numerous research has examined at the connection among mechanical forces and carcinogenesis in recent years, discovering connections between modifications to the architecture of normal tissues and their transformation into precancerous states [213]. Breast tumorigenesis has also been linked to collagen cross-linking, extracellular matrix (ECM) stiffness, and enhanced focal adhesions [216]. Thus, it is evident that shifted microenvironmental circumstances and mechanical forces play a role in carcinogenesis and that cancer cell phenotype may be more significant than cancer cell genotype [213]. By releasing alert signs during necrosis, mechanical pressure onto cells may cause autolysis and encourage the attraction of immune system cells to cancer tissue [217]. Several studies illustrating the impact of

mechanical compression upon both healthy and malignant tissues have been done, such as neurons [218], brain [219], fibroblasts [220], [221], lung [222]–[224], breast [219], [225], ovary [226], [227], and heart [228], [229], leading to invasive and metastatic types in malignant tissues and inflammations, delayed healing, and fibrotization routes in healthy tissues. Despite the fact that several tools have been created and put to the test to examine the cultivation of cells response and growth under cyclical and static compression [111], [218], [219], [230], [231], There aren't many adaptable systems that are perfect for use with multi-well cell culture methods. Numerous studies also show that the applied compression stimulus's strength might vary from 3 to 6.5 kPa, with this value potentially being increased to the physiological 3.7-18.9 kPa predicted to occur in tumor settings [226], [227], [232]–[234]. Therefore, more research is required to determine the type and degree of mechanical compression which significantly alters the tissue microenvironment [215]. In this study, we describe a flexible dynamic cell culture system that operates in a CO2 incubator and allows a controlled hydrostatic compression stimulus to be delivered to a typical multi-well plate tissue. A diaphragm pump that can adjust differential pressure up to 12 kPa and a proportional solenoid valve which returns the chamber to atmospheric pressure may be used to control the hydrostatic pressure in a polymethyl methacrylate airtight chamber where the plate is installed. An Arduino nano-microcontroller regulates the feedback from a differential pressure sensor and a temperature sensor, which gather environmental data in the culture chamber, and acts on the working times of the pump and solenoid valve. With a computer, the system may be readily configured to change the length of each compression stimulus and, in the case of cyclic compression, its duty cycle. Preliminary experiments with cells were conducted to make sure the system runs in cyclic positive compression state and tries to match the frequency of human breathing in order to assess the device's biocompatibility.

3.2 Materials and Methods

3.1.1 Design and Development of Culture Chamber

A CAD program (Rhinoceros 5, Robert McNeel & Associates) was used to design the cell culture chamber, and a computer driven milling machine (Benchman VMC 4000) was used to manufacture it. The chamber is made up of a translucent box that can hold a typical multiwell plate and has a very straightforward design. Eight steel screws were used to secure three polymethyl methacrylate (PMMA)

plates in a sandwich configuration. Section 4.2.1 provides a full description of the culture chamber's development.

3.1.2 Design and Development of Electronic Circuit

Figure 18 displays the system's block diagram. The Arduino Nano® 3.0 board, a programmable chip built on the ATmega328 microcontroller, is at the center of the circuit. In order to upload the required C++ code, the board may be linked to a PC through a USB port. The board also has fourteen pins for digital input and output, that can be used to monitor their low or high state while in input mode or to set an appropriate high or low state if in output mode. It also has 8 analog input pins, which can read and convert multiple analog signals from a wide range of sensors into readable form. The system has a temperature gauge (Honeywell, Charlotte, NC, USA, HIH6130 series) that connects to the Arduino using its digital I2C pins to track the temperature in the culture chamber while it is in use. In order to monitor the pressure attained at each cycle during operation, a pressure sensor (NXP, Amsterdam, NL, MPX5100DP) has been attached to the culture box and interacts with the Arduino using its analog ports. The board itself, which has two constant output voltages of +3 V and +5 V, powers both sensors. A pneumatic system on the platform may adjust the level of pressure in the culture chamber: The pressure is increased (or decreased, depending on the application) by a diaphragm pump (TCS Micropumps, Faversham, UK, D3K series), and it is precisely and steadily returned to atmospheric pressure by a typically closed proportional solenoid valve (255667, Burkert, Ingelfingen, Germany, DE). To configure the required frequency for the pressure cycles as well as, in the case of the pump, to set the ideal flow rate, each solenoid valve and pump have their own circuitry that is managed by Arduino. The Arduino board may be powered in two distinct ways: either using an external DC power supply or by connecting the USB cord to a computer. So that the PC may finally be unplugged after the appropriate parameters are defined, this system is outfitted with a DC power supply that is specifically designed for use with Arduino. Finally, an AC/DC switching power source (Mean Well, New Taipei City, TW, RS-25-12) which transforms the AC main power supply to 14 V DC (V_{DD}) is used to power the system. Figure 18 depicts the whole electronic circuit that will be covered in more depth hereafter, with all of the blocks that were covered in this part highlighted. Three 220 Ω pull-up resistors are used to connect an RGB LED to the Arduino's digital pins D6, D7, and D8 in the schematic, and their purpose is to display a

distinct color (red or blue, respectively) when the pump or solenoid valve is operating so that the system's proper operation can be more clearly seen.

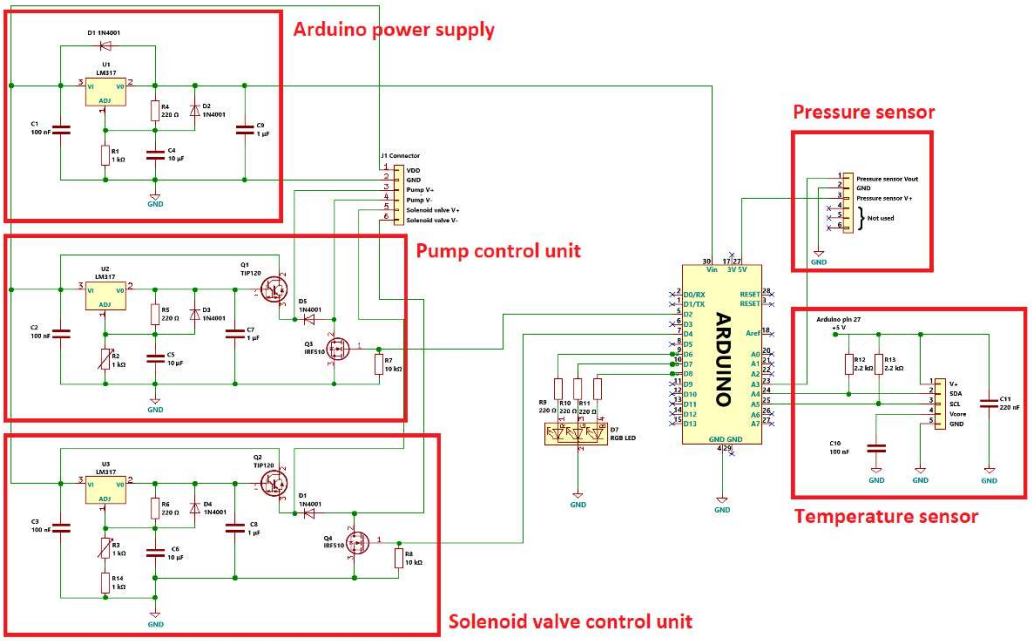

Figure 18 Electronic circuit of the system and its main blocks.

3.1.3 Arduino Power Supply Design

As previously indicated, a separate DC power supply with a voltage in the 7–12 V range can power an Arduino board. To decrease the value according to the Arduino input range, it was important to take into account the switching power supply DC output of 14 V, which supplies all of the circuit's components. Employing a linear voltage controller (LM317BT, STMicroelectronics, Geneva, CH), the circuit in Figure 19 was constructed. By default, this device is kept at an operating voltage of 1.25 V (V_{REF}) across the adjustment and output pins (V_{OUT}-V_{ADJ}), and the input voltage (V_{IN}) controls the circuit's maximum voltage swing. A 10-µF capacitor (C4) was inserted between the adjustment port and ground to increase ripple rejection, a 1-µF output capacitor (C9) was employed to improve transient responsiveness, and a 100-nF bypass capacitor (C1) was utilized to decrease any AC component of the input voltage. The circuit additionally included *D1* and *D2* as a pair of protective diodes. Input short circuit protection for the regulator is provided by the first, while output short circuit protection is

provided by the second. The voltage divider produced by both resistors R4 and R1 is where the output voltage is linked, and it responds to the ideal law

$$V_{OUT} = \frac{R_1 + R_4}{R_4} \cdot V_{REF} + I_{ADJ} \cdot R_1 \quad (23)$$

where R4 is advised by the supplier to be around 240 Ω, and the second term is often inconsequential as it is typically two orders of magnitude smaller than the first. The requisite minimum resistance value for R1 may be easily established because the Arduino board needs an output voltage of at least roughly 7 V. on this study, R4 was a 220- resistor from the E12 series, giving an R1 value of 1012 kΩ, which is equivalent to a 1 kΩ resistor from the E12 series that is readily accessible on the market.

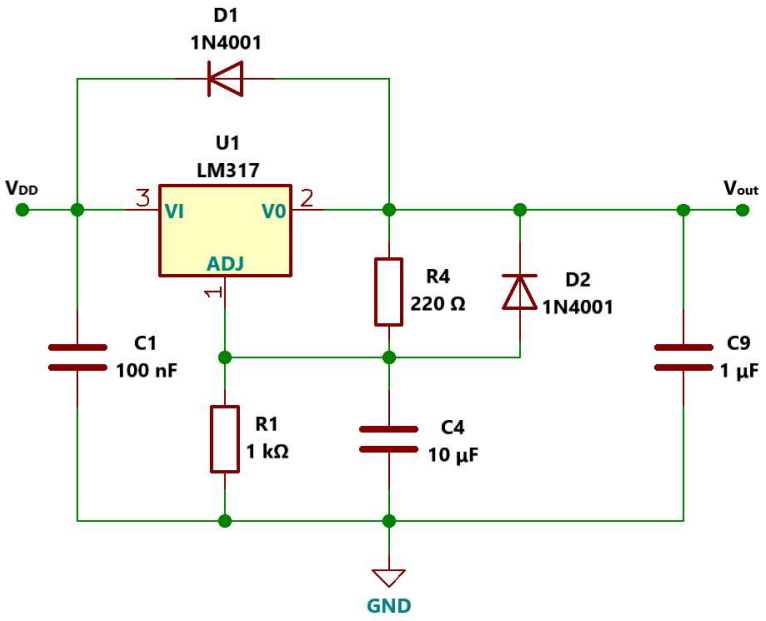

Figure 19 Arduino power supply circuit developed using an LM317 linear voltage regulator and passive components.

3.1.4 Pump Power Supply

The voltage regulator discussed in the preceding section serves as the foundation for the pump's power supply circuit. The diaphragm pump features two distinct inlets and outputs that may be connected either in series or parallel depending on whether the application calls for a larger maximum differential pressure or

vacuum but a lower flow rate. A maximum flow velocity of 3.5 l/min and a maximum differential pressure (both positive and negative) of 0.41 Pa and -0.39 Pa, respectively, were achieved in this work by connecting the pump in parallel. The pump voltage, which can be changed from a minimum of 2 V to a maximum of 6 V, may be used to change the flow rate. In order to produce a linear change of the output voltage, a precision potentiometer with 1 k and ten turns (536-1-1-102, Vishay, Malvern, PA, USA) was used in place of the adjusting resistor in the pump control circuit shown in Figure 20. To stop reverse voltage from leaking during the transient period of the pump shutdown, a safety diode D5 was connected across the terminals of the pump. A power BJT (TIP120, STMicroelectronics) in a Darlington configuration was connected straight to the V_{OUT} pin at a maximum voltage of 6 V. The collector of the power BJT was connected to V_{DD} together with the pin used for input of the voltage regulator. The negative terminal of the BJT was attached through the drain of an n-channel MOSFET (IRF510, Vishay), whose source was directly connected to ground. The positive pump terminal was supplied with power from the BJT's emitter. A digital Arduino connection D2 and a 10 kΩ pull-down resistor were both connected to the MOSFET's gate. The circuit's maximum current range was extended by the BJT such that it served as the primary conductor for current instead of the voltage regulator. The Arduino controlled the MOSFET's ON and OFF states, acting as a switch. The circuit's branches, V_{BE}, V_{PUMP}, and V_{DS}, were all affected by the regulator's output voltage, or V_{OUT}. The voltage regulator produced a minimal output voltage of 1.3V whenever the value of the potentiometer was adjusted to its lowest point. In this setup, the BJT would function in a forward active zone with voltages of V_C=V_{DD}=14 V, V_B=1.3 V, with VE being lower than V_B. According to the datasheet, the transistor's threshold value (V_{th}), which is 4 V, was smaller compared to the transistor's gate voltage (V_G), which, as was previously established, functioned as a switch when the Arduino's digital terminal D2 displayed a logic low condition. The MOSFET was operating in the OFF state at this time, preventing any current from passing down the drain branch. The V_G>Vth requirement was met when D2 produced a logic high status, causing the transistor to flip to the ON state. More specifically, the MOSFET in the ON position always functioned in the resistive region as the V_{DS} value never exceeded V_G-Vth while the system was in operation. As the potentiometer's resistance climbed, V_{OUT} likewise did so until the voltage over the pump was high enough to turn on the DC motor and keep the pump's minimum flow rate constant. According to the LTSpice computations in Section 3.1, a current on in the range

of tens of milliamperes passed through the branch while the MOSFET was in the ON state.

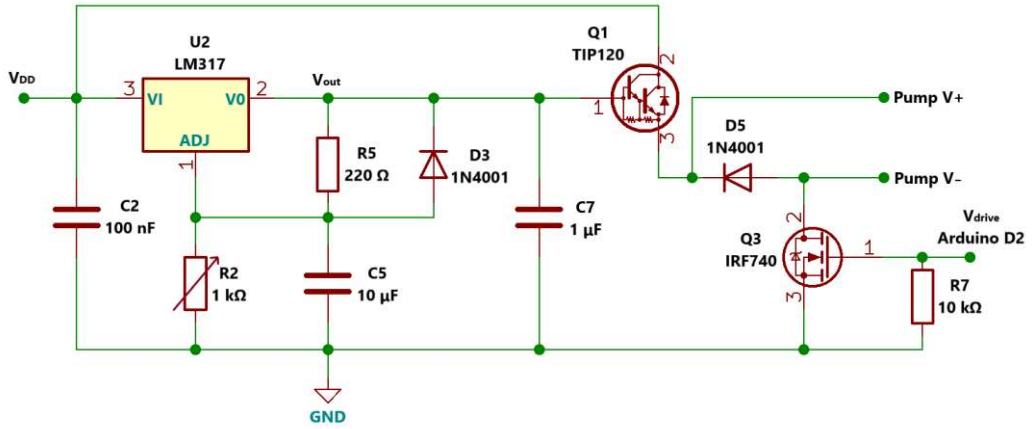

Figure 20 Pump power supply circuit developed using an LM317 linear voltage regulator and a network of passive and active components. The circuit is controlled by the Arduino board through the transistor Q3.

3.1.5 Solenoid Valve Power Supply

The solenoid valve network in Figure 21 is constructed similarly to the pump power source, with a few minor variations. Compared to the pump, the solenoid valve exhibits a higher DC impedance (137 Ω versus 10.3 Ω). As a result, a greater V_{OUT} value was required to provide an adequate voltage drop over the solenoid valve (V_{SV}) to enable the passage of the minimal current necessary to open the orifice. This meant that a larger resistance was required because the 1 kΩ potentiometer was no more adequate to do the assignment. In order to ensure that the resistor value range could be adjusted from a minimum of 1 kΩ to a maximum of 2 kΩ and the precision of the 10-turn potentiometer was able to remain in the appropriate resistance range, a 1 kΩ resistor was inserted in series with the potentiometer. As seen in the simulation graphic in Figure 22, this allowed fine regulation of the solenoid valve current, which translated into exact control of the valve opening. The V_{OUT} span could therefore vary from an initial value of 7.23 V to an ultimate value of 12.46 V.

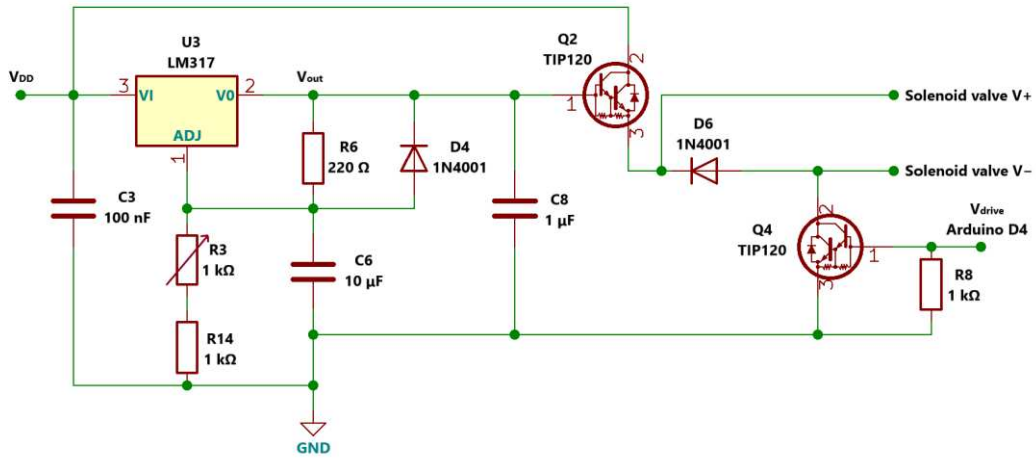

Figure 21 Solenoid valve power supply circuit developed using an LM317 linear voltage regulator and a network of passive and active components. The circuit is controlled by the Arduino board through the transistor Q4.

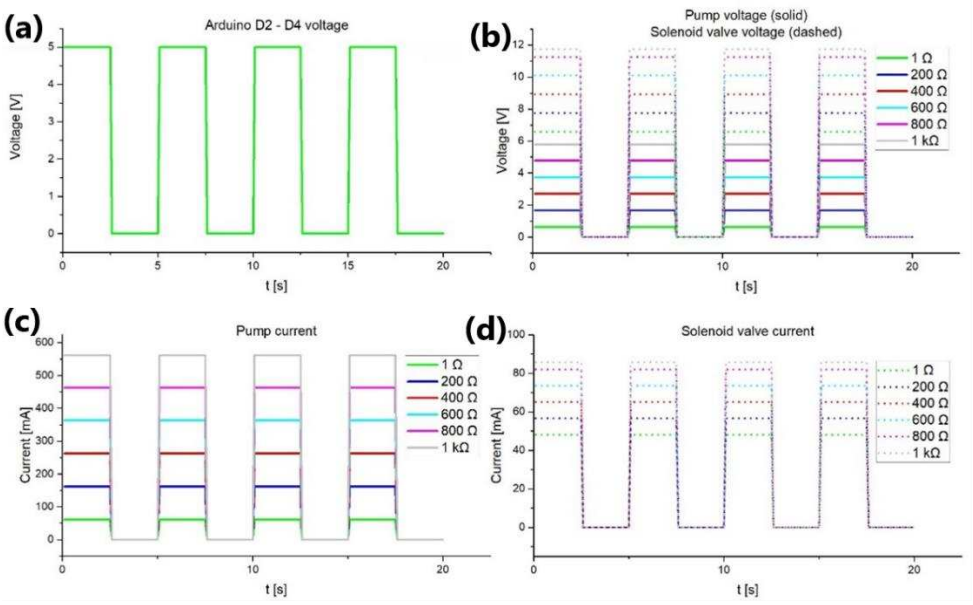

Figure 22 Results of the LTSpice simulations performed. **a)** Voltage on the D2-D4 terminals provided by the Arduino board. **b)** Pump and solenoid valve voltages as a function of the resistance set on the potentiometer. **c)-d)** Current flowing inside the Pump and the solenoid valve as a function of the potentiometer resistance.

3.1.6 PCB board development

Figure 23a illustrates how the circuit elements were organized on an electronic circuit board employing open source software (ECAD) (KiCad v5.1.6). The

voltage regulator's maximum current rating is 2.2 A, as stated on the data sheet, which is significantly less than the maximum current ratings of the pump and solenoid valve, that are less than 600 mA. As previously mentioned, the current range for the electronic system was widened through the use of BJT and MOSFET transistors with maximum current ratings of 5 A and 5.6 A, respectively. This decision was taken in order to allow the system to work with pumps that have greater power, greater flow rates, and maximal differential pressure. In order to meet a constant load current of 3.5 A during an ideal maximum rise in temperature of 20 °C and 5 A at a rise in temperature of 50 °C, which was suitable for the intended use in both cases, the width and thickness of the copper traces on the PCB were determined to be 1 mm and 0.89 mm, respectively. There was more room for the nominal power of the trace since the circuit was set up to switch among the pump and solenoid valve. To further lower the temperature increase of these parts during operation, a heat sink filled with a thermal paste was attached to every power transistor in the circuit. As illustrated in Figure 23b, the components were put in a small plastic box and attached to the PCB using a hot air soldering station (Hot Air Soldering Station 124-4134, RS PRO). A two-position switch placed on the front of the box is used to turn the system on. Figure 24 displays the system in its completed state.

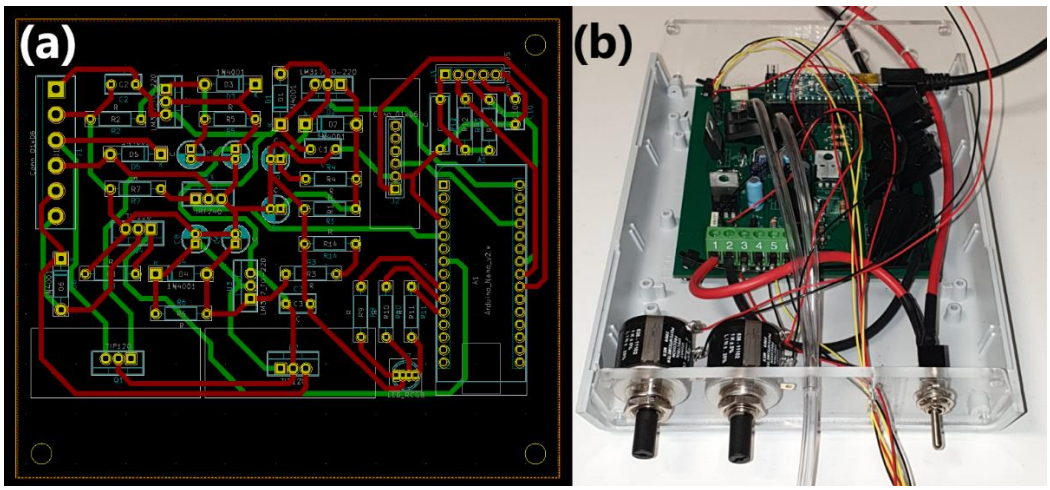

Figure 23 a) PCB board layout designed with KiCad. **b)** PCB board assembled and mounted inside a plastic enclosure.

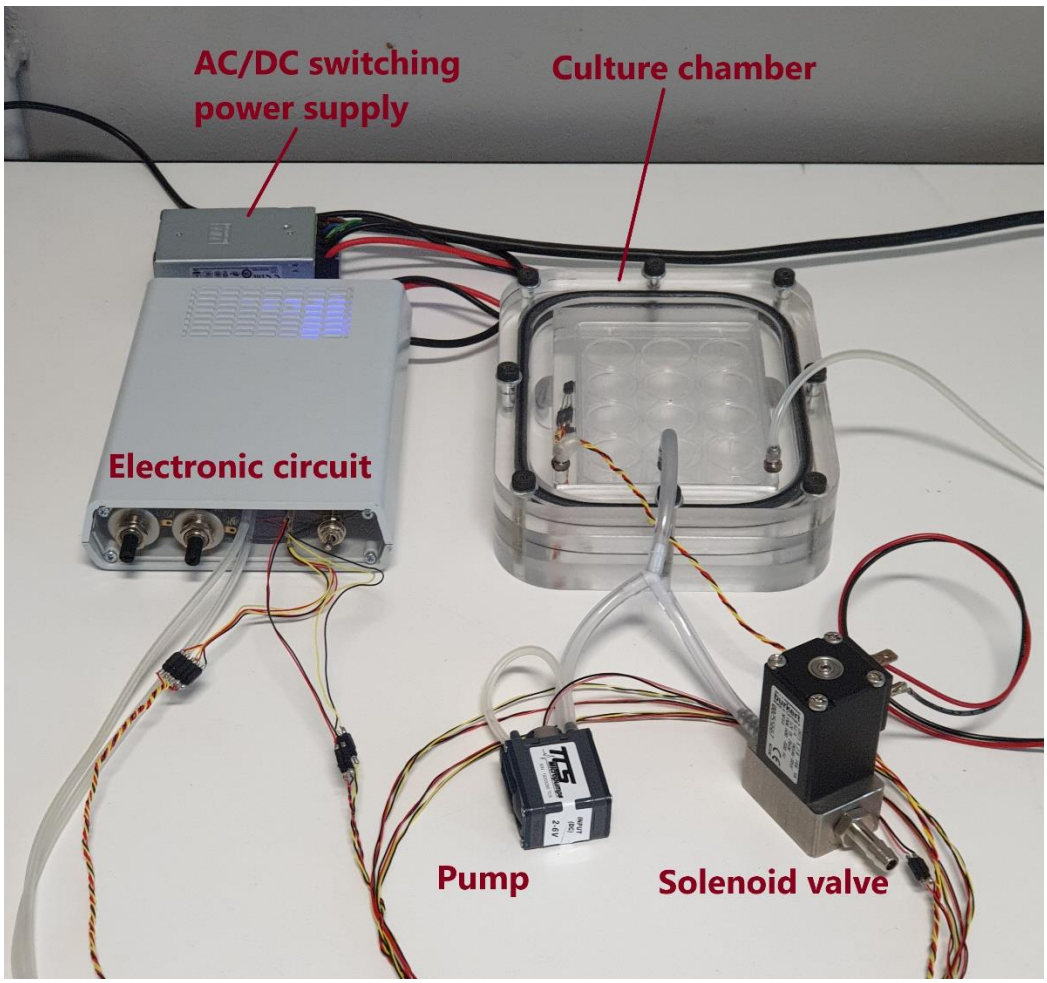

Figure 24 Final appearance of the system mounted with all its main parts.

3.1.7 Arduino Sketch

The solenoid valve and pump may be freely programmed on the Arduino board to run for the specified period. The loop function carried out by the microcontroller is displayed in the summarized Arduino program in the process diagram in Figure 25. Two time periods, *timer_P* and *timer_ SV* along with a common time variable *t* were established in the program setup for the pumping duration and the solenoid valve operating time. To guarantee that the Arduino board can read the output variables from these sensors, both temperature gauge and pressure gauge libraries have been added to the application. The solenoid valve was operating in the OFF state and the pump remained in the ON state at the start of the loop function. The parameter t was set to zero at RGB LED and the condition producing a red-light output was highlighted. Continuously monitoring the length of this cycle, the

parameter *t* was raised unless it reached the *timer_P* value. Following that, the microcontroller acquired the analog signal from the pressure sensor, transformed it to a form that could be read on the Arduino Serial Monitor, and also acquired the I2C signal from the temperature gauge and output it to the Arduino Serial Monitor. The solenoid valve was subsequently switched to the ON position, and the pump went into the OFF position. The variable t was reset to zero, and the RGB LED now produced blue light. As previously, once the variable t hit the value specified in timer_ SV, the length of this loop's duration was continually verified. At that moment, the loop function was repeated. The supporting information contains the full code highlighted.

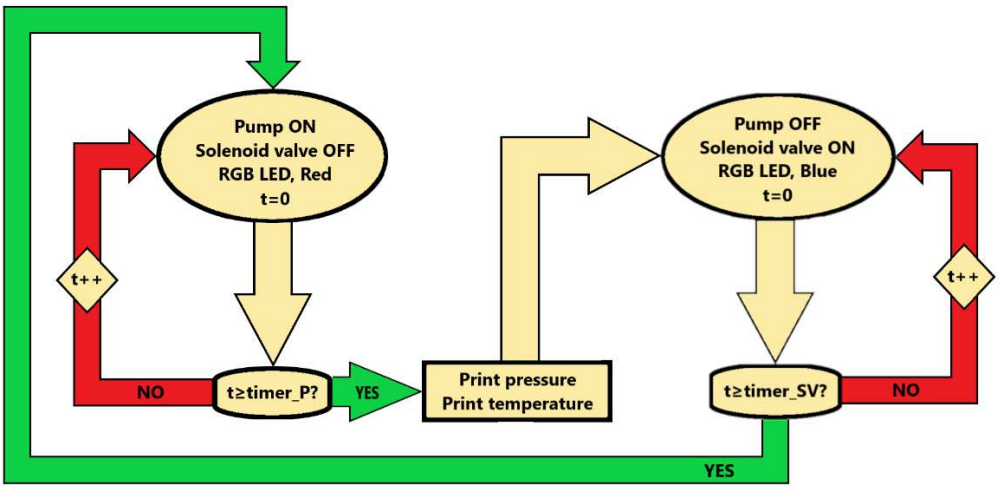

Figure 25 Flow chart of the firmware developed and uploaded on the Arduino board.

3.3 Results

3.3.1 Simulations

LTSpice (Analog Devices, Wilmington, MA, USA) was used to simulate each power supply circuit in order to show how the output of the voltage regulator is dependent on the resistance at the circuit's setting branch. The simulation's findings are displayed in Table 1, where the voltage regulator V_{OUT} is displayed for five distinct configurations of the simulated circuits resistance in the range between 1 and 1 kΩ. The choice of a fixed 1 kΩ resistor for the regulating branch of this main block was confirmed in the particular case of the Arduino power supply since the latter resistor value produced an output voltage of 7.2 V, which was inside the input voltage allowed by the Arduino. The solenoid valve

supply presented a greater output voltage, ranging from 7.2 to 12.5 V, with an additional 1 k resistor connected in series in the potentiometer branch. The power supply network for the pump was identical to that of the Arduino, so the VOUT sweep was also identical, ranging from 1.3 to 7.2 V. Figure 22 illustrates how the solenoid valve and pump's voltage and current rely on the MOSFET gate voltage regulated by the Arduino. The related DC impedances for the components were modeled, and they are 10.3 Ω for the pump and 137 Ω for the solenoid valve. As previously noted, 1 kΩ was selected as the resistance through the accuracy potentiometer for both device circuits. According to the simulations, increasing the resistance increased the voltage over the two devices, causing the solenoid valve to open in proportion to the current passing through it and the pump to vary its flow rate proportionally from a minimum to its maximum.

Table 1 Overview of the data provided by the LTSpice simulations as a function of the potentiometer resistance.

ADJ Resistance	**V_{OUT}, Arduino Power Supply (R_1)**	**V_{OUT}, Pump Power Supply (R_2)**	**V_{OUT}, Valve Power Supply (R_3)**
1 Ω	1.3 V	1.3 V	7.2 V
200 Ω	2.49 V	2.49 V	8.4 V
400 Ω	3.7 V	3.7 V	9.6 V
600 Ω	4.7 V	4.7 V	10.8 V
800 Ω	6.1 V	6.1 V	12.0 V
1 kΩ	7.2 V	7.2 V	12.5 V

3.3.2 Culture chamber leakage

To assess the alteration in tightness caused by the penetration rate of the sealant PDMS inside the system, an early tightness test was carried out on the system

both with and without the usage of a temperature gauge feedthrough. Figure 26 graphs illustrate how the chamber was first linked to an external pump that could provide an upper differential pressure of roughly 30 kPa before being separated so that pressure measurements could be taken over time. In the first instance, seen in Figure 26a, a commercial cap was used in place of the temperature sensor feedthrough. Over time, the chamber had a reasonably modest leakage pattern. A linear fit of the curve revealed three distinct trends in the graph: a leakage rate of -7.2-10-2 Pa/s in the 30–18 kPa range, -2.2-10-2 Pa/s in the 6.6-4.6 kPa region, and -1.1-10-2Pa/s in the 1.5-0.5 kPa range. The temperature gauge feedthrough was attached in the second instance, as indicated in Figure 26b, and the level of leakage dramatically increased. The identical three main trends were highlighted in the figure, with a linear fit of the curve revealing a more pronounced leakage rate relative to the first configuration. These leakage rates were determined to be -6.8 Pa/s in the range of 30 kPa-18 kPa, -7.7-10-1 Pa/s in the range 6.6-4.6 kPa, and -8.2-10-2 Pa/s in the range 1.5-0.5 kPa. Table 2 contains a list of all leakage rates. The chamber leakage rate was therefore insignificant for the application when taking into account the running period of the system, which in our instance was designed to conduct pressure cycling with a pump time of 2.5 s and a discharge time of 2.5 s, achieving a chosen ultimate pressure in the range of tens of kPa.

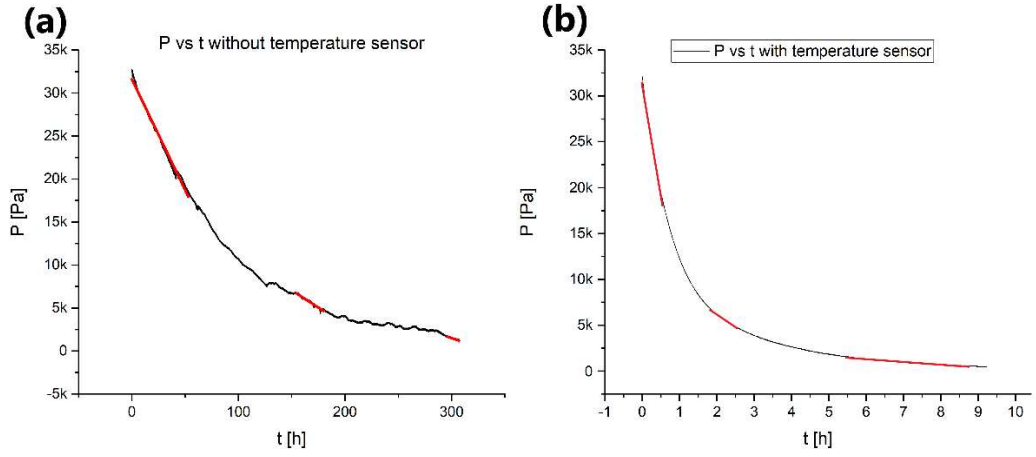

Figure 26 Leakage rate of the culture chamber, with **(a)** and without **(b)** temperature sensor feed-through mounted.

Table 2 Overview of the leakage rate of the culture chamber.

Pressure Range	Leakage Rate without T Sensor	Leakage Rate with T Sensor
30–18 kPa	$-7.2 \cdot 10^{-2}$ Pa/s	−6.8 Pa/s
6.6–4.6 kPa	$-2.2 \cdot 10^{-2}$ Pa/s	$-7.7 \cdot 10^{-1}$ Pa/s
1.5–0.5 kPa	$-1.1 \cdot 10^{-2}$ Pa/s	$-8.2 \cdot 10^{-2}$ Pa/s

3.3.3 Stability of the pressure profiles

Two configurations were used to verify the uniformity of the ultimate differential pressure attained in the chamber each cycle. The pump was set up in overpressure mode in the first setup, which caused the chamber's pressure to rise to 10.7 kPa. Figure 27a graph illustrates the findings, which demonstrate a steady trend over time with a standard deviation of $\sigma = 94.1$ Pa and a maximum variance in absolute pressure of 310 Pa. In the second instance, the pump was set up in vacuum mode, which reduced the chamber's differential pressure. The outcome is illustrated in Figure 27b and exhibits a steady trend with a highest absolute pressure fluctuation of 410 Pa and a standard variation of the greatest pressure fluctuation of $\sigma = 93.5$ Pa.

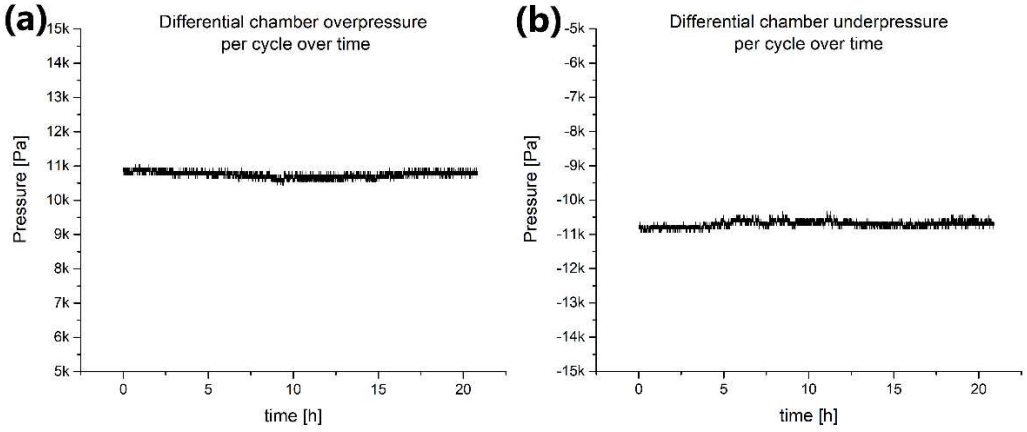

Figure 27 Pressure profiles of the system working in overpressure **(a)** and underpressure **(b)** mode.

The Arduino sketch's map function could detect fluctuations of 5 V/1024 bits, or 4.88 mV, on the analog pins since the analog to digital converter (ADC) located on the Arduino board has a resolution of 10 bits. The sensitivity of the pressure sensor was 4.5 mV/Pa as well. Consequently, it was anticipated that the chamber pressure information read from the Arduino would fluctuate by 100 Pa. Due to changes in the atmospheric pressure throughout the day, long-term observations may experience extra pressure fluctuations, which might result in an additional 100 Pa shift [235].

3.3.4 Temperature profile

The temperature of the culture chamber must be stable enough to support the development of a cell culture, which typically takes place in an incubator filled with CO_2 with a maintained temperature of 37 °C. In order to identify any temperature fluctuations brought on by the pressure cycles themselves as well as the heating of the pump and solenoid valve throughout operation, temperature stability tests were carried out on the system. A second similar temperature sensor was placed in the environment to monitor the temperature within and outside the chamber after the system was installed for use in a CO_2 incubator (ThermoFisher Scientific, Waltham, MA, USA, Heracell® 150i).

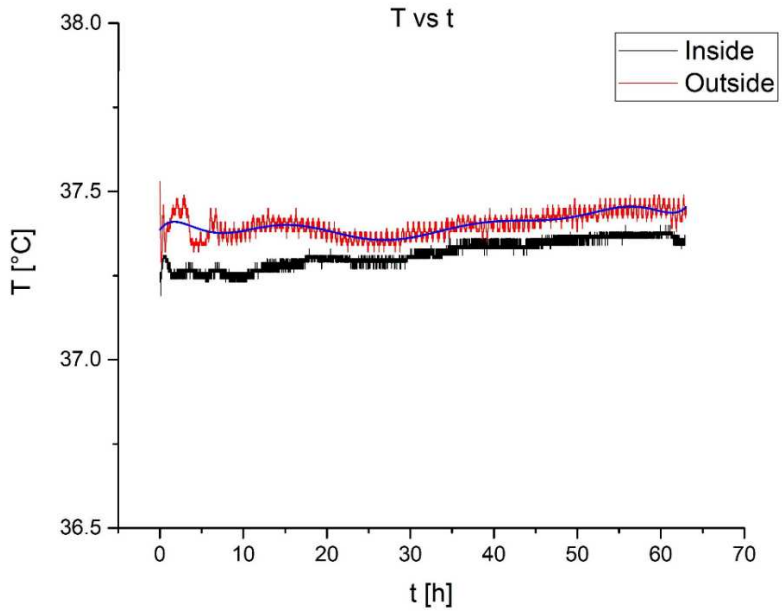

Figure 28 Temperature trend inside (black curve) and outside (red curve) the culture chamber, as a function of time.

The resultant temperature profiles, which are emphasized in Figure 28, demonstrate that the measured temperature within the chamber has an average temperature of 37.3 °C, a standard deviation of σ = 2.6-10-2 °C, and a highest absolute temperature change of 7.0-10-2 °C. The fact that the measured temperature outside the chamber had an average of 37.4 °C, a standard deviation of σ = 3.4-10-2 °C, and a highest absolute temperature shift of 0.1 °C suggests that neither the system's operation nor the pressure loops significantly changed the temperature inside the chamber. This claim is further supported by the fact that the highest absolute temperature change and the standard deviation were both much less than the temperature sensor's accuracy (0.5 °C).

Chapter 4

A programmable culture platform for stimulation and in situ pH sensing of lung cancer cells with organic electrochemical transistors

4.1 Introduction

One of the biggest factors causing death in developed nations is lung cancer [236]. Expensive and time-consuming animal trials must be replaced with more productive experimental techniques that go beyond conventional cultivation of cells in multi-well plates in order to develop cancer treatments. In order to retain differentiation of cells and tissue-specific function, new research fields have evolved during the past two decades that are moving toward dynamic models that replicate the organ-specific microenvironment. Despite the creation of several complex systems which attempt to replicate the circumstances that take place within human organs, including the stress events that the endothelial cells surrounding human alveoli and the epithelial cells in human alveoli experience, [237], [238], as well as a variety of human organs such as kidney[239], liver [240], intestine [85], and brain [241], There are not many flexible platforms that are suitable for use with conventional cell culture techniques. Furthermore, the

development of cultures in such devices prevents the use of conventional detection techniques frequently employed in biology labs, such as the measurement of absorbance in multi-well plates. In order to comprehend the fundamental concepts of typical lung organogenesis, in situ monitoring is also required to track crucial chemical, biological, and physical processes during dynamic cell growth, such as miRNA transport to nearby cells [242] or precise in vitro tracking of early/late apoptosis and necrosis of cells [243] as well as physical variables such as pH and O_2 content, NO and glucose [244]–[247]. The glycolytic metabolism of cancer cells, lack of oxygen and poor perfusion all contribute to the tumor microenvironment's usual acidic environment. Under physiological circumstances, a healthy tissue's pH is around 7.4, but in sick tissues, the pH level may vary from 5.5 to 7.0 [248]–[251]. Moreover, the medium's acidity affects the cell's life cycle, gene regulation, and metabolic processes in cells, making in situ pH monitoring a useful tool for the growth of cell cultures [252], [253]. The monitoring of pH is also very important in the study and development of exotic nanomaterials, such as gold nanoparticles [254], [255]. Given their small size and distinctive characteristics, nanoparticles are currently on the cutting edge of technological and medical advancement. Delivery of drugs to target cells, cancer prevention and therapy, are some of the medical fields where clinical applications of nanoparticles have been established [256], [257]. Due to their simplicity in manufacture, chemical stability, distinctive optical features, and biocompatibility, such technology has drawn tremendous scientific attention [258]. Applications such as optical tomography imaging and the use of tracers to identify DNA, can be developed thanks to these distinctive particles with reduced size, comparable with cells [259], [260]. Additionally, because of their distinct plasmon characteristics, they have the potential to create artificial tissues for use in ophthalmic therapeutic applications. Studying their dispersity in dimensions, form, and distribution, is also very important. The particles shape, dimension, and surface-charge features are controlled by a variety of processes and synthesis techniques. Due to its great precision and control over particle size, the process of synthesis employing citrate reduction is one of the most extensively employed among the variety of advanced methods [261]. It has been observed a significant variation in the reaction yield by about 46% moving from pH 5.3 to pH 4.7 on the concentration of the gold colloidal suspension synthesized under standard conditions, thus highlighting the great importance of pH in this field [262]. Citrate ions have an essential function in stabilizing the produced nanoparticles by limiting particle development and aggregation through electrostatic repulsion and acting as a reductant, turning gold ions into gold atoms. As a consequence, at

elevated citrate concentrations, this ion covers and stabilizes smaller particles, but at low concentrations, inadequate coverage allows particle development to proceed, resulting in the creation of particles with greater particle sizes [263]. Citrate also plays the function of a pH mediator in reaction mixtures, which it does by having a significant impact on the dimension and thus internalization of the resulting particles [264]. Systems for real-time pH monitoring, including OECTs, namely organic electrochemical transistors, two-photon fluorescence systems, and microneedles, have been developed as a result of research on pH monitoring in cell cultures [265]–[267], They are the most researched modern biosensing sensors that offer benefits like excellent sensitivity, great stability, and cheap cost [268]. The active component of an OECT is a conductive polymer, typically poly(3,4-ethylenedioxythiophene): polystyrenesulfonate (PEDOT:PSS), a type of semiconductor where the channel current (I_{DS}) may be controlled by introducing cations from an electrolytic solution into which the device is immersed, applying a positive gate voltage (V_G), and allowing it to operate easily in cell culture medium [269]. This type of systems has undergone extensive research for use in biological systems, including biosensing of target chemicals of interest when the gate electrode is properly functionalized, studies of cell migration and permeability of membranes, ion communication, and in vivo measurement of activity in neurons [270]–[272]. The research outlined in this dissertation aims to create a platform for the development of both regular and tumorous lung cells that is compatible with common multi-well plate culture procedures. In these techniques, cells are exposed to mechanical stimulation provided by a periodic rise in the hydrostatic pressure within the culture chamber, simulating a natural respiratory cycle. On the other hand, a rise in hydrostatic pressure raises the partial pressure of gases in the culture chamber, especially CO_2, which can cause the creation of carbonic acid and a reduction of the pH of the culture medium once it has dissolved in the cell culture fluid [273], [274]. In order to keep track of pH fluctuations in the medium used for culture during the growth of cells and to research the dynamics of this variable while either normal and tumor cell lines are exposed to a hydrostatic stimulus, the system is also equipped with a number of PEDOT:PSS-based OECTs that operate directly in the system.

4.2 Materials and Methods

4.2.1 Culture chamber fabrication

The cell culture chamber was manufactured employing a numerically controlled milling equipment (Benchman VMC 4000) and a 3D CAD program called Rhinoceros, developed by Robert McNeel & Associates. The chamber is made of three polymethyl methacrylate (PMMA) plates that were layered together and fastened with eight steel screws after being hollowed down to fit a multi-well plate with standard dimensions. A pair of nitrile-based O-rings that have been lubricated with vacuum grease and put in a groove between every pair of plates assure the chamber's tightness.

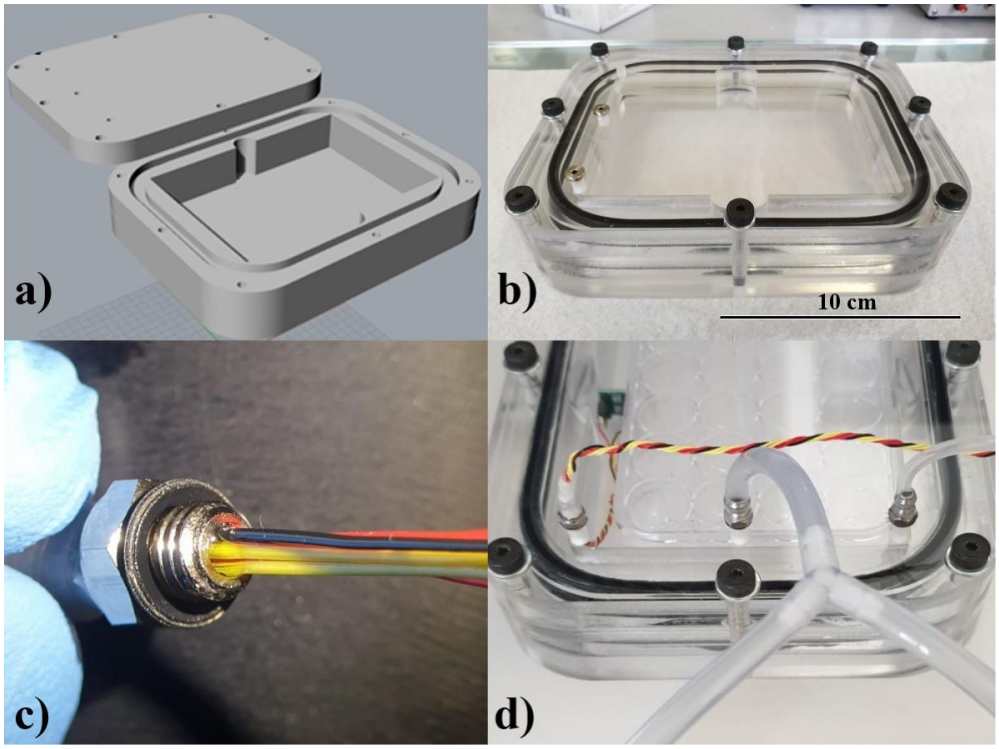

Figure 29 Overview of the PMMA culture chamber fabricated. **a)** CAD of the culture chamber. **b)** culture chamber assembled with its o-rings and closed with its set of screws. **c)** detail of the feed-through of the temperature sensor, sealed with PDMS. **d)** detail of the lid.

Three feedthrough apertures on the top portion of the plate allow for the connection of the temperature detector, differential pressure gauge, and chamber pressure apparatus. As illustrated in Figure 29, a pneumatic connection was used

to provide the feedthrough for the temperature gauge, and it was properly sealed with PDMS (Sylgard 184, ratio 1:10) to make the chamber airtight.

4.2.2 Electronic circuit

To program the platform and control the on/off periods of a diaphragm air pump and a solenoid valve and how long they operate, in order to achieve the desired pressure in the chamber, an embedded microcontroller (MCU) implemented with an Arduino Nano® microcontroller is used. This MCU also manages the data from the temperature gauge and the differential pressure gauge connected to the culture chamber. In section 3.2, the evolution of electronic systems is extensively covered.

4.2.3 OECTs development

On a 4" p-type (100) silicon wafer covered with SiO2, the OECTs were created in a clean room setting. The source and drain electrodes were designed with an interdigitated geometry in order to produce devices with substantially reduced dimensions as well as considerably boost the B/L ratio of the transistors, which in this particular instance were designed with W = 9.99 mm and L = 10 μm. This was done in consideration of their future application, which will involve immersing the devices in the small volumes of cell culture medium of a multiwell plate. The transistors' Au source and drain electrodes were made using lift-off and e-beam evaporation techniques. Following a well-known approach, an Al2O3 passivation coating was added on the transistors employing the identical method, maintaining a single opening on the conductive pads as well as one on the interdigitated source and drain electrodes [275]. Then, using a spin coating technique, a PEDOT:PSS coating 200 nm thick was applied, and it was patterned using photolithography and reactive ion etching. The supporting information includes a full description of the fabrication process. Last but not least, the chip and gate electrode are put together in a fluidic system, whereupon the devices become subjected to the electrolytic solution by being inserted into the inlet port (Fig. 30e). As indicated in Figure 30f, electrical characterization is carried out by making contact with the electrical terminals from outside the system.

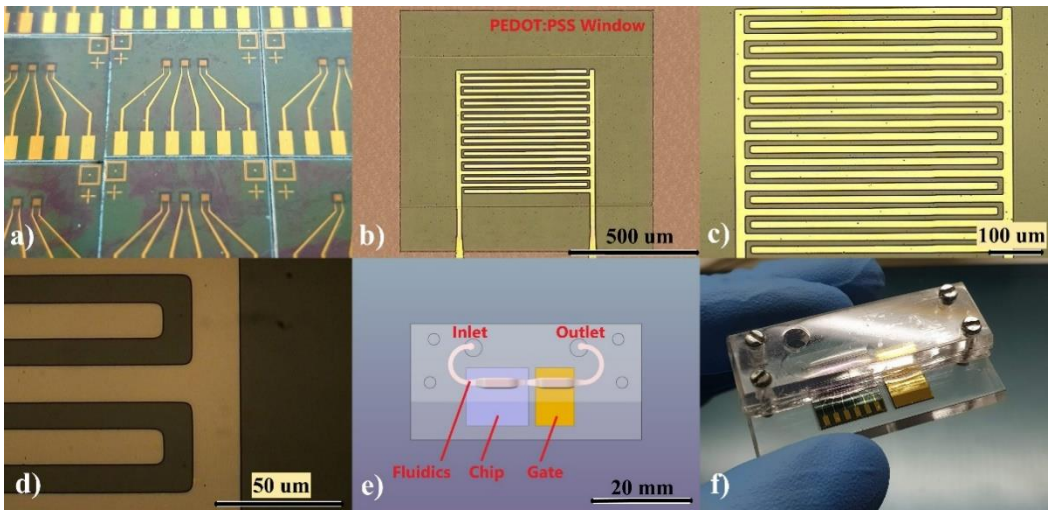

Figure 30 Overview of the OECTs developed. **a)** single chip with a triplet of devices fabricated on its surface. **b)-d)** detail of the geometry of source and drain electrodes. **e)-f)** CAD and picture of the fluidic chip.

4.2.4 Cell viability assay

For the purpose of evaluating cell survival, the human epidermal keratinocyte line (HaCaT) and the human foreskin fibroblast line (HFF-1) were chosen as two normal cell lines. In addition to 15% fetal bovine serum (Sigma-Aldrich), 1% L-glutamine, 1% penicillin-streptomycin, and 1% sodium pyruvate (Sigma-Aldrich), cells were grown in DMEM GLUTAMAX (Gibco, ThermoFisher Scientific). In a 96-well plate, 104 cells of HFF1 and 7000 cells of HaCaT were plated in each well, respectively. By using the MTT test (thiazolyl blue formazan, Sigma-Aldrich) to measure metabolic activity at 24 and 72 hours after seeding. Following a two-hour incubation with 0.5 mg/ml MTT at 37°C, the salts were then submerged in MTT solvent (10% SDS, 0.01 M HCl in H2O) for one hour. Using a SynergyTM HTX Multi-Mode Microplate Analyzer (BioTek, Winoosky, Vermont, USA), absorption was detected at 570 nm (650 nm reference wavelength).

4.3 Results

4.3.1 Culture chamber leakage

The airtightness of the chamber, the reliability of pressure periods over the course of time, and the tracking of variations in temperature generated by pressure increasing and decreasing phases in comparison to the outside chamber were all

tested using the culture chamber equipment and its electronics. In Section 3.3, the complete description of the characterizations carried out on the culture chamber is covered in depth.

4.3.2 HaCaT and HFF-1 proliferation tests

In the culture chamber, preliminary proliferation experiments were conducted with pressure cycles lasting 5 s and adjusted at 12 kPa. As a control, cells that had been cultivated in the usual manner were utilized. Using an extra-filled well as a reference, cultured human epidermal keratinocyte line (HaCaT) as well as human foreskin fibroblast line (HFF-1) were developed in duplicates (n=3). Cell proliferation was observed by measuring the optical density in both plates after 24 and 72 hours. By measuring the optical density in both plates, the rate of cell multiplication was kept track of.

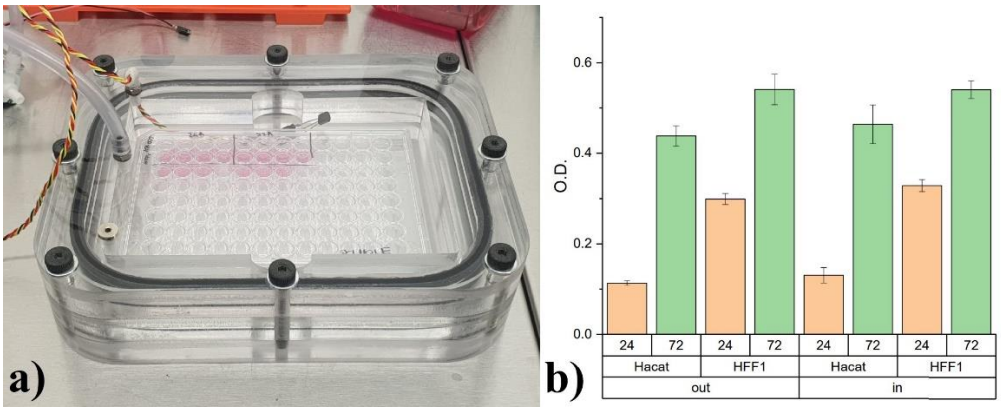

Figure 31 Overview of the multi-well plate inside the culture chamber **(a)** and proliferation results performed on HaCaT and HFF-1 cell lines inside and outside the culture chamber **(b)**.

It is important to note that there were no changes found when cells were subjected to pressure cycling, indicating that there is no impact on cell proliferation. Future research will examine different cell types as well as pressure levels to see if such variations in culture conditions affect how cells respond in terms of gene activation, proliferation, and viability.

4.3.3 OECTs characterization

The source, drain, and gate electrodes were connected to a programmed source meter (Keysight Technologies B2912A) for the purpose to characterize the transistors. The source voltage, that was linked to ground, served as the reference

for the gate and drain voltages. Cell culture medium was used as the source of electrolytes during tests on the devices using different gate materials. A porous Au gate electrode, an Ag/AgCl wire electrode, and an Au electrode evaporated by an electron beam were the three distinct gate electrodes employed. In each instance, the gate area that was subjected to the electrolyte mixture was 9 mm^2. The gate voltage was modulated between -0.75 and 1 V with a frequency of sampling of 125 mV/s, and the drain voltage was adjusted at -100 mV, in order to get the transfer curves. Figure 32 observations illustrate how the various gate materials behaved differently. When the gate voltage rises, the drain current of the transistor is efficiently reduced by both the porous Au gate as well as the Ag/AgCl gate, which turns the device off for V_G>0.8 V. When the evaporated Au gate is utilized, this does not occur, most likely because in this situation the capacitance of the channel-electrolyte barrier (C_{CH}) is significantly greater than that of the gate electrolyte one (C_G). The fact that porous Au gives an effective area twenty times higher than evaporated Au for the identical exposed gate region, resulting in a higher C_G, is evidence of this phenomenon. The devices' highest transconductances were 0.4, 5.0, and 5.2 mS, respectively, and the gate voltages that corresponded to those values were 0.9 V corresponding to the evaporated Au electrode, 0.49 V for the porous Au gate, and 0.51 V for the Ag/AgCl gate. Since Ag/AgCl gate electrodes have a better transconductance and reliability than the other two gate materials, stability studies were also carried out on these devices. To further confirm the functioning of the transistors in the context of cell growth environment, the electrolyte solution for this test was once more the cell culture medium. The drain potential was maintained at -100 mV, while the gate potential was varied within -0.75 and 1 V at a frequency of sampling of 125 mV/s. The various transfer curves were measured in the experiment depicted in Figure 32(c) with a 30-minute break in between. At the curve's greatest transconductance point (V_G=0.51 V), the devices displayed an overall current displacement over time of 158 A, or a relative current displacement of 7.3%. Table 3 provides an overview of the major performance indicators for each of the three gate electrodes.

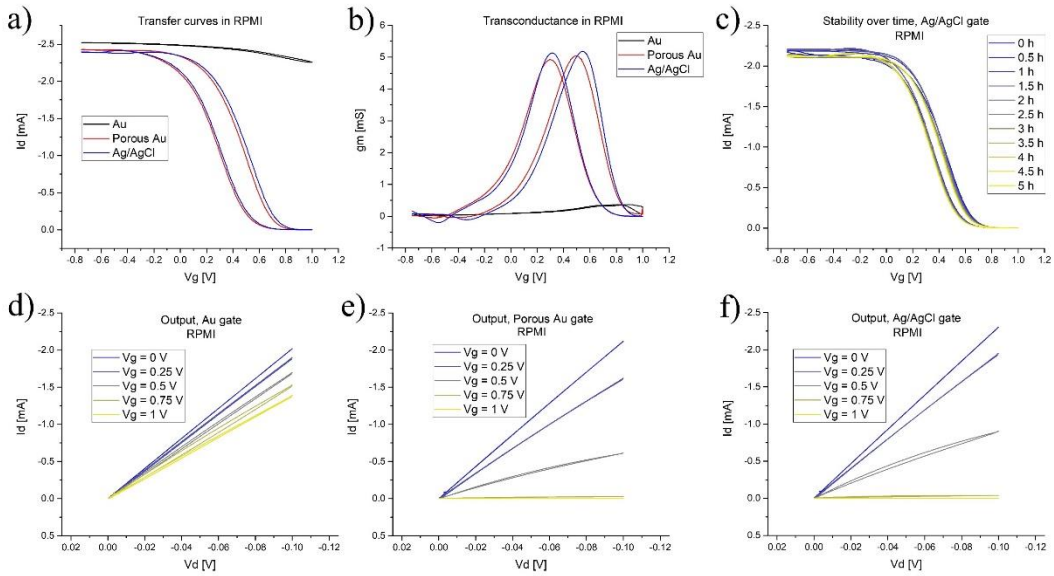

Figure 32 Transfer curve **(a)** and transconductance curve of the OECTs as a function of the gate electrode material. **c)** stability response of the device with an Ag/AgCl gate electrode as a function of time. **c)-f)** Output curves of the device as a function of the gate electrode material.

Table 3 Overview of the figures of merit of the OECTs.

Gate electrode	$\mathbf{g_{mMAX}}$	$\mathbf{V_{G\|gmMAX}}$	$\mathbf{I_{ON}/I_{OFF}}$	$\mathbf{\Delta V_G}$ **hysteresis** $\mathbf{@g_{mMAX}}$
Evaporated Au	0.4 mS	0.9 V	-	41 µV
Porous Au	5.0 mS	0.49 V	3001	195 mV
Ag/AgCl	5.2 mS	0.51 V	2738	230 mV

4.3.4 pH response of OECTs

Six distinct solutions having increasing amounts of HCl that ranged from 0.1 M (pH 1) to 10-6 M (pH 6) and a predetermined amount of NaCl (0.1 M) were used to study the electrical behavior of the transistors within electrolyte solutions with varied pH values. The Ag/AgCl gate electrode was used in all experiments, with

V_G varying from -0.75 to 1 V, V_D equal to -100 mV, and a scan rate of 125 mV/s. As the pH of the solution lowers, the data shown in Figures 33a and 33b clearly demonstrate a change in the transfer profiles (and consequently, the gm_{MAX}) for smaller V_G values. Table 4 displays the primary performance information for the transistors under these circumstances. The variation in the transfer profiles, whose is clearly defined by the exact position of the transconductance peak ($V_{G|gmMAX}$), may be used to monitor how the device responds to changes in pH. Table 4 shows that as the pH is decreased, the peak location moves to lower gate voltages. This behavior was anticipated since the internal amount of dissolved H+ ions rise over an order of magnitude for each unit pH as the pH drops.

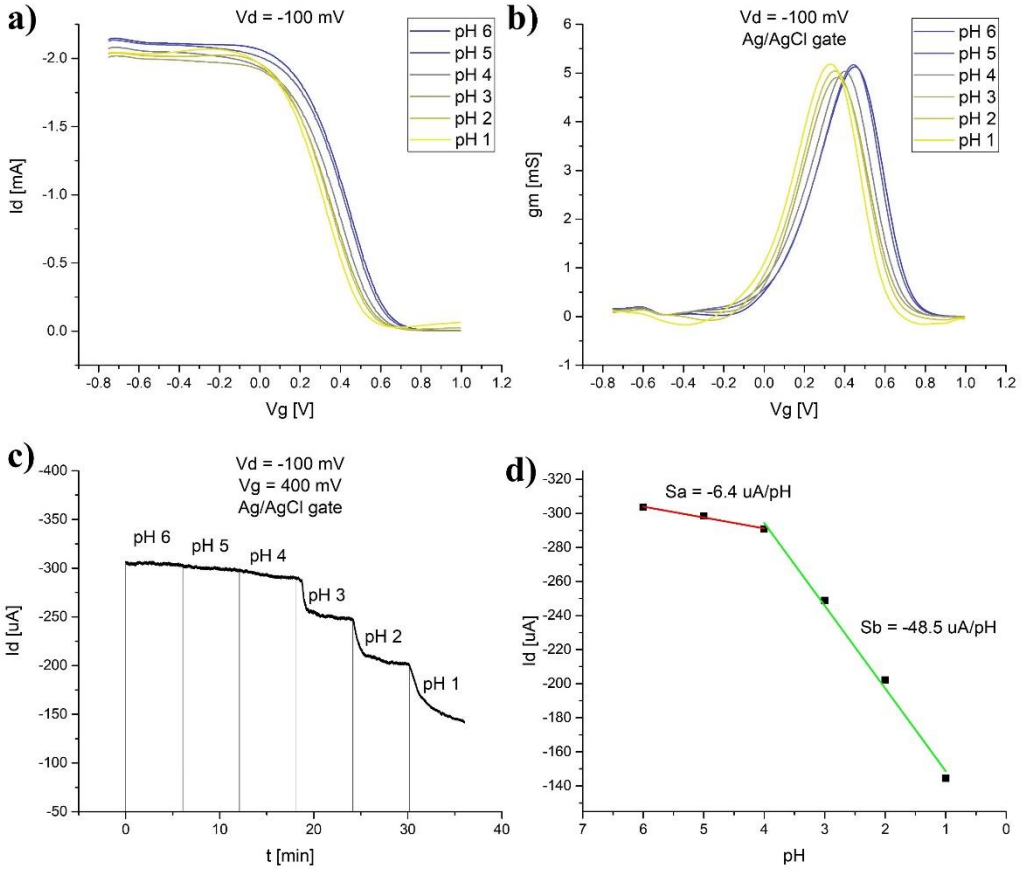

Figure 33 Response of the transfer curve **(a)** and the transconductance curve **(b)** of the OECTs as a function of the acidity of the electrolyte solution, using an Ag/AgCl gate electrode. Real-time output curve of the device working at its operating point, as a function of the acidity of the electrolyte solution fluxed inside the device fluidics **(c)**. Resulting sensitivity calculated as a function of the pH **(d)**.

Further positive ions were thus injected into the polymer film from the electrolyte at a given V_G, increasing the polymer film's capacity to stop the drain current. In a real-time assessment, V_G=400 mV and V_D=-100 mV were chosen, and the least acidic solution (pH 6) and the most acidic solution (pH 1) were sequentially flooded for 360 s at a fluidic flow rate of 100 l/min. Figure 33c depicts the results, which demonstrate that the drain current for the last three solutions (second group, pH=3, 2, 1) decreased significantly whereas the drain current for the initial three solutions (first group, pH = 6, 5, 4) slightly decreased.

Table 4 Main figures of merit of the OECTs as a function of the acidity of the electrolyte solution.

pH	gm_{MAX}	$V_{G\|gmMAX}$	I_{ON}/I_{OFF}	ΔV_G shift pH 6 @gm_{MAX}
6	5.1 mS	0.45 V	474	-
5	5.2 mS	0.44 V	854	10 mV
4	5.0 mS	0.40 V	773	50 mV
3	4.9 mS	0.36 V	669	90 mV
2	5.0 mS	0.35 V	135	100 mV
1	5.2 mS	0.33 V	103	120 mV

4.3.5 Absorbance tests on culture media

An absorbance interference study was carried out in order to show whether the presence of the OECTs did not affect the pH of the cell culture medium. A shift in the absorbance spectrum in the cell culture medium indicates a change in pH since the medium includes phenol red as a marker of pH, which transforms from yellow to a light pink throughout the pH range between 6.8 and 8.2. A preliminary absorbance alteration assay in cell culture media (RPMI 1640, GlutaMAXTM, Gibco ThermoFisher Scientific) was carried out by dipping the chips (non-biased) within the medium in three replicates and recording the absorbance of the cell culture medium in the wavelength range between 300 and 800 nm every 24 hours

(Figure 34a). This was done in consideration of the pH tracking application to which the OECTs in this work are intended. After removing from their spectra the components of the multiwell plate's own material, which served as a reference, the absorbance was evaluated with three replicates of the exact same culture medium. Figure 34b shows a consistent peak of absorption with a wavelength of 559 nm and no differences in absorption among wells over the course of 7 days. This might be as a result of the culture medium pH appearing to remain constant or changing in a way that this monitoring method is unable to detect.

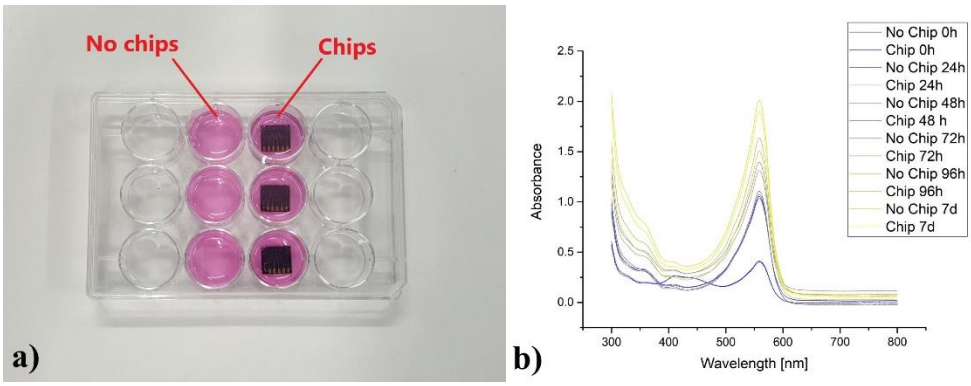

Figure 34 Overview of the absorbance test performed on the culture media with and without OECTs inside it **(a)** and resulting absorbance spectrum as a function of time **(b)**.

Chapter 5

Tuning of OECTs performance

5.1 Introduction

In this chapter, we focus on the pathway taken to enhance the performance of OECTs when employing an Au gate electrode. Our objective is to create a more sensitive and versatile device, broadening its potential applications beyond monitoring pH values in the culture medium. We aim to explore the possibilities of utilizing these devices in the field of biosensing. Initially, we present the preliminary biosensing tests conducted using the same devices discussed in Chapter 4, employing a biofunctionalized gate electrode. Subsequently, we emphasize the efforts invested in optimizing a novel category of devices, in which the Au gate electrode performance is improved. These new devices encompass improvements in channel geometry, as well as the design of source, drain, and gate electrodes to enhance the amplification of drain current at zero gate voltage. The performance of such devices are then highlighted and preliminary tests performed in acidic solutions have been carried out, showing the device response as the pH of the solution decreases.

5.2 Biosensing tests

Preliminary biosensing tests have been carried out employing the devices described in chapter 4, with a functionalized Au gate electrode. The functionalized protocol consists in the growth of a self-assembled pattern of thiols on the gate surface, working as functional groups which are able to chemically

interact with a target molecule, which consisted in bovine serum albumin (BSA), thus modifying the potential of the gate electrode and translating this variation into a modulation of the drain current. The functionalization protocol, as well as the testing protocol, is widely discussed in a previous publication of our research group [275], and it consists on the recording of the transfer curves of the devices employing two different gold gate electrodes, of which one is functionalized, while the second works as a blank. A solution containing BSA with concentrations ranging between 1 pM and 1 nM are managed to interact with the functionalized gate electrode, while the second gate works with a PBS solution. The results, highlighted in Figure 35, shows an uncertain behavior of the device as a function of the concentration of the BSA concentration, both when employing an Au gate electrode, or a functionalized one. The devices shows a behavior not related on the increasing concentration of the analyte, thus making unclear whether the variations in the transfer curves are affected by this parameter or by external factors, such as the intrinsic relative instability range highlighted in the stability tests showed in the previous chapter, or by the degradation of the polymer by electrolyte flux occurring through the microfluidic channel surrounding it, and needs to be further investigated. Moreover, the very low transconductance of the device when utilized with an evaporated Au electrode, makes very difficult the investigation of such effects with a functionalized Au gate electrode.

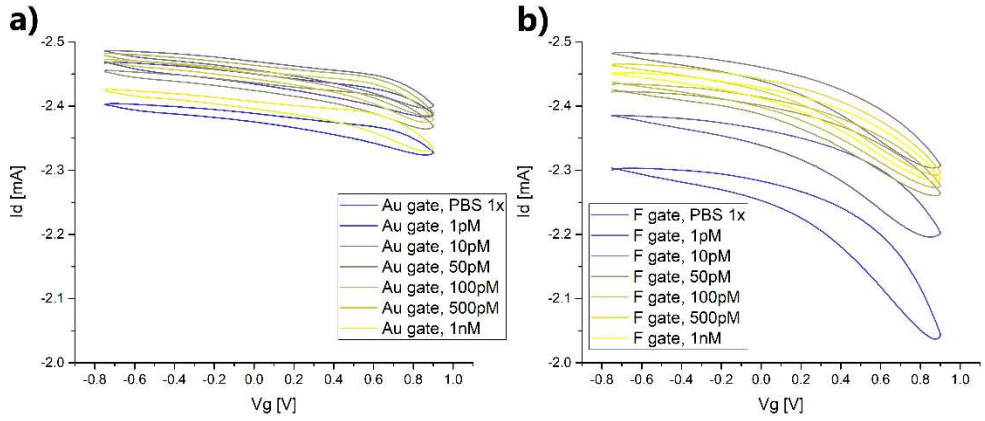

Figure 35 Transfer curve of the Au gate electrode as a function of the BSA concentration **(a)** and transfer curves of the same devices when using a functionalized Au gate electrode **(b)**.

5.2 Geometry variation

The results showed in the previous section, as well as the low performances of the evaporated Au gate electrode shown in the previous chapter, highlighted the necessity to modify the geometry of the gate electrode in order to increase the surface area exposed to the electrolyte solution, and thus the associated gate capacitance. Moreover, the gate voltage at which the transconductance shown its peak must be reduced from the value of 0.9 V highlighted in the previous chapter for the evaporated Au, towards values closer to 0 V. As highlighted in Figure 36, a new geometry for the device has been designed, in which the gate electrode is now fabricated directly into the surface of the device, a solution different from the previous ones, in which the gate electrode was separated from the chip. This new geometry exhibits a gate surface area exposed to the electrolyte solution of 23.36 mm^2, a value 2.6 times greater than in the previous device. In the zoom highlighted in Figure 36a, is shown the detail of the new channel, which exhibits a geometry with a W/L ratio of 80, a value 12.5 times smaller than the previous one, which turned out to be 999, keeping at the same time the previous channel thickness of 80 nm.

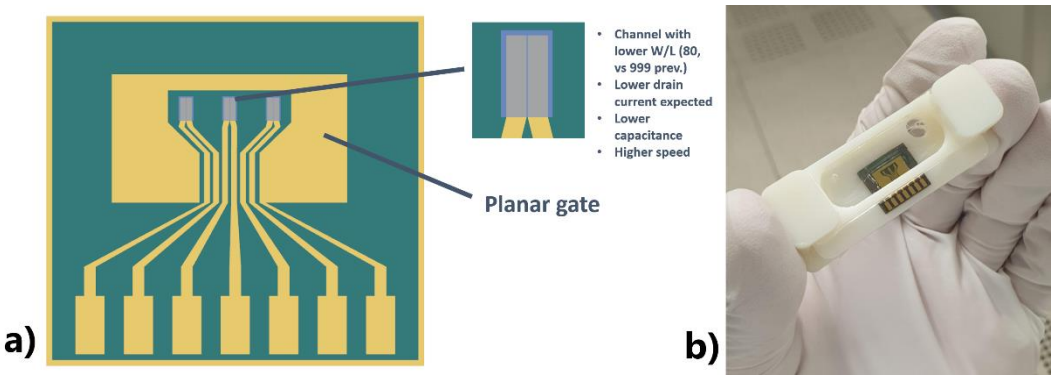

Figure 36 New device geometry **(a)** with the detail of the channel geometry, and device assembled in the microfluidic case **(b)**.

In this scenario, according to the equation for the calculation of I_D discussed in Chapter 2, the device must exhibit a reduced drain current compared with the previous one, with a peak transconductance in correspondence of a lower gate bias, as confirmed by the transfer and transconductance curves shown in Figure 37 [164]. All the tests have been carried out in RPMI culture media. The figure illustrates a drastic reduction of the drain current compared to the previous devices where an evaporated Au gate was used, showing a drain current at zero gate voltage of 0.21 mA, a value 12 times lower than the previous drain current in

the same conditions, which turned out to be 2.55 mA. Moreover, also the peak transconductance shows a clear reduction towards smaller gate voltages. Comparing again the peak transconductance at the same conditions of the previous device, the new geometry exhibits a value of g_m=0.4 mS with V_d=0.7 V, compared to the previous results of g_m=0.4 V with V_d=0.9 V. In table 5 are summarized the main figures of merit of the new device.

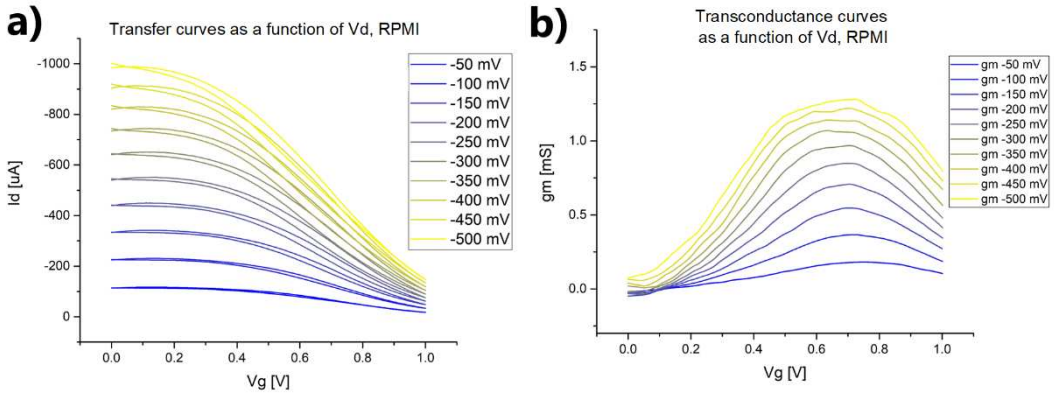

Figure 37 Transfer curve **(a)** and transconductance curve **(b)** of the new devices as a function of the drain voltage.

Table 5 Main figures of merit of the new OECTs as a function of the drain voltage

Vd	gm_{MAX}	$V_{G\|gmMAX}$	I_{ON}/I_{OFF}
-500 mV	1.3 mS	0.64 V	6.60
-450 mV	1.2 mS	0.65 V	6.37
-400 mV	1.2 mS	0.65 V	6.88
-350 mV	1.1 mS	0.65 V	7.09
-300 mV	1.0 mS	0.66 V	7.16
-250 mV	0.9 mS	0.68 V	7.26

-200 mV	0.3 mS	0.68 V	7.00
-150 mV	0.6 mS	0.69 V	6.7
-100 mV	0.4 mS	0.71 V	6.57
-50 mV	0.2 mS	0.73 V	5.75

5.3 Porous gold electrodeposition

Despite the improvements of the device, resulting in lower current and lower peak transconductance gate voltages, the g_m of the transistor remains very low, making it difficult to employ as a functionalized biosensor. Given also the low I_{ON}/I_{OFF} figure of merit of the new devices, an enhancement of the surface area exposed to the electrolyte solution is needed, in order to increase the capacitance associated to the gate-electrolyte interface C_G, in order to make it dominate over the channel-electrolyte one C_{CH}. An electrodeposition of porous gold has been grown on the planar gate electrode following the procedure highlighted in a previous work of our research group [276], aiming to amplify the equivalent surface area exposed to the electrolyte solution. The result, highlighted in Figure 38, shows the resulting gate electrode with a layer of porous gold grown on its surface.

Figure 38 Transfer curve **(a)** and transconductance curve **(b)** of the new devices with electrodeposited porous gold on the gate surface, as a function of the drain voltage.

The resulting transfer curve and transconductance curve of the device have been obtained in the same manner as in the previous discussed cases, with V_d=-100 mV, employing the cell culture medium as electrolyte solution. The results, illustrated in Figure 39, shows a sharp increase in the figure of merit I_{ON}/I_{OFF}, which turns out to be 46.96 (compared to 6.57 in the previous case), probably due to the increase capacitance associated with the gate-electrolyte interface, maintaining at the same time a drain current value at zero gate voltage comparable with the previous case. Also the transconductance of the device results inevitably increased, reaching a maximum of 0.6 mS (compared to the 0.4 mS of the previous case), this time with a peak shifted at even lower gate voltages, namely 0.56 V.

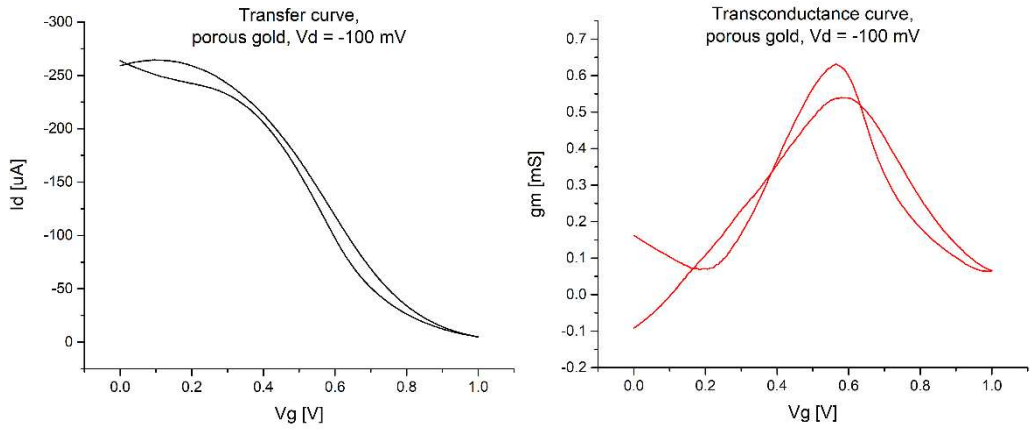

Figure 39 Transfer curve **(a)** and transconductance curve **(b)** of the new devices with electrodeposited porous gold on the gate surface, as a function of the drain voltage.

Conclusions

This research demonstrates the possibility of employing our system as a cell culture chamber where a cyclic rise in hydrostatic pressure may be used without harming the cells. It is important to note that the cyclic increase in hydrostatic pressure has no effect on cell proliferation while the system is in operation, but it may have an impact on cytoskeletal stiffness/rearrangements, which should be further investigated during subsequent tests. In order to evaluate the impact of cytoskeletal changes on these characteristics, analysis of cell migration and wound healing should also be conducted. OECTs have also been shown to operate consistently within culture media after being submerged inside it for more than a week without affecting its pH. Future experiments will be carried out within the chamber while varying the inner hydrostatic pressure, employing human alveolar epithelial cells as well as human adenocarcinomic alveolar epithelial cells (A549 cell line), this time to examine critical growth-related characteristics. This work has also opened the pathway in the direction of the non-invasive integration of live monitoring sensors inside cell culture media, which should be further investigated and developed in future tests. Additional studies should be done on the pH response of OECTs, in order to pave the way for the employing of these devices to detect chemical, physical and biological parameter shifts during cell growth. Upon correct functionalization of the gate electrode, the culture chamber and OECTs are both sufficiently adaptable to investigate, in the near future, various live monitoring approaches, including pH as well as the detection of certain fingerprint analytes associated to tumor cell proliferation. The preliminary efforts made in the direction of the improvement of the device geometry deserve to be further explored, trying to find the best mechanism to grow a porous Au layer on the evaporated Au surface, to maximize its area. The dendritic growth of gold is strongly dependent on external factors such as temperature, and the growth process should be tuned in a more efficient way to improve the reliability of the process. The new flat gate geometry exposed, opens the way to custom-made

electrodepositions which are not only limited to porous gold, but also to different materials which deserve to be investigated. Given the great electrical response of the Ag/AgCl reported in this work, the electrodeposition of Ag and its subsequent chlorination should be taken into account for the future, to boost device performance. The incredible versatility of the Arduino board makes possible the further development of the electronic circuit exposed in this work, in the way to control and detect not only the pneumatic system, but also to work as an interface to a custom made source meter capable to provide a precise electrical input to the OECTs and record their electrical response in live. Overall, this work provided the following achievements in the field of dynamic cell cultures and of in-situ biosensing:

- Development of a cheap and versatile open-source electronic board for the control and investigation of biological experiments, fully compatible with standard cell culture growth methodologies. The system can be readily adapted to different multi-well culture plates and common in vitro systems, to provide a positive or negative hydrostatic pressure stimulus to the growing tissues. The final pressure can be easily adjusted as well as the duty cycle of the mechanical stimuli, and the temperature can be monitored during cell development;
- Demonstration of the biocompatibility of the platform, through cell proliferation tests on HaCaT and HFF-1 cell lines, showing an similar proliferation trend compared to control group, opening the way to further studies involving different cell lines and further development parameters to be monitored;
- Design and development of an in-situ pH sensor based on PEDOT:PSS Organic Electrochemical Transistors, studied to work in the acidic zone of the electrolytic solution under test. The idea behind the development of this sensor is its implementation within the electronic platform described above, in order to monitor this critical physical quantity during cell culture growth;
- Investigation of the response of OECTs with different gate electrode materials and geometries, in order to achieve better stability and higher sensitivity by increasing the surface area exposed to the electrolytic medium, paving the way also to biosensing studies in which the gate electrode is functionalized to detect target molecules during cell development.

Supporting information

OECTs fabrication

The OECTs were fabricated in a clean room environment on a 4'' SiO_2 finished p-type (100) silicon wafer (resistivity 1-10 Ω·cm). The interdigitated source and drain electrodes of the devices (Fig. 30) are obtained by lift-off process. First the wafer was dehydrated on a hot plate (120°C, 5 min). An adhesion promoter was then spin coated (MicroChemicals® TI PRIME), and baked (120°C, 2 min). A layer of image reversal photoresist (MicroChemicals® AZ5214) was then spin-coated on the wafer (500 rpm, 5s, then 2400 rpm, 60 s), and soft baked (105°C, 2 min). The resulting wafer was then exposed with a patterned mask by means of a UV source (Neutronix Quintel, NXQ 4006 Mask Aligner, 5 s, 10 mW/cm^2) and baked again to reverse the tone of the photoresist (105°C, 2 min). The wafer was then exposed (flood exposure) a second time with a UV source (20 s, 10 mW/cm^2) and developed (MicroChemicals® AZ276 MIF) for 35 s, then rinsed in deionized water. An electron beam evaporator was employed (Ulvac EBX-14D) to deposit on the wafer a 10 nm thick Ti adhesion layer (rate 1.5 Å/s), and a 110 nm thick Au layer (rate 1 Å/s). The lift-off process was performed with acetone. The same technique has been repeated to deposit a 150 nm passivation layer of Al_2O_3 on the wafer, leaving two windows, one on the pads and one on the interdigitated electrodes. The wafer was then rinsed with isopropyl alcohol and dried with nitrogen. A (3-glycidyloxypropyl) trimethoxysilane (GOPS) adhesion layer was spin coated (4000 rpm, 60 s) on the wafer (22 mM in a 200:1 solution of toluene:acetic acid), then baked (120°C, 30 s). A solution of PEDOT:PSS was then prepared in the proportion of 93.5% PEDOT:PSS (Heraeus Clevios™), 5% ethylene glycol (Sigma Aldrich®), 1% GOPS (Sigma Aldrich®), 0.5 % 4-dodecylbenzenesulfonic acid (DBSA, Sigma Aldrich®) and spin coated twice on the wafer (4000 rpm, 60 s), baking it between the first and the second spin-coating process (120°C, 30 s) and baking again after the second one (120°C, 5 min), then rinsing in deionized water. The PEDOT:PSS layer was then cross-linked in a vacuum oven (150°C, 2 h). The PEDOT:PSS layer resulted in a measured thickness of 200 nm (Tencor P-10 Surface Profiler). A 20 μm thick photoresist layer was then deposited on the wafer (MicroChemicals® AZ9260) spinning it and soft baking it twice (500 rpm for 5s, then 2400 rpm for 60 s, 100°C, 10 min).

The resulting photoresist was then left resting for 4 h to rehydratate and avoid bubble formation during the UV exposure. The wafer was then UV exposed with a mask (80 s @11 mW/cm^2) and developed in a 3:1 solution of deionized water:developer (MicroChemicals® AZ400K) for 2 min. A dry etching process was then used to pattern the PEDOT:PSS through O_2 plasma (Electrotech Plasmafab 508), with the following parameters: O_2 flow 100 sccm, RF frequency 13.56 MHz, RF power 300 W. The etching process has been divided in 6 different etching/cooling steps lasting 30 min each, in order not to make the temperature exceeds the value at which the photoresist etching rate becomes significantly higher than that of the PEDOT: PSS. The wafer was finally developed in acetone, rinsed in isopropyl alcohol and dried with nitrogen, then laser cut to obtain chips containing three devices each.

Arduino sketch

```
#include <Wire.h>
byte fetch_humidity_temperature(unsigned int *p_Humidity, unsigned int *p_Temperature);
void print_float(float f, int num_digits);
#define TRUE 1;
#define FALSE 0;
int analogPin = A3;
int val = 0;
int Pressure;
int timer_p=2500;
int timer_p=2500;
int t=0;
void setup(void)
{
  Serial.begin(9600);
  Wire.begin();
  pinMode(2, OUTPUT);
  pinMode(4, OUTPUT);
  pinMode(6, OUTPUT);
```

```
  pinMode(7, OUTPUT);
  pinMode(8, OUTPUT);
  Serial.println(">>>>>>>>>>>>>>>>>>>>>>>>>");
}
void colore (unsigned char rosso, unsigned char verde, unsigned char blu)
{
 analogWrite(8, rosso);
 analogWrite(7, blu);
 analogWrite(6, verde);
}
void loop(void)
{
  byte _status;
  unsigned int H_dat, T_dat;
  float RH, T_C;

  while(1)
  {
    for(t=0;t<timer_p;t++)
    {
     digitalWrite(2, HIGH);
     digitalWrite(4, LOW);
     colore(0,255,0);

     _status = fetch_humidity_temperature(&H_dat, &T_dat);
     RH = (float) H_dat * 6.10e-3;
     T_C = (float) T_dat * 1.007e-2 - 40.0;
     val = analogRead(analogPin);
    if (val<38) {val = 38;}
    if (val>1015) {val = 1015;}
    Pressure = map (val, 38, 1015, 0, 10000);
```

```
      Serial.print(Pressure);
      Serial.print("  ");
      print_float(T_C, 2);
      Serial.print("  ");
      print_float(RH, 1);
      Serial.println();
     }
     for(t=0;t<timer_sv;t++)
     {
      digitalWrite(2, LOW);
      digitalWrite(4, HIGH);
      colore(0,255,0);
      _status = fetch_humidity_temperature(&H_dat, &T_dat);
      RH = (float) H_dat * 6.10e-3;
      T_C = (float) T_dat * 1.007e-2 - 40.0;
      val = analogRead(analogPin);
     if (val<38) {val = 38;}
     if (val>1015) {val = 1015;}
     Pressure = map (val, 38, 1015, 0, 10000);
     Serial.print(Pressure);
     Serial.print("  ");
     print_float(T_C, 2);
     Serial.print("  ");
     print_float(RH, 1);
     Serial.println();
     }
   }
}
byte fetch_humidity_temperature(unsigned int *p_H_dat, unsigned int *p_T_dat)
{
    byte address, Hum_H, Hum_L, Temp_H, Temp_L, _status;
```

```
    unsigned int H_dat, T_dat;
    address = 0x27;;
    Wire.beginTransmission(address);
    Wire.endTransmission();
    delay(100);
    Wire.requestFrom((int)address, (int) 4);
    Hum_H = Wire.read();
    Hum_L = Wire.read();
    Temp_H = Wire.read();
    Temp_L = Wire.read();
    Wire.endTransmission();
    _status = (Hum_H >> 6) & 0x03;
    Hum_H = Hum_H & 0x3f;
    H_dat = (((unsigned int)Hum_H) << 8) | Hum_L;
    T_dat = (((unsigned int)Temp_H) << 8) | Temp_L;
    T_dat = T_dat / 4;
    *p_H_dat = H_dat;
    *p_T_dat = T_dat;
    return(_status);
}
void print_float(float f, int num_digits)
{
   int f_int;
   int pows_of_ten[4] = {1, 10, 100, 1000};
   int multiplier, whole, fract, d, n;
   multiplier = pows_of_ten[num_digits];
   if (f < 0.0)
   {
      f = -f;
      Serial.print("-");
   }
```

```
  whole = (int) f;
  fract = (int) (multiplier * (f - (float)whole));
  Serial.print(whole);
  Serial.print(".");
  for (n=num_digits-1; n>=0; n--) // print each digit with no leading zero suppression
  {
    d = fract / pows_of_ten[n];
    Serial.print(d);
    fract = fract % pows_of_ten[n];
  }
}
```

References

[1] C. Moraes, G. Mehta, S. C. Lesher-Perez, e S. Takayama, «Organs-on-a-Chip: A Focus on Compartmentalized Microdevices», *Ann Biomed Eng*, vol. 40, fasc. 6, pp. 1211–1227, giu. 2012, doi: 10.1007/s10439-011-0455-6.

[2] P. Pound, S. Ebrahim, P. Sandercock, M. B. Bracken, e I. Roberts, «Where is the evidence that animal research benefits humans?», *BMJ*, vol. 328, fasc. 7438, pp. 514–517, feb. 2004, doi: 10.1136/bmj.328.7438.514.

[3] J. J. Sanz-Ezquerro, A. E. Münsterberg, e S. Stricker, «Editorial: Signaling Pathways in Embryonic Development», *Front. Cell Dev. Biol.*, vol. 5, p. 76, ago. 2017, doi: 10.3389/fcell.2017.00076.

[4] F. Nyberg e M. Hallberg, «Growth hormone and cognitive function», *Nat Rev Endocrinol*, vol. 9, fasc. 6, pp. 357–365, giu. 2013, doi: 10.1038/nrendo.2013.78.

[5] D. E. Discher, D. J. Mooney, e P. W. Zandstra, «Growth Factors, Matrices, and Forces Combine and Control Stem Cells», *Science*, vol. 324, fasc. 5935, pp. 1673–1677, giu. 2009, doi: 10.1126/science.1171643.

[6] M. Aragona *et al.*, «A Mechanical Checkpoint Controls Multicellular Growth through YAP/TAZ Regulation by Actin-Processing Factors», *Cell*, vol. 154, fasc. 5, pp. 1047–1059, ago. 2013, doi: 10.1016/j.cell.2013.07.042.

[7] T. Iskratsch, H. Wolfenson, e M. P. Sheetz, «Appreciating force and shape — the rise of mechanotransduction in cell biology», *Nat Rev Mol Cell Biol*, vol. 15, fasc. 12, pp. 825–833, dic. 2014, doi: 10.1038/nrm3903.

[8] M. A. Wozniak e C. S. Chen, «Mechanotransduction in development: a growing role for contractility», *Nat Rev Mol Cell Biol*, vol. 10, fasc. 1, pp. 34–43, gen. 2009, doi: 10.1038/nrm2592.

[9] T. Mammoto, A. Mammoto, A. Jiang, E. Jiang, B. Hashmi, e D. E. Ingber, «Mesenchymal condensation-dependent accumulation of collagen VI stabilizes organ-specific cell fates during embryonic tooth formation: ECM Induction by Cell Compaction», *Dev. Dyn.*, vol. 244, fasc. 6, pp. 713–723, giu. 2015, doi: 10.1002/dvdy.24264.

[10] J. He, Z. Liu, X. Zhu, H. Xia, H. Gao, e J. Lu, «Ultrasonic Microbubble Cavitation Enhanced Tissue Permeability and Drug Diffusion in Solid Tumor Therapy», *Pharmaceutics*, vol. 14, fasc. 8, p. 1642, ago. 2022, doi: 10.3390/pharmaceutics14081642.

[11] C. Chen, X. Bai, Y. Ding, e I.-S. Lee, «Electrical stimulation as a novel tool for regulating cell behavior in tissue engineering», *Biomater Res*, vol. 23, fasc. 1, p. 25, dic. 2019, doi: 10.1186/s40824-019-0176-8.

[12] H. Wolfenson, B. Yang, e M. P. Sheetz, «Steps in Mechanotransduction Pathways that Control Cell Morphology», *Annu. Rev. Physiol.*, vol. 81, fasc. 1, pp. 585–605, feb. 2019, doi: 10.1146/annurev-physiol-021317-121245.

[13] S. Kumari, S. Vermeulen, B. van der Veer, A. Carlier, J. de Boer, e D. Subramanyam, «Shaping Cell Fate: Influence of Topographical Substratum Properties on Embryonic Stem Cells», *Tissue Engineering Part B: Reviews*, vol. 24, fasc. 4, pp. 255–266, ago. 2018, doi: 10.1089/ten.teb.2017.0468.

[14] Y. Song, J. Soto, B. Chen, L. Yang, e S. Li, «Cell engineering: Biophysical regulation of the nucleus», *Biomaterials*, vol. 234, p. 119743, mar. 2020, doi: 10.1016/j.biomaterials.2019.119743.

[15] D. Douguet e E. Honoré, «Mammalian Mechanoelectrical Transduction: Structure and Function of Force-Gated Ion Channels», *Cell*, vol. 179, fasc. 2, pp. 340–354, ott. 2019, doi: 10.1016/j.cell.2019.08.049.

[16] J.-H. Lee, D.-H. Kim, H.-H. Lee, e H.-W. Kim, «Role of nuclear mechanosensitivity in determining cellular responses to forces and biomaterials», *Biomaterials*, vol. 197, pp. 60–71, mar. 2019, doi: 10.1016/j.biomaterials.2019.01.010.

[17] K. H. Vining e D. J. Mooney, «Mechanical forces direct stem cell behaviour in development and regeneration», *Nat Rev Mol Cell Biol*, vol. 18, fasc. 12, pp. 728–742, dic. 2017, doi: 10.1038/nrm.2017.108.

[18] Y. Y. Dong *et al.*, «K2P channel gating mechanisms revealed by structures of TREK-2 and a complex with Prozac», *Science*, vol. 347, fasc. 6227, pp. 1256–1259, mar. 2015, doi: 10.1126/science.1261512.

[19] S. E. Murthy, A. E. Dubin, e A. Patapoutian, «Piezos thrive under pressure: mechanically activated ion channels in health and disease», *Nat Rev Mol Cell Biol*, vol. 18, fasc. 12, pp. 771–783, dic. 2017, doi: 10.1038/nrm.2017.92.

[20] J. M. Kefauver, A. B. Ward, e A. Patapoutian, «Discoveries in structure and physiology of mechanically activated ion channels», *Nature*, vol. 587, fasc. 7835, pp. 567–576, nov. 2020, doi: 10.1038/s41586-020-2933-1.

[21] Y. Jia *et al.*, «TMC1 and TMC2 Proteins Are Pore-Forming Subunits of Mechanosensitive Ion Channels», *Neuron*, vol. 105, fasc. 2, pp. 310-321.e3, gen. 2020, doi: 10.1016/j.neuron.2019.10.017.

[22] W. Chen, Y. Shao, X. Li, G. Zhao, e J. Fu, «Nanotopographical surfaces for stem cell fate control: Engineering mechanobiology from the bottom», *Nano Today*, vol. 9, fasc. 6, pp. 759–784, dic. 2014, doi: 10.1016/j.nantod.2014.12.002.

[23] B. Geiger, J. P. Spatz, e A. D. Bershadsky, «Environmental sensing through focal adhesions», *Nat Rev Mol Cell Biol*, vol. 10, fasc. 1, pp. 21–33, gen. 2009, doi: 10.1038/nrm2593.

[24] C. Guilluy, V. Swaminathan, R. Garcia-Mata, E. Timothy O'Brien, R. Superfine, e K. Burridge, «The Rho GEFs LARG and GEF-H1 regulate the mechanical response to force on integrins», *Nat Cell Biol*, vol. 13, fasc. 6, pp. 722–727, giu. 2011, doi: 10.1038/ncb2254.

[25] J. D. Humphrey, E. R. Dufresne, e M. A. Schwartz, «Mechanotransduction and extracellular matrix homeostasis», *Nat Rev Mol Cell Biol*, vol. 15, fasc. 12, pp. 802–812, dic. 2014, doi: 10.1038/nrm3896.

[26] P. Isermann e J. Lammerding, «Nuclear Mechanics and Mechanotransduction in Health and Disease», *Current Biology*, vol. 23, fasc. 24, pp. R1113–R1121, dic. 2013, doi: 10.1016/j.cub.2013.11.009.

[27] B. D. Hoffman, C. Grashoff, e M. A. Schwartz, «Dynamic molecular processes mediate cellular mechanotransduction», *Nature*, vol. 475, fasc. 7356, pp. 316–323, lug. 2011, doi: 10.1038/nature10316.

[28] T. Yokokura, Y. Nakashima, Y. Yonemoto, Y. Hikichi, e Y. Nakanishi, «Method for measuring Young's modulus of cells using a cell compression microdevice», *International Journal of Engineering Science*, vol. 114, pp. 41–48, mag. 2017, doi: 10.1016/j.ijengsci.2017.02.002.

[29] K. Pogoda *et al.*, «Depth-sensing analysis of cytoskeleton organization based on AFM data», *Eur Biophys J*, vol. 41, fasc. 1, pp. 79–87, gen. 2012, doi: 10.1007/s00249-011-0761-9.

[30] A. M. Collinsworth, S. Zhang, W. E. Kraus, e G. A. Truskey, «Apparent elastic modulus and hysteresis of skeletal muscle cells throughout differentiation», *American Journal of Physiology-Cell Physiology*, vol. 283, fasc. 4, pp. C1219–C1227, ott. 2002, doi: 10.1152/ajpcell.00502.2001.

[31] D. Zeng *et al.*, «Young's modulus of elasticity of Schlemm's canal endothelial cells», *Biomech Model Mechanobiol*, vol. 9, fasc. 1, pp. 19–33, feb. 2010, doi: 10.1007/s10237-009-0156-3.

[32] R. O. Hynes, «The Extracellular Matrix: Not Just Pretty Fibrils», *Science*, vol. 326, fasc. 5957, pp. 1216–1219, nov. 2009, doi: 10.1126/science.1176009.

[33] M. Floren, W. Bonani, A. Dharmarajan, A. Motta, C. Migliaresi, e W. Tan, «Human mesenchymal stem cells cultured on silk hydrogels with variable stiffness and growth factor differentiate into mature smooth muscle cell phenotype», *Acta Biomaterialia*, vol. 31, pp. 156–166, feb. 2016, doi: 10.1016/j.actbio.2015.11.051.

[34] A. M. Cozzolino *et al.*, «Modulating the Substrate Stiffness to Manipulate Differentiation of Resident Liver Stem Cells and to Improve the Differentiation State of Hepatocytes», *Stem Cells International*, vol. 2016, pp. 1–12, 2016, doi: 10.1155/2016/5481493.

[35] S. Paiva *et al.*, «Polyacrylamide Hydrogels with Rigidity-Independent Surface Chemistry Show Limited Long-Term Maintenance of Pluripotency of Human Induced Pluripotent Stem Cells on Soft Substrates», *ACS Biomater. Sci. Eng.*, vol. 6, fasc. 1, pp. 340–351, gen. 2020, doi: 10.1021/acsbiomaterials.9b01189.

[36] M. Guvendiren e J. A. Burdick, «Stiffening hydrogels to probe short- and long-term cellular responses to dynamic mechanics», *Nat Commun*, vol. 3, fasc. 1, p. 792, apr. 2012, doi: 10.1038/ncomms1792.

[37] H. Y. Yoshikawa *et al.*, «Quantitative Evaluation of Mechanosensing of Cells on Dynamically Tunable Hydrogels», *J. Am. Chem. Soc.*, vol. 133, fasc. 5, pp. 1367–1374, feb. 2011, doi: 10.1021/ja1060615.

[38] B. Carrion *et al.*, «The Synergistic Effects of Matrix Stiffness and Composition on the Response of Chondroprogenitor Cells in a 3D Precondensation Microenvironment», *Adv. Healthcare Mater.*, vol. 5, fasc. 10, pp. 1192–1202, mag. 2016, doi: 10.1002/adhm.201501017.

[39] D. Kim, J. Lee, e G. Kim, «Biomimetic gelatin/HA biocomposites with effective elastic properties and 3D-structural flexibility using a 3D-printing process», *Additive Manufacturing*, vol. 36, p. 101616, dic. 2020, doi: 10.1016/j.addma.2020.101616.

[40] D. Wei *et al.*, «Mechanics-Controlled Dynamic Cell Niches Guided Osteogenic Differentiation of Stem Cells via Preserved Cellular Mechanical Memory», *ACS Appl. Mater. Interfaces*, vol. 12, fasc. 1, pp. 260–274, gen. 2020, doi: 10.1021/acsami.9b18425.

[41] M. Hua *et al.*, «Strong tough hydrogels via the synergy of freeze-casting and salting out», *Nature*, vol. 590, fasc. 7847, pp. 594–599, feb. 2021, doi: 10.1038/s41586-021-03212-z.

[42] J. Padmanabhan *et al.*, «Engineering Cellular Response Using Nanopatterned Bulk Metallic Glass», *ACS Nano*, vol. 8, fasc. 5, pp. 4366–4375, mag. 2014, doi: 10.1021/nn501874q.

[43] C. W. Kuo, D.-Y. Chueh, e P. Chen, «Investigation of size–dependent cell adhesion on nanostructured interfaces», *J Nanobiotechnol*, vol. 12, fasc. 1, p. 54, dic. 2014, doi: 10.1186/s12951-014-0054-4.

[44] A. R. Cameron, J. E. Frith, G. A. Gomez, A. S. Yap, e J. J. Cooper-White, «The effect of time-dependent deformation of viscoelastic hydrogels on myogenic induction and Rac1 activity in mesenchymal stem cells», *Biomaterials*, vol. 35, fasc. 6, pp. 1857–1868, feb. 2014, doi: 10.1016/j.biomaterials.2013.11.023.

[45] B. Yang *et al.*, «Enhanced mechanosensing of cells in synthetic 3D matrix with controlled biophysical dynamics», *Nat Commun*, vol. 12, fasc. 1, p. 3514, giu. 2021, doi: 10.1038/s41467-021-23120-0.

[46] O. Chaudhuri *et al.*, «Substrate stress relaxation regulates cell spreading», *Nat Commun*, vol. 6, fasc. 1, p. 6365, feb. 2015, doi: 10.1038/ncomms7365.

[47] O. Chaudhuri *et al.*, «Hydrogels with tunable stress relaxation regulate stem cell fate and activity», *Nature Mater*, vol. 15, fasc. 3, pp. 326–334, mar. 2016, doi: 10.1038/nmat4489.

[48] J.-S. Kim *et al.*, «Chondrogenic differentiation of human ASCs by stiffness control in 3D fibrin hydrogel», *Biochemical and Biophysical Research Communications*, vol. 522, fasc. 1, pp. 213–219, gen. 2020, doi: 10.1016/j.bbrc.2019.11.049.

[49] S. Tan, J. Y. Fang, Z. Yang, M. E. Nimni, e B. Han, «The synergetic effect of hydrogel stiffness and growth factor on osteogenic differentiation», *Biomaterials*, vol. 35, fasc. 20, pp. 5294–5306, lug. 2014, doi: 10.1016/j.biomaterials.2014.02.040.

[50] A. J. Engler, S. Sen, H. L. Sweeney, e D. E. Discher, «Matrix Elasticity Directs Stem Cell Lineage Specification», *Cell*, vol. 126, fasc. 4, pp. 677–689, ago. 2006, doi: 10.1016/j.cell.2006.06.044.

[51] K. Ye, L. Cao, S. Li, L. Yu, e J. Ding, «Interplay of Matrix Stiffness and Cell–Cell Contact in Regulating Differentiation of Stem Cells», *ACS Appl. Mater. Interfaces*, vol. 8, fasc. 34, pp. 21903–21913, ago. 2016, doi: 10.1021/acsami.5b09746.

[52] P. Fratzl e R. Weinkamer, «Nature's hierarchical materials», *Progress in Materials Science*, vol. 52, fasc. 8, pp. 1263–1334, nov. 2007, doi: 10.1016/j.pmatsci.2007.06.001.

[53] L. C. Palmer, C. J. Newcomb, S. R. Kaltz, E. D. Spoerke, e S. I. Stupp, «Biomimetic Systems for Hydroxyapatite Mineralization Inspired By Bone and Enamel», *Chem. Rev.*, vol. 108, fasc. 11, pp. 4754–4783, nov. 2008, doi: 10.1021/cr8004422.

[54] S. Namgung, K. Y. Baik, J. Park, e S. Hong, «Controlling the Growth and Differentiation of Human Mesenchymal Stem Cells by the Arrangement of Individual Carbon Nanotubes», *ACS Nano*, vol. 5, fasc. 9, pp. 7383–7390, set. 2011, doi: 10.1021/nn2023057.

[55] S. Wu, Y. Wang, P. N. Streubel, e B. Duan, «Living nanofiber yarn-based woven biotextiles for tendon tissue engineering using cell tri-culture and mechanical stimulation», *Acta Biomaterialia*, vol. 62, pp. 102–115, ott. 2017, doi: 10.1016/j.actbio.2017.08.043.

[56] A. Carvalho *et al.*, «Femtosecond laser microstructuring of alumina toughened zirconia for surface functionalization of dental implants», *Ceramics International*, vol. 46, fasc. 2, pp. 1383–1389, feb. 2020, doi: 10.1016/j.ceramint.2019.09.101.

[57] M. F. A. Cutiongco, B. S. Jensen, P. M. Reynolds, e N. Gadegaard, «Predicting gene expression using morphological cell responses to nanotopography», *Nat Commun*, vol. 11, fasc. 1, p. 1384, mar. 2020, doi: 10.1038/s41467-020-15114-1.

[58] X. Li *et al.*, «A nanostructure platform for live-cell manipulation of membrane curvature», *Nat Protoc*, vol. 14, fasc. 6, pp. 1772–1802, giu. 2019, doi: 10.1038/s41596-019-0161-7.

[59] P. Li *et al.*, «The promoting effect on pre-osteoblast growth under electrical and magnetic double stimulation based on PEDOT/Fe_3O_4/PLGA magnetic-conductive bi-functional scaffolds», *J. Mater. Chem. B*, vol. 6, fasc. 30, pp. 4952–4962, 2018, doi: 10.1039/C8TB00985F.

[60] A. Omidinia-Anarkoli *et al.*, «Solvent-Induced Nanotopographies of Single Microfibers Regulate Cell Mechanotransduction», *ACS Appl. Mater. Interfaces*, vol. 11, fasc. 8, pp. 7671–7685, feb. 2019, doi: 10.1021/acsami.8b17955.

[61] E. G. Long, M. Buluk, M. B. Gallagher, J. M. Schneider, e J. L. Brown, «Human mesenchymal stem cell morphology, migration, and differentiation on micro and nano-textured titanium», *Bioactive Materials*, vol. 4, pp. 249–255, dic. 2019, doi: 10.1016/j.bioactmat.2019.08.001.

[62] A. Mazare *et al.*, «Black TiO2 nanotubes: Efficient electrodes for triggering electric field-induced stimulation of stem cell growth», *Acta Biomaterialia*, vol. 97, pp. 681–688, ott. 2019, doi: 10.1016/j.actbio.2019.08.021.

[63] C. Yang *et al.*, «Stimulation of osteogenesis and angiogenesis by micro/nano hierarchical hydroxyapatite *via* macrophage immunomodulation», *Nanoscale*, vol. 11, fasc. 38, pp. 17699–17708, 2019, doi: 10.1039/C9NR05730G.

[64] M. Xu *et al.*, «Easy, Scalable, Robust, Micropatterned Silk Fibroin Cell Substrates», *Adv. Mater. Interfaces*, vol. 6, fasc. 8, p. 1801822, apr. 2019, doi: 10.1002/admi.201801822.

[65] E. Martinez-Campos *et al.*, «Wrinkled Hydrogel Surfaces with Modulated Surface Chemistry and Topography: Evaluation As Supports for Cell Growth and Transplant», *ACS Appl. Bio Mater.*, vol. 2, fasc. 2, pp. 654–664, feb. 2019, doi: 10.1021/acsabm.8b00460.

[66] J. You *et al.*, «Impact of Nanotopography, Heparin Hydrogel Microstructures, and Encapsulated Fibroblasts on Phenotype of Primary Hepatocytes», *ACS Appl. Mater. Interfaces*, vol. 7, fasc. 23, pp. 12299–12308, giu. 2015, doi: 10.1021/am504614e.

[67] X. Pei *et al.*, «Creating hierarchical porosity hydroxyapatite scaffolds with osteoinduction by three-dimensional printing and microwave sintering», *Biofabrication*, vol. 9, fasc. 4, p. 045008, nov. 2017, doi: 10.1088/1758-5090/aa90ed.

[68] F. J. Harding *et al.*, «Ordered Silicon Pillar Arrays Prepared by Electrochemical Micromachining: Substrates for High-Efficiency Cell Transfection», *ACS Appl. Mater. Interfaces*, vol. 8, fasc. 43, pp. 29197–29202, nov. 2016, doi: 10.1021/acsami.6b07850.

[69] J. Litowczenko, B. M. Maciejewska, J. K. Wychowaniec, M. Kościński, S. Jurga, e A. Warowicka, «Groove-patterned surfaces induce

morphological changes in cells of neuronal origin», *J Biomed Mater Res*, vol. 107, fasc. 10, pp. 2244–2256, ott. 2019, doi: 10.1002/jbm.a.36733.

[70] S. A. Fraser, Y. Ting, K. S. Mallon, A. E. Wendt, C. J. Murphy, e P. F. Nealey, «Sub-micron and nanoscale feature depth modulates alignment of stromal fibroblasts and corneal epithelial cells in serum-rich and serum-free media», *J. Biomed. Mater. Res.*, vol. 86A, fasc. 3, pp. 725–735, set. 2008, doi: 10.1002/jbm.a.31519.

[71] N. W. Karuri *et al.*, «Biological length scale topography enhances cell-substratum adhesion of human corneal epithelial cells», *Journal of Cell Science*, vol. 117, fasc. 15, pp. 3153–3164, lug. 2004, doi: 10.1242/jcs.01146.

[72] T. Kimura, M. Kondo, Y. Hashimoto, T. Fujisato, N. Nakamura, e A. Kishida, «Surface Topography of PDMS Replica Transferred from Various Decellularized Aortic Lumens Affects Cellular Orientation», *ACS Biomater. Sci. Eng.*, vol. 5, fasc. 11, pp. 5721–5726, nov. 2019, doi: 10.1021/acsbiomaterials.8b01536.

[73] X. Wu *et al.*, «A free-form patterning method enabling endothelialization under dynamic flow», *Biomaterials*, vol. 273, p. 120816, giu. 2021, doi: 10.1016/j.biomaterials.2021.120816.

[74] M. Lasgorceix *et al.*, «Micropatterning of beta tricalcium phosphate bioceramic surfaces, by femtosecond laser, for bone marrow stem cells behavior assessment», *Materials Science and Engineering: C*, vol. 95, pp. 371–380, feb. 2019, doi: 10.1016/j.msec.2018.03.004.

[75] P. Kuppan, S. Sethuraman, e U. M. Krishnan, «Interaction of human smooth muscle cells with nanofibrous scaffolds: Effect of fiber orientation on cell adhesion, proliferation, and functional gene expression: Human Smooth Muscle Cells with Nanofibrous Scaffolds», *J. Biomed. Mater. Res.*, vol. 103, fasc. 7, pp. 2236–2250, lug. 2015, doi: 10.1002/jbm.a.35360.

[76] E. Uslu, D. Mimiroglu, e B. Ercan, «Nanofeature Size and Morphology of Tantalum Oxide Surfaces Control Osteoblast Functions», *ACS Appl. Bio Mater.*, vol. 4, fasc. 1, pp. 780–794, gen. 2021, doi: 10.1021/acsabm.0c01354.

[77] B. Wysocki *et al.*, «The influence of chemical polishing of titanium scaffolds on their mechanical strength and in-vitro cell response», *Materials Science and Engineering: C*, vol. 95, pp. 428–439, feb. 2019, doi: 10.1016/j.msec.2018.04.019.

[78] O. C. Aktas *et al.*, «Controlling fibroblast adhesion and proliferation by 1D Al_2O_3 nanostructures», *IET nanobiotechnol.*, vol. 13, fasc. 6, pp. 621–625, ago. 2019, doi: 10.1049/iet-nbt.2018.5088.

[79] F. Wang *et al.*, «Micropatterned Thermoresponsive Surfaces by Polymerization of Monomer Crystals: Modulating Cellular Morphology and Cell–Substrate Interactions», *Anal. Chem.*, vol. 84, fasc. 21, pp. 9439–9445, nov. 2012, doi: 10.1021/ac302267z.

[80] X. Ye *et al.*, «Fabrication and characterization of porous 3D whisker-covered calcium phosphate scaffolds», *Materials Letters*, vol. 128, pp. 179–182, ago. 2014, doi: 10.1016/j.matlet.2014.04.142.

[81] X. Liu e S. Wang, «Three-dimensional nano-biointerface as a new platform for guiding cell fate», *Chem. Soc. Rev.*, vol. 43, fasc. 8, pp. 2385–2401, 2014, doi: 10.1039/C3CS60419E.

[82] R. Bassel-Duby e E. N. Olson, «Signaling Pathways in Skeletal Muscle Remodeling», *Annu. Rev. Biochem.*, vol. 75, fasc. 1, pp. 19–37, giu. 2006, doi: 10.1146/annurev.biochem.75.103004.142622.

[83] K. Naruse, T. Yamada, X.-R. Sai, M. Hamaguchi, e M. Sokabe, «Pp125FAK is required for stretch dependent morphological response of endothelial cells», *Oncogene*, vol. 17, fasc. 4, pp. 455–463, lug. 1998, doi: 10.1038/sj.onc.1201950.

[84] A. O. Stucki *et al.*, «A lung-on-a-chip array with an integrated bio-inspired respiration mechanism», *Lab Chip*, vol. 15, fasc. 5, pp. 1302–1310, 2015, doi: 10.1039/C4LC01252F.

[85] P. de Haan *et al.*, «Digestion-on-a-chip: a continuous-flow modular microsystem recreating enzymatic digestion in the gastrointestinal tract», *Lab Chip*, vol. 19, fasc. 9, pp. 1599–1609, 2019, doi: 10.1039/C8LC01080C.

[86] R. Villenave *et al.*, «Human Gut-On-A-Chip Supports Polarized Infection of Coxsackie B1 Virus In Vitro», *PLoS ONE*, vol. 12, fasc. 2, p. e0169412, feb. 2017, doi: 10.1371/journal.pone.0169412.

[87] O. T. Guenat e F. Berthiaume, «Incorporating mechanical strain in organs-on-a-chip: Lung and skin», *Biomicrofluidics*, vol. 12, fasc. 4, p. 042207, lug. 2018, doi: 10.1063/1.5024895.

[88] P. Poulin e S. Haddad, «Toward a new paradigm for the efficient in vitro–in vivo extrapolation of metabolic clearance in humans from hepatocyte data», *Journal of Pharmaceutical Sciences*, vol. 102, fasc. 9, pp. 3239–3251, set. 2013, doi: 10.1002/jps.23502.

[89] D. Huh *et al.*, «Microfabrication of human organs-on-chips», *Nat Protoc*, vol. 8, fasc. 11, pp. 2135–2157, nov. 2013, doi: 10.1038/nprot.2013.137.

[90] R. A. Kellogg, R. Gómez-Sjöberg, A. A. Leyrat, e S. Tay, «High-throughput microfluidic single-cell analysis pipeline for studies of signaling dynamics», *Nat Protoc*, vol. 9, fasc. 7, pp. 1713–1726, lug. 2014, doi: 10.1038/nprot.2014.120.

[91] T. Wang *et al.*, «3D uniaxial mechanical stimulation induces tenogenic differentiation of tendon-derived stem cells through a PI3K/AKT signaling pathway», *FASEB j.*, vol. 32, fasc. 9, pp. 4804–4814, set. 2018, doi: 10.1096/fj.201701384R.

[92] K. Y. Xie, L. Yang, K. Chen, e Q. Li, «In vitro study of the effect of cyclic strains on the dermal fibroblast (GM3384) morphology—Mapping of cell responses to strain field», *Medical Engineering & Physics*, vol. 34, fasc. 7, pp. 826–831, set. 2012, doi: 10.1016/j.medengphy.2011.09.024.

[93] S. Virjula *et al.*, «The effect of equiaxial stretching on the osteogenic differentiation and mechanical properties of human adipose stem cells», *Journal of the Mechanical Behavior of Biomedical Materials*, vol. 72, pp. 38–48, ago. 2017, doi: 10.1016/j.jmbbm.2017.04.016.

[94] H. Liu *et al.*, «Microdevice arrays with strain sensors for 3D mechanical stimulation and monitoring of engineered tissues», *Biomaterials*, vol. 172, pp. 30–40, lug. 2018, doi: 10.1016/j.biomaterials.2018.04.041.

[95] S.-Y. Chu *et al.*, «Mechanical stretch induces hair regeneration through the alternative activation of macrophages», *Nat Commun*, vol. 10, fasc. 1, p. 1524, apr. 2019, doi: 10.1038/s41467-019-09402-8.

[96] B. Sebastian e P. S. Dittrich, «Microfluidics to Mimic Blood Flow in Health and Disease», *Annu. Rev. Fluid Mech.*, vol. 50, fasc. 1, pp. 483–504, gen. 2018, doi: 10.1146/annurev-fluid-010816-060246.

[97] J. H. Jeon e O. C. Jeong, «Effect of shear stress magnitude on intracellular calcium expression in bone cells», *Microelectronic Engineering*, vol. 97, pp. 329–332, set. 2012, doi: 10.1016/j.mee.2012.03.018.

[98] F. Kurth, A. Franco-Obregón, M. Casarosa, S. K. Küster, K. Wuertz-Kozak, e P. S. Dittrich, «Transient receptor potential vanilloid 2-mediated shear-stress responses in C2C12 myoblasts are regulated by serum and extracellular matrix», *FASEB j.*, vol. 29, fasc. 11, pp. 4726–4737, nov. 2015, doi: 10.1096/fj.15-275396.

[99] E. P. Efstathopoulos, G. Patatoukas, I. Pantos, O. Benekos, D. Katritsis, e N. L. Kelekis, «Wall shear stress calculation in ascending aorta using phase contrast magnetic resonance imaging. Investigating effective ways to calculate it in clinical practice», *Physica Medica*, vol. 24, fasc. 4, pp. 175–181, dic. 2008, doi: 10.1016/j.ejmp.2008.01.004.

[100] L. K. Chin, J. Q. Yu, Y. Fu, T. Yu, A. Q. Liu, e K. Q. Luo, «Production of reactive oxygen species in endothelial cells under different pulsatile shear stresses and glucose concentrations», *Lab Chip*, vol. 11, fasc. 11, p. 1856, 2011, doi: 10.1039/c0lc00651c.

[101] S. Vijayavenkataraman, W.-C. Yan, W. F. Lu, C.-H. Wang, e J. Y. H. Fuh, «3D bioprinting of tissues and organs for regenerative medicine», *Advanced Drug Delivery Reviews*, vol. 132, pp. 296–332, lug. 2018, doi: 10.1016/j.addr.2018.07.004.

[102] N. S. Bhise *et al.*, «Organ-on-a-chip platforms for studying drug delivery systems», *Journal of Controlled Release*, vol. 190, pp. 82–93, set. 2014, doi: 10.1016/j.jconrel.2014.05.004.

[103] W.-T. Chen *et al.*, «Alteration of mesenchymal stem cells polarity by laminar shear stimulation promoting β-catenin nuclear localization»,

Biomaterials, vol. 190–191, pp. 1–10, gen. 2019, doi: 10.1016/j.biomaterials.2018.10.026.

[104] Y. Fan *et al.*, «Skeletal loading regulates breast cancer-associated osteolysis in a loading intensity-dependent fashion», *Bone Res*, vol. 8, fasc. 1, p. 9, feb. 2020, doi: 10.1038/s41413-020-0083-6.

[105] A. Schubert, M. Cattaruzza, M. Hecker, D. Darmer, J. Holtz, e H. Morawietz, «Shear Stress–Dependent Regulation of the Human β-Tubulin Folding Cofactor D Gene», *Circulation Research*, vol. 87, fasc. 12, pp. 1188–1194, dic. 2000, doi: 10.1161/01.RES.87.12.1188.

[106] J. Scheinpflug *et al.*, «Journey into Bone Models: A Review», *Genes*, vol. 9, fasc. 5, p. 247, mag. 2018, doi: 10.3390/genes9050247.

[107] A. H. Huang, M. J. Farrell, e R. L. Mauck, «Mechanics and mechanobiology of mesenchymal stem cell-based engineered cartilage», *Journal of Biomechanics*, vol. 43, fasc. 1, pp. 128–136, gen. 2010, doi: 10.1016/j.jbiomech.2009.09.018.

[108] C. Meinert, K. Schrobback, D. W. Hutmacher, e T. J. Klein, «A novel bioreactor system for biaxial mechanical loading enhances the properties of tissue-engineered human cartilage», *Sci Rep*, vol. 7, fasc. 1, p. 16997, dic. 2017, doi: 10.1038/s41598-017-16523-x.

[109] W. Hoffmann, «Novel perfused compression bioreactor system as an in vitro model to investigate fracture healing», *Front. Bioeng. Biotechnol.*, vol. 3, 2015, doi: 10.3389/fbioe.2015.00010.

[110] Y. Torisawa *et al.*, «Bone marrow–on–a–chip replicates hematopoietic niche physiology in vitro», *Nat Methods*, vol. 11, fasc. 6, pp. 663–669, giu. 2014, doi: 10.1038/nmeth.2938.

[111] Y. C. Kim, J. H. Kang, S.-J. Park, E.-S. Yoon, e J.-K. Park, «Microfluidic biomechanical device for compressive cell stimulation and lysis», *Sensors and Actuators B: Chemical*, vol. 128, fasc. 1, pp. 108–116, dic. 2007, doi: 10.1016/j.snb.2007.05.050.

[112] A. I. Peptan, A. Lopez, R. A. Kopher, e J. J. Mao, «Responses of intramembranous bone and sutures upon in vivo cyclic tensile and compressive

loading», *Bone*, vol. 42, fasc. 2, pp. 432–438, feb. 2008, doi: 10.1016/j.bone.2007.05.014.

[113] M. Rummler *et al.*, «Mechanical loading prevents bone destruction and exerts anti-tumor effects in the MOPC315.BM.Luc model of myeloma bone disease», *Acta Biomaterialia*, vol. 119, pp. 247–258, gen. 2021, doi: 10.1016/j.actbio.2020.10.041.

[114] S. H. Park *et al.*, «PCL/β-TCP Composite Scaffolds Exhibit Positive Osteogenic Differentiation with Mechanical Stimulation», *Tissue Eng Regen Med*, vol. 14, fasc. 4, pp. 349–358, ago. 2017, doi: 10.1007/s13770-017-0022-9.

[115] T. Ohashi, Y. Sugaya, N. Sakamoto, e M. Sato, «Hydrostatic pressure influences morphology and expression of VE-cadherin of vascular endothelial cells», *Journal of Biomechanics*, vol. 40, fasc. 11, pp. 2399–2405, 2007, doi: 10.1016/j.jbiomech.2006.11.023.

[116] Y. Sun, D. Luo, Y. Zhu, e K. Wang, «MicroRNA 4323 induces human bladder smooth muscle cell proliferation under cyclic hydrodynamic pressure by activation of erk1/2 signaling pathway», *Exp Biol Med (Maywood)*, vol. 242, fasc. 2, pp. 169–176, gen. 2017, doi: 10.1177/1535370216669837.

[117] Y. Sun *et al.*, «MiR 3180-5p promotes proliferation in human bladder smooth muscle cell by targeting PODN under hydrodynamic pressure», *Sci Rep*, vol. 6, fasc. 1, p. 33042, set. 2016, doi: 10.1038/srep33042.

[118] R. M. Sappington, T. Sidorova, D. J. Long, e D. J. Calkins, «TRPV1: Contribution to Retinal Ganglion Cell Apoptosis and Increased Intracellular Ca $^{2+}$ with Exposure to Hydrostatic Pressure», *Invest. Ophthalmol. Vis. Sci.*, vol. 50, fasc. 2, p. 717, feb. 2009, doi: 10.1167/iovs.08-2321.

[119] K. Karamesinis *et al.*, «Continuous hydrostatic pressure induces differentiation phenomena in chondrocytes mediated by changes in polycystins, SOX9, and RUNX2», *J Orofac Orthop*, vol. 78, fasc. 1, pp. 21–31, gen. 2017, doi: 10.1007/s00056-016-0061-1.

[120] T. H. Hui, Z. L. Zhou, J. Qian, Y. Lin, A. H. W. Ngan, e H. Gao, «Volumetric Deformation of Live Cells Induced by Pressure-Activated Cross-

Membrane Ion Transport», *Phys. Rev. Lett.*, vol. 113, fasc. 11, p. 118101, set. 2014, doi: 10.1103/PhysRevLett.113.118101.

[121] J. P. K. Armstrong *et al.*, «Engineering Anisotropic Muscle Tissue using Acoustic Cell Patterning», *Adv. Mater.*, vol. 30, fasc. 43, p. 1802649, ott. 2018, doi: 10.1002/adma.201802649.

[122] J. W. Lim *et al.*, «An Active and Soft Hydrogel Actuator to Stimulate Live Cell Clusters by Self-folding», *Polymers*, vol. 12, fasc. 3, p. 583, mar. 2020, doi: 10.3390/polym12030583.

[123] Y. Li *et al.*, «Magnetically actuated cell-laden microscale hydrogels for probing strain-induced cell responses in three dimensions», *NPG Asia Mater*, vol. 8, fasc. 1, pp. e238–e238, gen. 2016, doi: 10.1038/am.2015.148.

[124] H. Sun *et al.*, «Complementary Logic Circuits Based on High-Performance n-Type Organic Electrochemical Transistors», *Adv. Mater.*, vol. 30, fasc. 9, p. 1704916, mar. 2018, doi: 10.1002/adma.201704916.

[125] D. Khodagholy *et al.*, «High transconductance organic electrochemical transistors», *Nat Commun*, vol. 4, fasc. 1, p. 2133, lug. 2013, doi: 10.1038/ncomms3133.

[126] M. ElMahmoudy, S. Inal, A. Charrier, I. Uguz, G. G. Malliaras, e S. Sanaur, «Tailoring the Electrochemical and Mechanical Properties of PEDOT:PSS Films for Bioelectronics», *Macromol. Mater. Eng.*, vol. 302, fasc. 5, p. 1600497, mag. 2017, doi: 10.1002/mame.201600497.

[127] X. Strakosas, B. Wei, D. C. Martin, e R. M. Owens, «Biofunctionalization of polydioxythiophene derivatives for biomedical applications», *J. Mater. Chem. B*, vol. 4, fasc. 29, pp. 4952–4968, 2016, doi: 10.1039/C6TB00852F.

[128] S. E. Doris, A. Pierre, e R. A. Street, «Dynamic and Tunable Threshold Voltage in Organic Electrochemical Transistors», *Adv. Mater.*, vol. 30, fasc. 15, p. 1706757, apr. 2018, doi: 10.1002/adma.201706757.

[129] P. Gkoupidenis, N. Schaefer, B. Garlan, e G. G. Malliaras, «Neuromorphic Functions in PEDOT:PSS Organic Electrochemical Transistors»,

Adv. Mater., vol. 27, fasc. 44, pp. 7176–7180, nov. 2015, doi: 10.1002/adma.201503674.

[130] C. Qian *et al.*, «Artificial Synapses Based on in-Plane Gate Organic Electrochemical Transistors», *ACS Appl. Mater. Interfaces*, vol. 8, fasc. 39, pp. 26169–26175, ott. 2016, doi: 10.1021/acsami.6b08866.

[131] M. Kostić *et al.*, «Design and Development of OECT Logic Circuits for Electrical Stimulation Applications», *Applied Sciences*, vol. 12, fasc. 8, p. 3985, apr. 2022, doi: 10.3390/app12083985.

[132] «MOSFETs», in *Physics of Semiconductor Devices*, Hoboken, NJ, USA: John Wiley & Sons, Inc., 2006, pp. 293–373. doi: 10.1002/9780470068328.ch6.

[133] J. Rivnay, S. Inal, A. Salleo, R. M. Owens, M. Berggren, e G. G. Malliaras, «Organic electrochemical transistors», *Nat Rev Mater*, vol. 3, fasc. 2, p. 17086, gen. 2018, doi: 10.1038/natrevmats.2017.86.

[134] S. Inal, G. G. Malliaras, e J. Rivnay, «Benchmarking organic mixed conductors for transistors», *Nat Commun*, vol. 8, fasc. 1, p. 1767, nov. 2017, doi: 10.1038/s41467-017-01812-w.

[135] D. A. Bernards e G. G. Malliaras, «Steady-State and Transient Behavior of Organic Electrochemical Transistors», *Adv. Funct. Mater.*, vol. 17, fasc. 17, pp. 3538–3544, nov. 2007, doi: 10.1002/adfm.200601239.

[136] D. A. Koutsouras, P. Gkoupidenis, C. Stolz, V. Subramanian, G. G. Malliaras, e D. C. Martin, «Impedance Spectroscopy of Spin-Cast and Electrochemically Deposited PEDOT:PSS Films on Microfabricated Electrodes with Various Areas», *ChemElectroChem*, vol. 4, fasc. 9, pp. 2321–2327, set. 2017, doi: 10.1002/celc.201700297.

[137] J. Newman, «Resistance for Flow of Current to a Disk», *J. Electrochem. Soc.*, vol. 113, fasc. 5, p. 501, 1966, doi: 10.1149/1.2424003.

[138] A. K. Ahuja, M. R. Behrend, J. J. Whalen, M. S. Humayun, e J. D. Weiland, «The Dependence of Spectral Impedance on Disc Microelectrode Radius», *IEEE Trans. Biomed. Eng.*, vol. 55, fasc. 4, pp. 1457–1460, apr. 2008, doi: 10.1109/TBME.2007.912430.

[139] P. Barthó, H. Hirase, L. Monconduit, M. Zugaro, K. D. Harris, e G. Buzsáki, «Characterization of Neocortical Principal Cells and Interneurons by Network Interactions and Extracellular Features», *Journal of Neurophysiology*, vol. 92, fasc. 1, pp. 600–608, lug. 2004, doi: 10.1152/jn.01170.2003.

[140] K. Tybrandt, S. B. Kollipara, e M. Berggren, «Organic electrochemical transistors for signal amplification in fast scan cyclic voltammetry», *Sensors and Actuators B: Chemical*, vol. 195, pp. 651–656, mag. 2014, doi: 10.1016/j.snb.2014.01.097.

[141] G. Tarabella, C. Santato, S. Y. Yang, S. Iannotta, G. G. Malliaras, e F. Cicoira, «Effect of the gate electrode on the response of organic electrochemical transistors», *Appl. Phys. Lett.*, vol. 97, fasc. 12, p. 123304, set. 2010, doi: 10.1063/1.3491216.

[142] D. A. Bernards, D. J. Macaya, M. Nikolou, J. A. DeFranco, S. Takamatsu, e G. G. Malliaras, «Enzymatic sensing with organic electrochemical transistors», *J. Mater. Chem.*, vol. 18, fasc. 1, pp. 116–120, 2008, doi: 10.1039/B713122D.

[143] J. Lee, L. G. Kaake, J. H. Cho, X.-Y. Zhu, T. P. Lodge, e C. D. Frisbie, «Ion Gel-Gated Polymer Thin-Film Transistors: Operating Mechanism and Characterization of Gate Dielectric Capacitance, Switching Speed, and Stability», *J. Phys. Chem. C*, vol. 113, fasc. 20, pp. 8972–8981, mag. 2009, doi: 10.1021/jp901426e.

[144] A. Laiho, L. Herlogsson, R. Forchheimer, X. Crispin, e M. Berggren, «Controlling the dimensionality of charge transport in organic thin-film transistors», *Proc. Natl. Acad. Sci. U.S.A.*, vol. 108, fasc. 37, pp. 15069–15073, set. 2011, doi: 10.1073/pnas.1107063108.

[145] F. Zare Bidoky e C. D. Frisbie, «Parasitic Capacitance Effect on Dynamic Performance of Aerosol-Jet-Printed Sub 2 V Poly(3-hexylthiophene) Electrolyte-Gated Transistors», *ACS Appl. Mater. Interfaces*, vol. 8, fasc. 40, pp. 27012–27017, ott. 2016, doi: 10.1021/acsami.6b08396.

[146] M. Ramuz *et al.*, «Optimization of a Planar All-Polymer Transistor for Characterization of Barrier Tissue», *ChemPhysChem*, vol. 16, fasc. 6, pp. 1210–1216, apr. 2015, doi: 10.1002/cphc.201402878.

[147] D. Khodagholy *et al.*, «High speed and high density organic electrochemical transistor arrays», *Appl. Phys. Lett.*, vol. 99, fasc. 16, p. 163304, ott. 2011, doi: 10.1063/1.3652912.

[148] C. Yao, C. Xie, P. Lin, F. Yan, P. Huang, e I.-M. Hsing, «Organic Electrochemical Transistor Array for Recording Transepithelial Ion Transport of Human Airway Epithelial Cells», *Adv. Mater.*, vol. 25, fasc. 45, pp. 6575–6580, dic. 2013, doi: 10.1002/adma.201302615.

[149] J. T. Friedlein, M. J. Donahue, S. E. Shaheen, G. G. Malliaras, e R. R. McLeod, «Microsecond Response in Organic Electrochemical Transistors: Exceeding the Ionic Speed Limit», *Adv. Mater.*, vol. 28, fasc. 38, pp. 8398–8404, ott. 2016, doi: 10.1002/adma.201602684.

[150] G. C. Faria, D. T. Duong, e A. Salleo, «On the transient response of organic electrochemical transistors», *Organic Electronics*, vol. 45, pp. 215–221, giu. 2017, doi: 10.1016/j.orgel.2017.03.021.

[151] D. E. Ward e R. W. Dutton, «A charge-oriented model for MOS transistor capacitances», *IEEE J. Solid-State Circuits*, vol. 13, fasc. 5, pp. 703–708, ott. 1978, doi: 10.1109/JSSC.1978.1051123.

[152] F. Liu, W. Xie, S. Shi, C. Daniel Frisbie, e P. Paul Ruden, «Coupling of channel conductance and gate-to-channel capacitance in electric double layer transistors», *Appl. Phys. Lett.*, vol. 103, fasc. 19, p. 193304, nov. 2013, doi: 10.1063/1.4829139.

[153] M. Z. Szymanski, D. Tu, e R. Forchheimer, «2-D Drift-Diffusion Simulation of Organic Electrochemical Transistors», *IEEE Trans. Electron Devices*, vol. 64, fasc. 12, pp. 5114–5120, dic. 2017, doi: 10.1109/TED.2017.2757766.

[154] J. J. Paulos e D. A. An, «Limitations of quasi-static capacitance models for the MOS transistor», *IEEE Electron Device Lett.*, vol. 4, fasc. 7, pp. 221–224, lug. 1983, doi: 10.1109/EDL.1983.25712.

[155] A. Giovannitti *et al.*, «Controlling the mode of operation of organic transistors through side-chain engineering», *Proc. Natl. Acad. Sci. U.S.A.*, vol. 113, fasc. 43, pp. 12017–12022, ott. 2016, doi: 10.1073/pnas.1608780113.

[156] C. Gold, D. A. Henze, C. Koch, e G. Buzsáki, «On the Origin of the Extracellular Action Potential Waveform: A Modeling Study», *Journal of Neurophysiology*, vol. 95, fasc. 5, pp. 3113–3128, mag. 2006, doi: 10.1152/jn.00979.2005.

[157] V. Kaphle, S. Liu, A. Al-Shadeedi, C.-M. Keum, e B. Lüssem, «Contact Resistance Effects in Highly Doped Organic Electrochemical Transistors», *Adv. Mater.*, vol. 28, fasc. 39, pp. 8766–8770, ott. 2016, doi: 10.1002/adma.201602125.

[158] R. L. Stoop, K. Thodkar, M. Sessolo, H. J. Bolink, C. Schönenberger, e M. Calame, «Charge Noise in Organic Electrochemical Transistors», *Phys. Rev. Applied*, vol. 7, fasc. 1, p. 014009, gen. 2017, doi: 10.1103/PhysRevApplied.7.014009.

[159] R. A. Street e A. Salleo, «Contact effects in polymer transistors», *Appl. Phys. Lett.*, vol. 81, fasc. 15, pp. 2887–2889, ott. 2002, doi: 10.1063/1.1512950.

[160] T. Miyadera, T. Minari, K. Tsukagoshi, H. Ito, e Y. Aoyagi, «Frequency response analysis of pentacene thin-film transistors with low impedance contact by interface molecular doping», *Appl. Phys. Lett.*, vol. 91, fasc. 1, p. 013512, lug. 2007, doi: 10.1063/1.2754350.

[161] M. Mottaghi e G. Horowitz, «Field-induced mobility degradation in pentacene thin-film transistors», *Organic Electronics*, vol. 7, fasc. 6, pp. 528–536, dic. 2006, doi: 10.1016/j.orgel.2006.07.011.

[162] O. Simonetti, L. Giraudet, T. Maurel, J.-L. Nicolas, e A. Belkhir, «Organic transistor model with nonlinear injection: Effects of uneven source contact on apparent mobility and threshold voltage», *Organic Electronics*, vol. 11, fasc. 8, pp. 1381–1393, ago. 2010, doi: 10.1016/j.orgel.2010.06.001.

[163] M. J. Donahue *et al.*, «High-Performance Vertical Organic Electrochemical Transistors», *Adv. Mater.*, vol. 30, fasc. 5, p. 1705031, feb. 2018, doi: 10.1002/adma.201705031.

[164] J. Rivnay *et al.*, «Organic Electrochemical Transistors with Maximum Transconductance at Zero Gate Bias», *Adv. Mater.*, vol. 25, fasc. 48, pp. 7010–7014, dic. 2013, doi: 10.1002/adma.201303080.

[165] Chun-Ying Chen e J. Kanicki, «Gated-four-probe a-Si:H TFT structure: a new technique to measure the intrinsic performance of a-Si:H TFT», *IEEE Electron Device Lett.*, vol. 18, fasc. 7, pp. 340–342, lug. 1997, doi: 10.1109/55.596930.

[166] A. A. Günther, M. Sawatzki, P. Formánek, D. Kasemann, e K. Leo, «Contact Doping for Vertical Organic Field-Effect Transistors», *Adv. Funct. Mater.*, vol. 26, fasc. 5, pp. 768–775, feb. 2016, doi: 10.1002/adfm.201504377.

[167] S. Singh *et al.*, «Reduction of contact resistance by selective contact doping in fullerene n-channel organic field-effect transistors», *Appl. Phys. Lett.*, vol. 102, fasc. 15, p. 153303, apr. 2013, doi: 10.1063/1.4802237.

[168] C. Liu, Y. Xu, e Y.-Y. Noh, «Contact engineering in organic field-effect transistors», *Materials Today*, vol. 18, fasc. 2, pp. 79–96, mar. 2015, doi: 10.1016/j.mattod.2014.08.037.

[169] C. M. Proctor, J. Rivnay, e G. G. Malliaras, «Understanding volumetric capacitance in conducting polymers», *J. Polym. Sci. Part B: Polym. Phys.*, vol. 54, fasc. 15, pp. 1433–1436, ago. 2016, doi: 10.1002/polb.24038.

[170] J. Li *et al.*, «Improving organic transistor performance through contact-area-limited doping», *Solid State Communications*, vol. 149, fasc. 41–42, pp. 1826–1830, nov. 2009, doi: 10.1016/j.ssc.2009.07.006.

[171] S. Schaur, P. Stadler, B. Meana-Esteban, H. Neugebauer, e N. Serdar Sariciftci, «Electrochemical doping for lowering contact barriers in organic field effect transistors», *Organic Electronics*, vol. 13, fasc. 8, pp. 1296–1301, ago. 2012, doi: 10.1016/j.orgel.2012.03.020.

[172] Y. Xu, R. Gwoziecki, I. Chartier, R. Coppard, F. Balestra, e G. Ghibaudo, «Modified transmission-line method for contact resistance extraction in organic field-effect transistors», *Appl. Phys. Lett.*, vol. 97, fasc. 6, p. 063302, ago. 2010, doi: 10.1063/1.3479476.

[173] T. J. Richards e H. Sirringhaus, «Analysis of the contact resistance in staggered, top-gate organic field-effect transistors», *Journal of Applied Physics*, vol. 102, fasc. 9, p. 094510, nov. 2007, doi: 10.1063/1.2804288.

[174] E. G. Bittle, J. I. Basham, T. N. Jackson, O. D. Jurchescu, e D. J. Gundlach, «Mobility overestimation due to gated contacts in organic field-effect transistors», *Nat Commun*, vol. 7, fasc. 1, p. 10908, mar. 2016, doi: 10.1038/ncomms10908.

[175] O. Vatel e M. Tanimoto, «Kelvin probe force microscopy for potential distribution measurement of semiconductor devices», *Journal of Applied Physics*, vol. 77, fasc. 6, pp. 2358–2362, mar. 1995, doi: 10.1063/1.358758.

[176] F. V. Di Girolamo, M. Barra, V. Capello, M. Oronzio, C. Romano, e A. Cassinese, «Bias stress instability in organic transistors investigated by ac admittance measurements», *Journal of Applied Physics*, vol. 107, fasc. 11, p. 114508, giu. 2010, doi: 10.1063/1.3425795.

[177] J. Rivnay *et al.*, «High-performance transistors for bioelectronics through tuning of channel thickness», *Sci. Adv.*, vol. 1, fasc. 4, p. e1400251, mag. 2015, doi: 10.1126/sciadv.1400251.

[178] F. Bonafè, F. Decataldo, B. Fraboni, e T. Cramer, «Charge Carrier Mobility in Organic Mixed Ionic–Electronic Conductors by the Electrolyte-Gated van der Pauw Method», *Adv. Electron. Mater.*, vol. 7, fasc. 10, p. 2100086, ott. 2021, doi: 10.1002/aelm.202100086.

[179] M. Braendlein, T. Lonjaret, P. Leleux, J.-M. Badier, e G. G. Malliaras, «Voltage Amplifier Based on Organic Electrochemical Transistor», *Adv. Sci.*, vol. 4, fasc. 1, p. 1600247, gen. 2017, doi: 10.1002/advs.201600247.

[180] S. D. Baranovskii, «Theoretical description of charge transport in disordered organic semiconductors: Charge transport in disordered organic semiconductors», *Phys. Status Solidi B*, vol. 251, fasc. 3, pp. 487–525, mar. 2014, doi: 10.1002/pssb.201350339.

[181] N. Tessler, Y. Preezant, N. Rappaport, e Y. Roichman, «Charge Transport in Disordered Organic Materials and Its Relevance to Thin-Film Devices: A Tutorial Review», *Adv. Mater.*, vol. 21, fasc. 27, pp. 2741–2761, lug. 2009, doi: 10.1002/adma.200803541.

[182] S.-J. Yoo e J.-J. Kim, «Charge Transport in Electrically Doped Amorphous Organic Semiconductors», *Macromol. Rapid Commun.*, vol. 36, fasc. 11, pp. 984–1000, giu. 2015, doi: 10.1002/marc.201500026.

[183] V. Coropceanu, J. Cornil, D. A. Da Silva Filho, Y. Olivier, R. Silbey, e J.-L. Brédas, «Charge Transport in Organic Semiconductors», *Chem. Rev.*, vol. 107, fasc. 4, pp. 926–952, apr. 2007, doi: 10.1021/cr050140x.

[184] R. Noriega *et al.*, «A general relationship between disorder, aggregation and charge transport in conjugated polymers», *Nature Mater*, vol. 12, fasc. 11, pp. 1038–1044, nov. 2013, doi: 10.1038/nmat3722.

[185] M. C. J. M. Vissenberg e M. Matters, «Theory of the field-effect mobility in amorphous organic transistors», *Phys. Rev. B*, vol. 57, fasc. 20, pp. 12964–12967, mag. 1998, doi: 10.1103/PhysRevB.57.12964.

[186] V. Ambegaokar, B. I. Halperin, e J. S. Langer, «Hopping Conductivity in Disordered Systems», *Phys. Rev. B*, vol. 4, fasc. 8, pp. 2612–2620, ott. 1971, doi: 10.1103/PhysRevB.4.2612.

[187] A. B. Kaiser e V. Skákalová, «Electronic conduction in polymers, carbon nanotubes and graphene», *Chem. Soc. Rev.*, vol. 40, fasc. 7, p. 3786, 2011, doi: 10.1039/c0cs00103a.

[188] R. H. Young e J. J. Fitzgerald, «Effect of polar additives on charge transport in a molecularly doped polymer: Evaluation of disorder models», *The Journal of Chemical Physics*, vol. 102, fasc. 23, pp. 9380–9391, giu. 1995, doi: 10.1063/1.468806.

[189] J. M. Frost, J. Kirkpatrick, T. Kirchartz, e J. Nelson, «Parameter free calculation of the subgap density of states in poly(3-hexylthiophene)», *Faraday Discuss.*, vol. 174, pp. 255–266, 2014, doi: 10.1039/C4FD00153B.

[190] Z. G. Yu, D. L. Smith, A. Saxena, R. L. Martin, e A. R. Bishop, «Molecular Geometry Fluctuation Model for the Mobility of Conjugated Polymers», *Phys. Rev. Lett.*, vol. 84, fasc. 4, pp. 721–724, gen. 2000, doi: 10.1103/PhysRevLett.84.721.

[191] V. I. Arkhipov, P. Heremans, E. V. Emelianova, e H. Bässler, «Effect of doping on the density-of-states distribution and carrier hopping in disordered organic semiconductors», *Phys. Rev. B*, vol. 71, fasc. 4, p. 045214, gen. 2005, doi: 10.1103/PhysRevB.71.045214.

[192] X.-H. Shi, J.-X. Sun, C.-H. Xiong, e L. Sun, «Exponential-type density of states with clearly cutting tail for organic semiconductors», *Organic Electronics*, vol. 30, pp. 60–66, mar. 2016, doi: 10.1016/j.orgel.2015.11.023.

[193] Q. Wei, M. Mukaida, K. Kirihara, Y. Naitoh, e T. Ishida, «Photoinduced Dedoping of Conducting Polymers: An Approach to Precise Control of the Carrier Concentration and Understanding Transport Properties», *ACS Appl. Mater. Interfaces*, vol. 8, fasc. 3, pp. 2054–2060, gen. 2016, doi: 10.1021/acsami.5b10453.

[194] Y. Xia, J. H. Cho, J. Lee, P. P. Ruden, e C. D. Frisbie, «Comparison of the Mobility-Carrier Density Relation in Polymer and Single-Crystal Organic Transistors Employing Vacuum and Liquid Gate Dielectrics», *Adv. Mater.*, vol. 21, fasc. 21, pp. 2174–2179, giu. 2009, doi: 10.1002/adma.200803437.

[195] J. T. Friedlein, S. E. Shaheen, G. G. Malliaras, e R. R. McLeod, «Optical Measurements Revealing Nonuniform Hole Mobility in Organic Electrochemical Transistors», *Adv. Electron. Mater.*, vol. 1, fasc. 11, p. 1500189, nov. 2015, doi: 10.1002/aelm.201500189.

[196] C. Yao, Q. Li, J. Guo, F. Yan, e I.-M. Hsing, «Rigid and Flexible Organic Electrochemical Transistor Arrays for Monitoring Action Potentials from Electrogenic Cells», *Adv. Healthcare Mater.*, vol. 4, fasc. 4, pp. 528–533, mar. 2015, doi: 10.1002/adhm.201400406.

[197] C. H. McCoy e M. S. Wrighton, «Potential-dependent conductivity of conducting polymers yields opportunities for molecule-based devices: a microelectrochemical push-pull amplifier based on two different conducting polymer transistors», *Chem. Mater.*, vol. 5, fasc. 7, pp. 914–916, lug. 1993, doi: 10.1021/cm00031a006.

[198] B. D. Paulsen e C. D. Frisbie, «Dependence of Conductivity on Charge Density and Electrochemical Potential in Polymer Semiconductors Gated with Ionic Liquids», *J. Phys. Chem. C*, vol. 116, fasc. 4, pp. 3132–3141, feb. 2012, doi: 10.1021/jp2093934.

[199] D. Ofer, L. Y. Park, R. R. Schrock, e M. S. Wrighton, «Potential dependence of the conductivity of polyacetylene: finite potential windows of high

conductivity», *Chem. Mater.*, vol. 3, fasc. 4, pp. 573–575, lug. 1991, doi: 10.1021/cm00016a004.

[200] H. S. White, G. P. Kittlesen, e M. S. Wrighton, «Chemical derivatization of an array of three gold microelectrodes with polypyrrole: fabrication of a molecule-based transistor», *J. Am. Chem. Soc.*, vol. 106, fasc. 18, pp. 5375–5377, set. 1984, doi: 10.1021/ja00330a070.

[201] M. Demelas, E. Scavetta, L. Basiricò, R. Rogani, e A. Bonfiglio, «A deeper insight into the operation regime of all-polymeric electrochemical transistors», *Appl. Phys. Lett.*, vol. 102, fasc. 19, p. 193301, mag. 2013, doi: 10.1063/1.4804423.

[202] T. Blaudeck *et al.*, «Simplified Large-Area Manufacturing of Organic Electrochemical Transistors Combining Printing and a Self-Aligning Laser Ablation Step», *Adv. Funct. Mater.*, vol. 22, fasc. 14, pp. 2939–2948, lug. 2012, doi: 10.1002/adfm.201102827.

[203] T. Lan, F. Soavi, M. Marcaccio, P.-L. Brunner, J. Sayago, e C. Santato, «Electrolyte-gated transistors based on phenyl-C_{61}-butyric acid methyl ester (PCBM) films: bridging redox properties, charge carrier transport and device performance», *Chem. Commun.*, vol. 54, fasc. 43, pp. 5490–5493, 2018, doi: 10.1039/C8CC03090A.

[204] Y. Shen, K. Diest, M. H. Wong, B. R. Hsieh, D. H. Dunlap, e G. G. Malliaras, «Charge transport in doped organic semiconductors», *Phys. Rev. B*, vol. 68, fasc. 8, p. 081204, ago. 2003, doi: 10.1103/PhysRevB.68.081204.

[205] M. Ramuz, A. Hama, J. Rivnay, P. Leleux, e R. M. Owens, «Monitoring of cell layer coverage and differentiation with the organic electrochemical transistor», *J. Mater. Chem. B*, vol. 3, fasc. 29, pp. 5971–5977, 2015, doi: 10.1039/C5TB00922G.

[206] I. N. Hulea, H. B. Brom, A. J. Houtepen, D. Vanmaekelbergh, J. J. Kelly, e E. A. Meulenkamp, «Wide Energy-Window View on the Density of States and Hole Mobility in Poly(p -Phenylene Vinylene)», *Phys. Rev. Lett.*, vol. 93, fasc. 16, p. 166601, ott. 2004, doi: 10.1103/PhysRevLett.93.166601.

[207] D. Vanmaekelbergh, A. J. Houtepen, e J. J. Kelly, «Electrochemical gating: A method to tune and monitor the (opto)electronic

properties of functional materials», *Electrochimica Acta*, vol. 53, fasc. 3, pp. 1140–1149, dic. 2007, doi: 10.1016/j.electacta.2007.02.045.

[208] X. Wang, B. Shapiro, e E. Smela, «Development of a Model for Charge Transport in Conjugated Polymers», *J. Phys. Chem. C*, vol. 113, fasc. 1, pp. 382–401, gen. 2009, doi: 10.1021/jp802941m.

[209] S. Wang, M. Ha, M. Manno, C. Daniel Frisbie, e C. Leighton, «Hopping transport and the Hall effect near the insulator–metal transition in electrochemically gated poly(3-hexylthiophene) transistors», *Nat Commun*, vol. 3, fasc. 1, p. 1210, nov. 2012, doi: 10.1038/ncomms2213.

[210] W. Xie, F. Liu, S. Shi, P. P. Ruden, e C. D. Frisbie, «Charge Density Dependent Two-Channel Conduction in Organic Electric Double Layer Transistors (EDLTs)», *Adv. Mater.*, vol. 26, fasc. 16, pp. 2527–2532, apr. 2014, doi: 10.1002/adma.201304946.

[211] X. Wang e E. Smela, «Color and Volume Change in PPy(DBS)», *J. Phys. Chem. C*, vol. 113, fasc. 1, pp. 359–368, gen. 2009, doi: 10.1021/jp802937v.

[212] R. A. Marcus, «Electron transfer reactions in chemistry theory and experiment», *Journal of Electroanalytical Chemistry*, vol. 438, fasc. 1–2, pp. 251–259, nov. 1997, doi: 10.1016/S0022-0728(97)00091-0.

[213] M. J. Bissell e W. C. Hines, «Why don't we get more cancer? A proposed role of the microenvironment in restraining cancer progression», *Nat Med*, vol. 17, fasc. 3, pp. 320–329, mar. 2011, doi: 10.1038/nm.2328.

[214] W. J. Polacheck, R. Li, S. G. M. Uzel, e R. D. Kamm, «Microfluidic platforms for mechanobiology», *Lab Chip*, vol. 13, fasc. 12, p. 2252, 2013, doi: 10.1039/c3lc41393d.

[215] K. Wang, L.-H. Cai, B. Lan, e J. J. Fredberg, «Hidden in the mist no more: physical force in cell biology», *Nat Methods*, vol. 13, fasc. 2, pp. 124–125, feb. 2016, doi: 10.1038/nmeth.3744.

[216] K. R. Levental *et al.*, «Matrix Crosslinking Forces Tumor Progression by Enhancing Integrin Signaling», *Cell*, vol. 139, fasc. 5, pp. 891–906, nov. 2009, doi: 10.1016/j.cell.2009.10.027.

[217] S. Takao, M. Taya, e C. Chiew, «Mechanical stress-induced cell death in breast cancer cells», *Biology Open*, p. bio.043133, gen. 2019, doi: 10.1242/bio.043133.

[218] S. Hosmane *et al.*, «Valve-based microfluidic compression platform: single axon injury and regrowth», *Lab Chip*, vol. 11, fasc. 22, p. 3888, 2011, doi: 10.1039/c1lc20549h.

[219] J. M. Tse *et al.*, «Mechanical compression drives cancer cells toward invasive phenotype», *Proc. Natl. Acad. Sci. U.S.A.*, vol. 109, fasc. 3, pp. 911–916, gen. 2012, doi: 10.1073/pnas.1118910109.

[220] M. Kalli, P. Papageorgis, V. Gkretsi, e T. Stylianopoulos, «Solid Stress Facilitates Fibroblasts Activation to Promote Pancreatic Cancer Cell Migration», *Ann Biomed Eng*, vol. 46, fasc. 5, pp. 657–669, mag. 2018, doi: 10.1007/s10439-018-1997-7.

[221] C. Nicolò *et al.*, «A programmable culture platform for hydrostatic stimulation and in situ pH sensing of lung cancer cells with organic electrochemical transistors», *Micro and Nano Engineering*, vol. 16, p. 100147, ago. 2022, doi: 10.1016/j.mne.2022.100147.

[222] B. Lan *et al.*, «Airway epithelial compression promotes airway smooth muscle proliferation and contraction», *American Journal of Physiology-Lung Cellular and Molecular Physiology*, vol. 315, fasc. 5, pp. L645–L652, nov. 2018, doi: 10.1152/ajplung.00261.2018.

[223] N. Marozkina *et al.*, «Cyclic compression increases F508 Del CFTR expression in ciliated human airway epithelium», *American Journal of Physiology-Lung Cellular and Molecular Physiology*, vol. 317, fasc. 2, pp. L247–L258, ago. 2019, doi: 10.1152/ajplung.00020.2019.

[224] A. Kılıç *et al.*, «Mechanical forces induce an asthma gene signature in healthy airway epithelial cells», *Sci Rep*, vol. 10, fasc. 1, p. 966, dic. 2020, doi: 10.1038/s41598-020-57755-8.

[225] M. Luo, K. K. Y. Ho, Z. Tong, L. Deng, e A. P. Liu, «Compressive Stress Enhances Invasive Phenotype of Cancer Cells via Piezo1 Activation», Cell Biology, preprint, gen. 2019. doi: 10.1101/513218.

[226] C. M. Novak, E. N. Horst, E. Lin, e G. Mehta, «Compressive Stimulation Enhances Ovarian Cancer Proliferation, Invasion, Chemoresistance, and Mechanotransduction via CDC42 in a 3D Bioreactor», *Cancers*, vol. 12, fasc. 6, p. 1521, giu. 2020, doi: 10.3390/cancers12061521.

[227] M. Asem *et al.*, «Ascites-induced compression alters the peritoneal microenvironment and promotes metastatic success in ovarian cancer», *Sci Rep*, vol. 10, fasc. 1, p. 11913, dic. 2020, doi: 10.1038/s41598-020-68639-2.

[228] M. Carlos-Oliveira, F. Lozano-Juan, P. Occhetta, R. Visone, e M. Rasponi, «Current strategies of mechanical stimulation for maturation of cardiac microtissues», *Biophys Rev*, vol. 13, fasc. 5, pp. 717–727, ott. 2021, doi: 10.1007/s12551-021-00841-6.

[229] C. Lui *et al.*, «Mechanical stimulation enhances development of scaffold-free, 3D-printed, engineered heart tissue grafts», *J Tissue Eng Regen Med*, vol. 15, fasc. 5, pp. 503–512, mag. 2021, doi: 10.1002/term.3188.

[230] D. Lee, A. Erickson, T. You, A. T. Dudley, e S. Ryu, «Pneumatic microfluidic cell compression device for high-throughput study of chondrocyte mechanobiology», *Lab Chip*, vol. 18, fasc. 14, pp. 2077–2086, 2018, doi: 10.1039/C8LC00320C.

[231] H.-Y. Hsieh *et al.*, «Gradient static-strain stimulation in a microfluidic chip for 3D cellular alignment», *Lab Chip*, vol. 14, fasc. 3, pp. 482–493, 2014, doi: 10.1039/C3LC50884F.

[232] Y. Klymenko *et al.*, «Modeling the effect of ascites-induced compression on ovarian cancer multicellular aggregates», *Disease Models & Mechanisms*, vol. 11, fasc. 9, p. dmm034199, set. 2018, doi: 10.1242/dmm.034199.

[233] Bregenzer, Horst, Mehta, Novak, Repetto, e Mehta, «The Role of Cancer Stem Cells and Mechanical Forces in Ovarian Cancer Metastasis», *Cancers*, vol. 11, fasc. 7, p. 1008, lug. 2019, doi: 10.3390/cancers11071008.

[234] R. K. Jain, J. D. Martin, e T. Stylianopoulos, «The Role of Mechanical Forces in Tumor Growth and Therapy», *Annu. Rev. Biomed. Eng.*, vol. 16, fasc. 1, pp. 321–346, lug. 2014, doi: 10.1146/annurev-bioeng-071813-105259.

[235] K. S. Hintz, H. Vedel, e E. Kaas, «Collecting and processing of barometric data from smartphones for potential use in numerical weather prediction data assimilation», *Meteorol Appl*, vol. 26, fasc. 4, pp. 733–746, ott. 2019, doi: 10.1002/met.1805.

[236] «Cancer». https://www.who.int/news-room/fact-sheets/detail/cancer (consultato 19 novembre 2021).

[237] J. Shrestha *et al.*, «Lung-on-a-chip: the future of respiratory disease models and pharmacological studies», *Critical Reviews in Biotechnology*, vol. 40, fasc. 2, pp. 213–230, feb. 2020, doi: 10.1080/07388551.2019.1710458.

[238] B. A. Hassell *et al.*, «Human Organ Chip Models Recapitulate Orthotopic Lung Cancer Growth, Therapeutic Responses, and Tumor Dormancy In Vitro», *Cell Reports*, vol. 21, fasc. 2, pp. 508–516, ott. 2017, doi: 10.1016/j.celrep.2017.09.043.

[239] J. Wang, C. Wang, N. Xu, Z.-F. Liu, D.-W. Pang, e Z.-L. Zhang, «A virus-induced kidney disease model based on organ-on-a-chip: Pathogenesis exploration of virus-related renal dysfunctions», *Biomaterials*, vol. 219, p. 119367, ott. 2019, doi: 10.1016/j.biomaterials.2019.119367.

[240] N. S. Bhise *et al.*, «A liver-on-a-chip platform with bioprinted hepatic spheroids», *Biofabrication*, vol. 8, fasc. 1, p. 014101, gen. 2016, doi: 10.1088/1758-5090/8/1/014101.

[241] J. Park, B. K. Lee, G. S. Jeong, J. K. Hyun, C. J. Lee, e S.-H. Lee, «Three-dimensional brain-on-a-chip with an interstitial level of flow and its application as an in vitro model of Alzheimer's disease», *Lab Chip*, vol. 15, fasc. 1, pp. 141–150, 2015, doi: 10.1039/C4LC00962B.

[242] T. Najrana *et al.*, «Mechanical stretch regulates the expression of specific miRNA in extracellular vesicles released from lung epithelial cells», *J Cell Physiol*, vol. 235, fasc. 11, pp. 8210–8223, nov. 2020, doi: 10.1002/jcp.29476.

[243] A. Romeo *et al.*, «Drug-induced cellular death dynamics monitored by a highly sensitive organic electrochemical system», *Biosensors and Bioelectronics*, vol. 68, pp. 791–797, giu. 2015, doi: 10.1016/j.bios.2015.01.073.

[244] J. J. Davenport, M. Hickey, J. P. Phillips, e P. A. Kyriacou, «Dual pO $_2$ /pCO $_2$ fibre optic sensing film», *Analyst*, vol. 142, fasc. 10, pp. 1711–1719, 2017, doi: 10.1039/C7AN00173H.

[245] L. Ding, C. Fan, Y. Zhong, T. Li, e J. Huang, «A sensitive optic fiber sensor based on CdSe QDs fluorophore for nitric oxide detection», *Sensors and Actuators B: Chemical*, vol. 185, pp. 70–76, ago. 2013, doi: 10.1016/j.snb.2013.04.092.

[246] A. Deep *et al.*, «Immobilization of enzyme on long period grating fibers for sensitive glucose detection», *Biosensors and Bioelectronics*, vol. 33, fasc. 1, pp. 190–195, mar. 2012, doi: 10.1016/j.bios.2011.12.051.

[247] D. Choudhury *et al.*, «Endoscopic sensing of alveolar pH», *Biomed. Opt. Express*, vol. 8, fasc. 1, p. 243, gen. 2017, doi: 10.1364/BOE.8.000243.

[248] C. Justus, E. Sanderlin, e L. Yang, «Molecular Connections between Cancer Cell Metabolism and the Tumor Microenvironment», *IJMS*, vol. 16, fasc. 12, pp. 11055–11086, mag. 2015, doi: 10.3390/ijms160511055.

[249] S. Romero-Garcia, H. Prado-Garcia, A. D. Valencia-Camargo, e A. Alvarez-Pulido, «Lactic Acidosis Promotes Mitochondrial Biogenesis in Lung Adenocarcinoma Cells, Supporting Proliferation Under Normoxia or Survival Under Hypoxia», *Front. Oncol.*, vol. 9, p. 1053, ott. 2019, doi: 10.3389/fonc.2019.01053.

[250] P. Vaupel, H. Schmidberger, e A. Mayer, «The Warburg effect: essential part of metabolic reprogramming and central contributor to cancer progression», *International Journal of Radiation Biology*, vol. 95, fasc. 7, pp. 912–919, lug. 2019, doi: 10.1080/09553002.2019.1589653.

[251] L. V., R. D., e L. Dong, «Targeting Tumor Microenvironments for Cancer Prevention and Therapy», in *Cancer Prevention - From Mechanisms to Translational Benefits*, A. G. Georgakilas, A c. di, InTech, 2012. doi: 10.5772/28692.

[252] W. Liu *et al.*, «The Suppression of Medium Acidosis Improves the Maintenance and Differentiation of Human Pluripotent Stem Cells at High

Density in Defined Cell Culture Medium», *Int. J. Biol. Sci.*, vol. 14, fasc. 5, pp. 485–496, 2018, doi: 10.7150/ijbs.24681.

[253] Y. Wu, B. Gao, Q.-J. Xiong, Y.-C. Wang, D.-K. Huang, e W.-N. Wu, «Acid-sensing ion channels contribute to the effect of extracellular acidosis on proliferation and migration of A549 cells», *Tumour Biol.*, vol. 39, fasc. 6, p. 101042831770575, giu. 2017, doi: 10.1177/1010428317705750.

[254] H. Chugh, D. Sood, I. Chandra, V. Tomar, G. Dhawan, e R. Chandra, «Role of gold and silver nanoparticles in cancer nano-medicine», *Artificial Cells, Nanomedicine, and Biotechnology*, vol. 46, fasc. sup1, pp. 1210–1220, ott. 2018, doi: 10.1080/21691401.2018.1449118.

[255] X. Han, K. Xu, O. Taratula, e K. Farsad, «Applications of nanoparticles in biomedical imaging», *Nanoscale*, vol. 11, fasc. 3, pp. 799–819, 2019, doi: 10.1039/C8NR07769J.

[256] F.-Y. Kong, J.-W. Zhang, R.-F. Li, Z.-X. Wang, W.-J. Wang, e W. Wang, «Unique Roles of Gold Nanoparticles in Drug Delivery, Targeting and Imaging Applications», *Molecules*, vol. 22, fasc. 9, p. 1445, ago. 2017, doi: 10.3390/molecules22091445.

[257] S. Jain, D. G. Hirst, e J. M. O'Sullivan, «Gold nanoparticles as novel agents for cancer therapy», *BJR*, vol. 85, fasc. 1010, pp. 101–113, feb. 2012, doi: 10.1259/bjr/59448833.

[258] I. Hammami, N. M. Alabdallah, A. A. Jomaa, e M. Kamoun, «Gold nanoparticles: Synthesis properties and applications», *Journal of King Saud University - Science*, vol. 33, fasc. 7, p. 101560, ott. 2021, doi: 10.1016/j.jksus.2021.101560.

[259] B. Fadeel e A. E. Garcia-Bennett, «Better safe than sorry: Understanding the toxicological properties of inorganic nanoparticles manufactured for biomedical applications», *Advanced Drug Delivery Reviews*, vol. 62, fasc. 3, pp. 362–374, mar. 2010, doi: 10.1016/j.addr.2009.11.008.

[260] P. Suchomel *et al.*, «Simple size-controlled synthesis of Au nanoparticles and their size-dependent catalytic activity», *Sci Rep*, vol. 8, fasc. 1, p. 4589, mar. 2018, doi: 10.1038/s41598-018-22976-5.

[261] M. Tran, R. DePenning, M. Turner, e S. Padalkar, «Effect of citrate ratio and temperature on gold nanoparticle size and morphology», *Mater. Res. Express*, vol. 3, fasc. 10, p. 105027, ott. 2016, doi: 10.1088/2053-1591/3/10/105027.

[262] B. Contreras-Trigo *et al.*, «Slight pH Fluctuations in the Gold Nanoparticle Synthesis Process Influence the Performance of the Citrate Reduction Method», *Sensors*, vol. 18, fasc. 7, p. 2246, lug. 2018, doi: 10.3390/s18072246.

[263] J. Kimling, M. Maier, B. Okenve, V. Kotaidis, H. Ballot, e A. Plech, «Turkevich Method for Gold Nanoparticle Synthesis Revisited», *J. Phys. Chem. B*, vol. 110, fasc. 32, pp. 15700–15707, ago. 2006, doi: 10.1021/jp061667w.

[264] W. Patungwasa e J. H. Hodak, «pH tunable morphology of the gold nanoparticles produced by citrate reduction», *Materials Chemistry and Physics*, vol. 108, fasc. 1, pp. 45–54, mar. 2008, doi: 10.1016/j.matchemphys.2007.09.001.

[265] I. L. Moldero *et al.*, «Probing the pH Microenvironment of Mesenchymal Stromal Cell Cultures on Additive-Manufactured Scaffolds», *Small*, vol. 16, fasc. 34, p. 2002258, ago. 2020, doi: 10.1002/smll.202002258.

[266] J. Ge *et al.*, «A two-photon ratiometric fluorescent probe for effective monitoring of lysosomal pH in live cells and cancer tissues», *Sensors and Actuators B: Chemical*, vol. 262, pp. 913–921, giu. 2018, doi: 10.1016/j.snb.2018.02.082.

[267] G. Scheiblin, R. Coppard, R. M. Owens, P. Mailley, e G. G. Malliaras, «Referenceless pH Sensor using Organic Electrochemical Transistors», *Adv. Mater. Technol.*, vol. 2, fasc. 2, p. 1600141, feb. 2017, doi: 10.1002/admt.201600141.

[268] E. Macchia *et al.*, «Ultra-sensitive protein detection with organic electrochemical transistors printed on plastic substrates», *Flex. Print. Electron.*, vol. 3, fasc. 3, p. 034002, lug. 2018, doi: 10.1088/2058-8585/aad0cb.

[269] K. Lieberth *et al.*, «Current-Driven Organic Electrochemical Transistors for Monitoring Cell Layer Integrity with Enhanced Sensitivity», *Adv.*

Healthcare Mater., vol. 10, fasc. 19, p. 2100845, ott. 2021, doi: 10.1002/adhm.202100845.

[270] L. Chen *et al.*, «Organic Electrochemical Transistors for the Detection of Cell Surface Glycans», *ACS Appl. Mater. Interfaces*, vol. 10, fasc. 22, pp. 18470–18477, giu. 2018, doi: 10.1021/acsami.8b01987.

[271] D. Khodagholy *et al.*, «In vivo recordings of brain activity using organic transistors», *Nat Commun*, vol. 4, fasc. 1, p. 1575, giu. 2013, doi: 10.1038/ncomms2573.

[272] Y. Lee, G. Lee, M. Cho, e J.-K. Park, «Design criteria and standardization of a microfluidic cell culture system for investigating cellular migration», *J. Micromech. Microeng.*, vol. 29, fasc. 4, p. 043003, apr. 2019, doi: 10.1088/1361-6439/ab0796.

[273] C. Peng, J. P. Crawshaw, G. C. Maitland, J. P. Martin Trusler, e D. Vega-Maza, «The pH of CO2-saturated water at temperatures between 308K and 423K at pressures up to 15MPa», *The Journal of Supercritical Fluids*, vol. 82, pp. 129–137, ott. 2013, doi: 10.1016/j.supflu.2013.07.001.

[274] B. Meyssami, M. O. Balaban, e A. A. Teixeira, «Prediction of pH in model systems pressurized with carbon dioxide», *Biotechnol. Prog.*, vol. 8, fasc. 2, pp. 149–154, mar. 1992, doi: 10.1021/bp00014a009.

[275] M. Segantini *et al.*, «Design of a Portable Microfluidic Platform for EGOT-Based in Liquid Biosensing», *Sensors*, vol. 22, fasc. 3, p. 969, gen. 2022, doi: 10.3390/s22030969.

[276] D. Arcoraci *et al.*, «Enhancing the performance and mechanical stability of 2D-based hybrid micro-supercapacitors using dendritic-gold as framework layer», *Electrochimica Acta*, vol. 453, p. 142346, giu. 2023, doi: 10.1016/j.electacta.2023.142346.